

Experimental Studies of Surface Melting and Time-  
Resolved Superheating of Metal Surfaces

by

Elizabeth Ann Murphy

Submitted in Partial Fulfillment

of the

Requirements for the Degree

Doctor of Philosophy

Supervised by

Professor Yongli Gao

Department of Physics and Astronomy  
College of Arts and Science

University of Rochester  
Rochester, NY

1993

## Curriculum Vitae

Elizabeth Ann Murphy was born in Boston, Massachusetts on April 26, 1966. She attended Colby College from 1984 to 1988, and graduated summa cum laude with a Bachelor of Arts degree in Physics with Honors and a concentration in Applied Mathematics. She came to the University of Rochester in the Fall of 1988 and began graduate studies in Physics. She received a Rush Rhees Fellowship for her first three years of graduate study and the Department of Physics and Astronomy Graduate Student Teaching Award in the Spring of 1989. In her first year of graduate school she held a teaching assistantship and a research assistantship thereafter. Elizabeth Murphy's research fellowship was provided by the Laboratory for Laser Energetics at the University of Rochester from February 1990 through August 1993. She taught as a Dean's Teaching Fellow during the Spring semester of 1991. She pursued research in surface physics under the direction of Professor Hani Elsayed-Ali at the Laboratory for Laser Energetics, receiving the Master of Arts degree in 1990. Professor Yongli Gao, from the Department of Physics and Astronomy, served as her departmental advisor.

## Acknowledgements

I would like to thank Professors Hani Elsayed-Ali and Yongli Gao for their support and guidance throughout my graduate-student career. I would especially like to thank Professor Robert Knox and John Herman for their encouragement, support, and invaluable friendships. I greatly appreciate the opportunities that have been provided by the Department of Physics and Astronomy regarding my interest in college-level teaching. I would also like to thank my family and Peter for their patience, emotional support, and confidence.

All work was supported by the U.S. Department of Energy, Division of Materials Sciences, under contract No. DE-FG02-88ER45376. Additional support for the work discussed in Chapter 2 was provided by the National Science Foundation under contract No. DMR-8913880. I would like to thank the Laboratory for Laser Energetics for providing me with a research assistantship. I would also like to thank Dr. Scott Chambers for the code for the single-scattering cluster model, and Professor S. Y. Tong for the multiple-scattering calculations, both discussed in Chapter 2. In addition, I gratefully acknowledge Dr. J. Chu for the SEM images shown in Chapter 3.

## Abstract

The surface plays a very important role in the process of melting of a solid and therefore studies of the thermal behavior of surfaces can lead to a better understanding of the microscopic nature of bulk melting. In this thesis, experimental measurements of the disordering and superheating of surfaces of lead and of bismuth, respectively, are described. Surface disordering of Pb(100) is studied by monitoring the diffraction corresponding to the surface structure as a function of temperature using the x-ray photoelectron diffraction technique. The diffraction pattern gives quantitative information about the temperature-dependent degree of surface order or disorder. The Pb(100) surface is found to experience incomplete surface melting. Superheating of Bi(0001) is studied using time-resolved reflection high-energy electron diffraction, which provides surface structural information as a function of temperature as well as time. Superheating by about 90 K is observed.

## Table of Contents

Curriculum Vitae.....	ii
Acknowledgements.....	iii
Abstract.....	iv
Table of Contents.....	v
List of Tables.....	vii
List of Figures.....	viii
List of Abbreviations.....	xii
Chapter 1	
1.1	1
Introduction: The Role of the Surface in Melting of the Bulk.....	
1.2	10
References.....	
Chapter 2	
Temperature-Dependent X-ray Photoelectron Diffraction of Pb(100).....	11
2.1	11
Introduction.....	
2.2	13
X-ray Photoelectron Diffraction.....	
2.3	13
Experiment.....	
2.4	22
Temperature-Dependent X-ray Photoelectron Diffraction of Pb(100): Experimental Results and the Single-Scattering Cluster Model.....	
2.4.1	25
The Single-Scattering Cluster Model.....	
2.4.2	31
Results and Discussion.....	
2.5	39
Surface Disordering of Pb(100).....	
2.5.1	40
Results and Discussion.....	
2.6	47
Conclusions.....	
2.7	51
References.....	
Chapter 3	
Superheating of Bi(0001).....	53
3.1	53
Introduction.....	

3.2	Superheating of Crystallites in the Electron Microscope.....	56
3.3	Experiment.....	62
3.4	Reflection High-Energy Electron Diffraction.....	64
3.5	Time-Resolved RHEED and the Laser System.....	73
3.6	Results and Discussion.....	81
3.7	Laser-Induced Surface Damage of Bi(0001).....	91
3.8	Conclusions.....	97
3.9	References.....	99
Appendix A	Auger Electron and X-ray Photoelectron Spectroscopies.....	101
Appendix B	Hemispherical Energy Analyzer.....	103
Appendix C	Prediction of the Dependence of the Forward-Scattering Amplitude on Atomic Vibrations.....	105
Appendix D	Calculating the Surface Debye Temperature using RHEED.....	107
Appendix E	The Heat-Diffusion Model.....	115
Index.....		125

## List of Tables

<b>Table</b>	<b>Title</b>	<b>Page</b>
1	Properties of Bi and Pb.	56
2	The Debye Temperature of Low-Index Pb Surfaces from LEED and RHEED.	112
3	Heat-diffusion-Model Parameters for Time-Resolved RHEED on Bi(0001).	121
4	Heat-diffusion-Model Parameters for Time-Resolved RHEED on Pb(111).	122

## List of Figures

<b>Figure</b>	<b>Title</b>	<b>Page</b>
1	The low-index surfaces of a face-centered-cubic solid.	2
2	Logarithm of the intensity attenuation versus temperature for the low-index faces of Pb.	4
3	Surface cleanliness of Pb(100) confirmed with x-ray photoelectron spectroscopy.	15
4	The Pb(100) surface with some of the azimuths indicated.	17
5	Simple geometry shows x-ray photoelectron diffraction peaks at (a) $\theta = 0^\circ, 18^\circ, 45^\circ,$ and $72^\circ$ for the [001] azimuth and at (b) $\theta = 0^\circ, 19^\circ, 35^\circ,$ and $55^\circ$ for the [011] azimuth of the Pb(100) surface.	18
6	The x-ray photoelectron diffraction technique.	20
7	The method of data correction for a polar scan of the [001] azimuth of Pb(100) at $T = 326 \pm 0.6$ K.	21
8	The logarithm of the corrected forward-scattered peak intensity, $\ln[I_{\text{corr}}(\theta, \phi, T)]$ , plotted as a function of temperature for various angles along the [001] azimuth of Pb(100).	23
9	The logarithm of the corrected forward-scattered peak intensity, $\ln[I_{\text{corr}}(\theta, \phi, T)]$ , plotted as a function of temperature for various angles along the [011] azimuth of Pb(100).	24
10	The atomic-scattering factor for high-kinetic energies is strongly peaked in the forward direction.	26
11	Schematic diagram of the processes included in the SSC model.	28
12	The logarithm of the corrected forward-scattered intensity plotted as a function of temperature for $\theta = 0^\circ, 18^\circ, 45^\circ,$ and $72^\circ$ along the [001] azimuth of Pb(100) in the region of exponential intensity attenuation.	32
13	An experimental polar scan compared to the polar scan predicted by the single-scattering cluster model, when surface relaxation and thermal expansion are included, for the [001] azimuth of Pb(100) at $T = 350$ K.	35

<b>Figure</b>	<b>Title</b>	<b>Page</b>
14	An experimental polar scan compared to the polar scan predicted by the single-scattering cluster model, when surface relaxation and thermal expansion are included, for the [011] azimuth of Pb(100) at $T = 350$ K.	36
15	The logarithm of the forward-scattered intensity plotted as a function of temperature for the single-scattering cluster model including surface relaxation and thermal expansion for (a) $\theta = 0^\circ, 18^\circ,$ and $45^\circ$ along the [001] azimuth and (b) $\theta = 0^\circ, 19^\circ,$ and $35^\circ$ along the [011] azimuth.	37
16	The logarithm of the corrected forward-scattered intensity normalized to the exponential fit, $\ln[I_{\text{corr}}(\theta, \phi, T)/I_{\text{DW}}(\theta, \phi, T)]$ versus $\ln(T_m - T)$ .	42
17	The corrected forward-scattered intensity, $I_{\text{corr}}(\theta, \phi, T)$ , normalized to the exponential fit, $I_{\text{DW}}(\theta, \phi, T)$ , plotted versus temperature for the [001] and [011] azimuths of Pb(100) for $\theta = 0^\circ$ and compared to normalized intensities for Pb(110).	45
18	The number of disordered layers on Pb(100) determined using Eq. (2.8) with $\lambda_{\text{eff}} = 10$ Å.	48
19	The rhombohedral structure of Bi.	55
20	The Bi(0001) surface is similar to a (111) simple-cubic surface.	57
21	The characteristic time of melting versus bias temperature extended to the time scales used in time-resolved RHEED experiments on Bi(0001).	60
22	The Bi(01 $\bar{1}$ 2) surface.	63
23	AES confirms the cleanliness of the Bi(0001) surface.	65
24	High-energy electrons at glancing incidence generate the RHEED pattern.	66
25	The Ewald sphere representation for RHEED.	68
26	A typical RHEED pattern for non-zero angle of incidence.	69
27	The reciprocal lattice of Bi(0001) can be determined using RHEED by obtaining diffraction pattern in two or more azimuthal directions.	72

<b>Figure</b>	<b>Title</b>	<b>Page</b>
28	The laser system used in the time-resolved RHEED experiments.	75
29	The time-resolved RHEED setup.	76
30	The diffraction intensity is monitored using a linear-array detector aligned with the peak intensity of the diffraction streak of interest.	77
31	Time-resolved surface heating of Bi(0001) before, during, and after the arrival of the heating pulse at the surface.	78
32	The portion of the electron beam assumed to interact with the region of the surface probed by the electron beam.	79
33	A histogram of the multishot laser-beam uniformity.	80
34	A calibration to determine the temperature rise induced by the laser.	82
35	$I/I(T = 300 \text{ K})$ in Fig. 31 converted to $\Delta T$ .	84
36	The logarithm of the ratio of the heated streak intensity to the intensity at $T_{\text{bias}} = 523 \text{ K}$ versus peak laser intensity for various delay times.	85-6
37	Figures 34 and 36 combined to show the extension of Debye-Waller behavior above $T_m$ for both samples used in the experiment.	87
38	The ratio of the heated streak intensity to the intensity at the bias temperature versus delay time for various bias temperatures.	89-90
39	Laser-induced damage on Bi(0001) shows grating-like properties.	92
40	Scanning electron microscopy images of the undamaged and damaged Bi(0001) surface.	93
41	The scanning electron microscopy image of the laser-damaged surface with higher resolution.	94
42	The hemispherical energy analyzer used in the x-ray photoelectron diffraction experiments.	104
43	The parameters necessary for the calculation of the surface Debye temperature obtained using RHEED.	110
44	$\ln[I/I(T = 407 \text{ K})]$ plotted versus temperature for Pb(111).	111
45	$\frac{ \Delta \mathbf{k}_0 }{ \Delta \mathbf{k}_1 }$ versus $(M/\alpha)^{1/2}$ for Pb(111).	113

<b>Figure</b>	<b>Title</b>	<b>Page</b>
46	Temperature versus peak laser intensity plotted to confirm that $\Delta T = T - T_{\text{bias}}$ is linear in $I_p$ .	117
47	The heat-diffusion model calculated for laser-induced surface heating of Bi(0001).	118
48	The experimental setup used to measure the reflectivity of the sample as a function of temperature at the laser wavelength.	119
49	Experimental determination of the reflectivity of Bi(0001) at $\lambda = 1.06 \mu\text{m}$ as a function of temperature.	120
50	The heat-diffusion model for Bi(0001) and Pb(111) compared for the same laser energy absorbed at the sample surface.	123

## List of Abbreviations

AES	Auger electron spectroscopy
FWHM	full width at half maximum
LEED	low-energy electron diffraction
LIPSS	laser-induced periodic surface structure
MCP	microchannel plate
RHEED	reflection high-energy electron diffraction
SEM	scanning electron microscopy
SSC	single-scattering cluster
UHV	ultrahigh vacuum
XPD	x-ray photoelectron diffraction
XPS	x-ray photoelectron spectroscopy
YAG	yttrium aluminum garnet

## CHAPTER 1

### INTRODUCTION

#### 1.1: IMPORTANCE OF THE SURFACE IN THE THERMAL PROPERTIES OF THE BULK

Although the thermodynamics of melting is well understood, a comprehensive theory which treats the role of the surface and includes a microscopic treatment of melting still needs to be developed. Consequently, the experimental and theoretical study of surface melting has been a topic of current interest among surface scientists. The concept of surface melting (often used interchangeably with “surface disordering”) was proposed as early as 1860 by Faraday<sup>1</sup>, but it was not until 1985 that the first unambiguous observation of surface-induced melting was reported by Frenken and van der Veen.<sup>2</sup> Extensive studies on the low-index surfaces of Pb (and some other face-centered-cubic metals) comprise the vast majority of work to date on this subject. A diagram of the low-index faces of a face-centered-cubic crystal are given in Fig. 1.

It is well known that melting is initiated at free surfaces, grain boundaries, dislocations, and other defects.<sup>3,4</sup> A physical explanation for the observation of surface melting below the bulk melting temperature stems from the fact that a surface atom does not experience the same atomic forces as does an atom in the bulk. A surface atom has significantly fewer nearest neighbors than one in the bulk; hence its movement is less restricted. Thus, a surface atom experiences larger thermal vibrations than a bulk atom at the same temperature. The Lindemann criterion states that a solid will melt when the vibrational amplitude of its atoms exceeds a certain fraction of the interatomic spacing, typically 10%.<sup>5</sup> Hence, the surface “melts” at a lower temperature than the bulk, resulting in the existence of a disordered layer on the surface of an ordered crystal. For example, the low-index (111), (100), and (110) surfaces of a

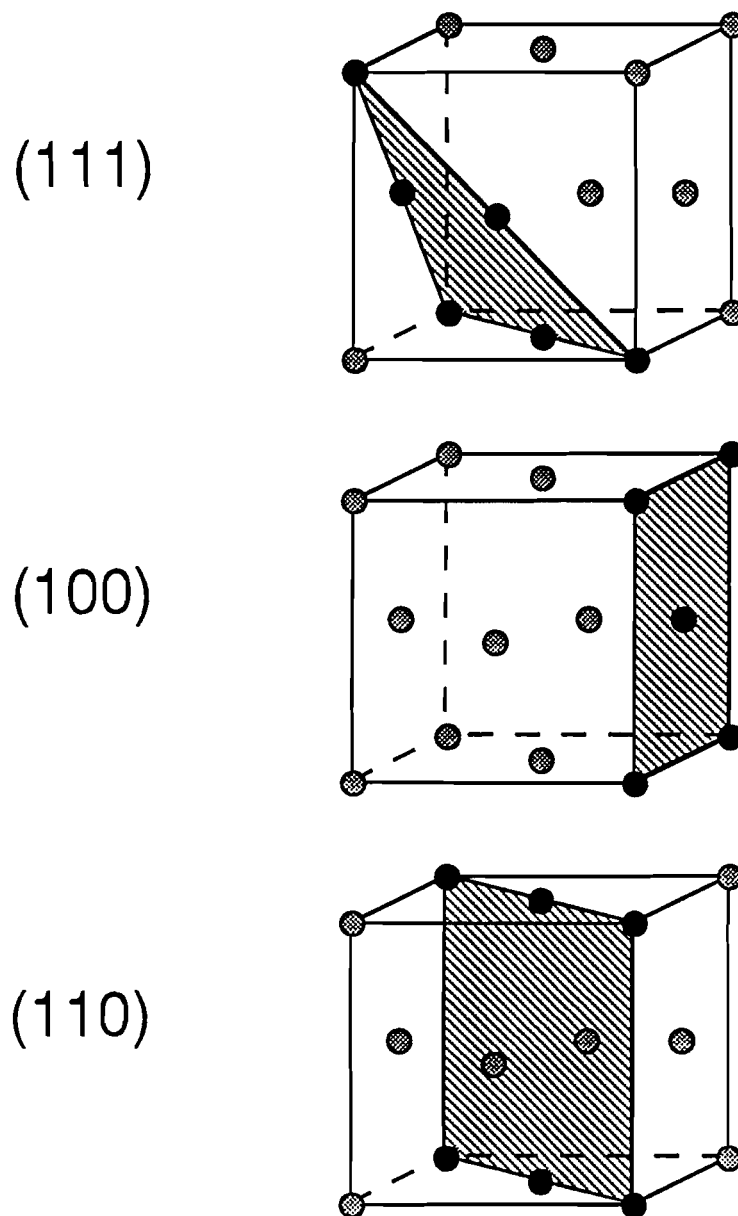


Fig. 1: The low-index surfaces of a face-centered-cubic solid.

face-centered-cubic crystal, which are shown in Fig. 1, have nine, eight, and seven nearest-neighbors, respectively, compared to twelve nearest neighbors for a bulk atom. This results in enhanced lattice vibrations, and in some cases, surface melting.

The effects of this reduction in nearest neighbors at the surface can be observed using diffraction techniques. For a bulk solid, the diffraction intensity generally decreases exponentially with temperature (Debye-Waller effect) until the bulk melting temperature is reached. This intensity attenuation is directly related to the thermal vibrations of the atoms, or equivalently, the Debye temperature. X-ray diffraction, for example, is commonly used to study the properties of the bulk due to the deep penetration of x-rays into the solid. To study surfaces, electron diffraction is often used because of the strong interaction between electrons and atoms which can be used to limit contributing regions to a near-surface layer. The increased vibrational amplitude of surface atoms results in an increased temperature dependence of the diffraction as compared to the bulk. The attenuation is generally exponential with temperature up until the onset of surface melting. Surface melting is observed as a deviation from this functional dependence. The result of the reduction in nearest neighbors on surfaces is manifested in the behavior of the (110), (111) and (100) surfaces of face-centered-cubic Pb, which have been shown to experience surface melting, no surface melting, and behavior intermediate to that seen on the other two surfaces, respectively. Intensity versus temperature plots for the low-index Pb surfaces, demonstrating the effect of a reduced number of nearest neighbors, are given in Fig. 2.<sup>6</sup>

Bulk melting is a first-order phase transition; i.e., it is characterized by a discontinuity in the first derivative of the Gibbs free energy at the melting temperature. This corresponds to the coexistence of the solid and its melt at the bulk melting temperature. In contrast, surface melting is a continuous process which proceeds until

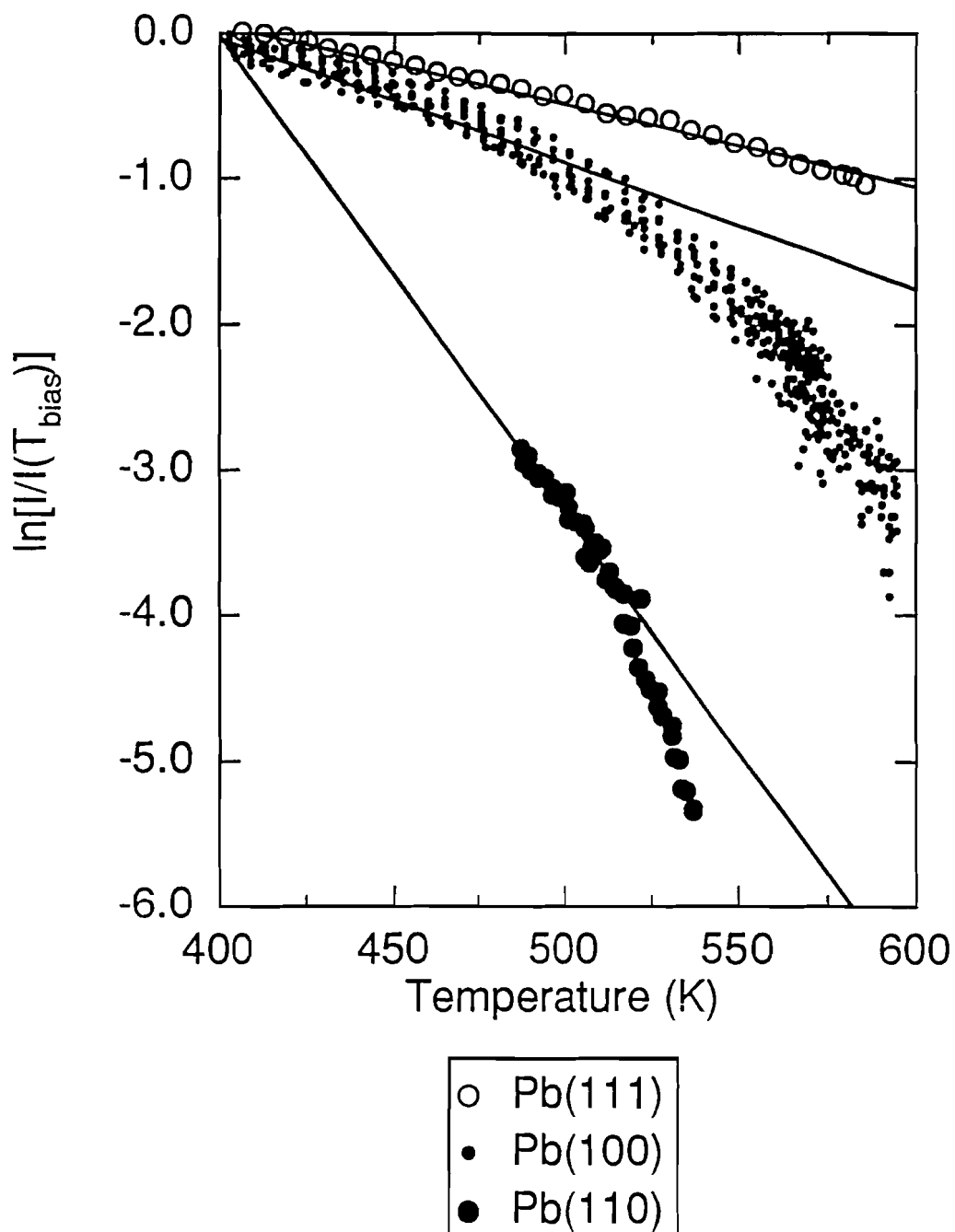


Figure 2: Logarithm of the intensity attenuation versus temperature for the low-index faces of Pb, adapted from Ref. 6. Notice the increased temperature dependence for more open surfaces.

the formation of a three-dimensional liquid at the bulk melting temperature. Surface melting is not a discontinuous phase transition, which makes surface melting an easier process to study than melting of the bulk.

If and at what temperature a solid experiences surface melting is governed by the energy associated with the formation of the disordered layer compared to the energy associated with the solid surface. It is energetically favorable for a disordered layer to form on the surface when

$$\Delta\gamma = \gamma_{sv} - (\gamma_{sl} + \gamma_{lv}) > 0, \quad (1.1)$$

where  $\gamma_{sv}$ ,  $\gamma_{sl}$ , and  $\gamma_{lv}$  are the interfacial free energies associated with the solid-vapor, solid-liquid, and liquid-vapor interfaces, respectively.<sup>2,7,8</sup> The interfacial free energies are element and surface specific and also depend on temperature. When  $\Delta\gamma \leq 0$  it is energetically favorable to have an ordered surface in direct contact with the vapor. Equation (1.1) only provides a qualitative explanation of why surface melting occurs. This is due to the fact that substantial error may occur in the determination of interfacial free energies, which of course limits the quantitative use of this equation.

The total interfacial free energy associated with the surface can be expressed as<sup>7</sup>:

$$\gamma = \gamma_{sl} + \gamma_{lv} + L_m \ell \left( 1 - \frac{T}{T_m} \right) + (\Delta\gamma)M_s, \quad (1.2)$$

where  $L_m \ell \left( 1 - \frac{T}{T_m} \right)$  is the energy cost associated with the undercooling of a liquid layer of thickness  $\ell$ ,  $L_m$  is the latent heat of melting per unit thickness,  $T$  is temperature, and  $T_m$  is the bulk melting temperature. The last term represents the gain

in energy associated with a solid being wetted by a liquid layer.  $M_s$  is a surface order parameter, the functional form of which depends on the interaction between an atom on the solid-liquid interface and one on the liquid-vapor interface.

In general, the thickness of the disordered layer is found to grow continuously once the temperature exceeds a characteristic onset temperature that depends on the physical properties of the surface and the bulk. However, there are exceptions to this case, some of which will be discussed later. In the general case discussed here, the disordered layer continues to increase in thickness until bulk melting occurs. As long as an ordered bulk lies beneath the surface layer, atomic motion in the surface layer will be more restricted than it would be in a true liquid. As the thickness of the disordered layer increases with temperature, the effective field that the bulk exerts on the surface atoms is screened; however, this effective field is present to some degree up until the formation of a bulk liquid.

Thermodynamically, two distinct regimes have been predicted and observed for the growth of a disordered layer on metals below the bulk melting temperature. When the surface layer is sufficiently thin, the growth is governed by a short-range Coulomb-like force between an atom on the liquid-vapor interface and an atom on the solid-liquid interface. In metals, conduction electrons screen longer range interactions when the thickness of the disordered layer is approximately the same magnitude as the lattice spacing.<sup>3</sup> For the appropriate form of  $M_s$ , minimization of Eq. (1.2) with respect to the thickness of the disordered layer leads to the prediction of logarithmic growth of the disordered layer, i.e.,

$$\ell \propto |\ln(T_m - T)| \quad (1.3)$$

As the thickness of the disordered layer increases even further, the short-range forces become negligible and only consideration of long-range van der Waals forces is necessary. For the form of  $M_s$  corresponding to this case, Eq. (1.2) has a minimum in this case which predicts power law growth of the disordered layer, i.e.,

$$\ell \propto (T_m - T)^{-1/3}. \quad (1.4)$$

The proportionality constant involves the term  $(\rho_l - \rho_s)$  where  $\rho_l$  and  $\rho_s$  are the liquid and solid densities, respectively. Therefore, the interfacial force is only repulsive for  $\rho_s > \rho_l$ , and growth is only predicted for samples whose liquid is less dense than the solid.<sup>8</sup> This suggests that it is possible for surfaces that form a disordered layer to reach a maximum thickness below the bulk melting temperature. In this case, no further growth occurs above a characteristic temperature up until the onset of bulk melting. Such behavior is anticipated for Bi since thermodynamics predicts that  $\Delta\gamma > 0$ , and Bi experiences a negative volume change upon melting.<sup>7,9</sup>

The initiation of melting at the surface is directly related to the fact that superheating is uncommon and infrequently observed. The presence of surfaces is the primary reason why superheating is very difficult to observe in comparison to supercooling. Liquids can easily be cooled below the bulk melting temperature because nucleation sites for the onset of crystallization are not readily available. However, in the case of superheating, the surface provides a massive nucleation site for bulk melting. Correspondingly, most of the successful attempts at superheating have been accomplished by suppressing the role of the surface in the bulk melting process, forcing nucleation of the melt to take place in the bulk. Some examples of superheating are: (1) *Internal heating of Sn and Cu rods*. While preferentially cooling the surface,

superheating by  $\sim 2$  K was observed.<sup>10,11</sup> (2) *Coating of Ag spheres with a uniform Au layer.* The Au layer provided a close lattice match and higher melting temperature, leading to an observed superheating temperature of at least 7.5 K.<sup>12</sup> (3) *Heating of nearly-perfect crystallites of exposed close-packed Pb(111) and Bi(0001) facets.* These crystallites have been observed to superheat by 2–3 K and 7–10 K, respectively.<sup>13–16</sup>

The fact that superheating is possible supports the generally accepted belief that the melting process requires nucleation. By suppressing the role of nucleation sites, such as free surfaces in (1) and (2), and crystal defects in (3), above, superheating has been achieved. If the nucleation theory of melting is indeed valid, as experimental evidence suggests, one might anticipate that superheating is possible with rapid heating and cooling of the surface at a rate fast enough to suppress the nucleation of the melt. In fact, this has been demonstrated for Pb(111)<sup>17</sup> and Bi(0001) with ultrafast surface heating with a pulsed laser; the latter case is discussed in detail in Chapter 3.

In Chapter 2 an angle-resolved x-ray photoelectron diffraction study of the temperature-dependent surface structure of Pb(100) is discussed. At the time of this experiment, the thermal properties of the Pb(110) and Pb(111) surfaces were relatively well known. Therefore, Pb(100), which had not yet been extensively studied, was chosen for these experiments in order to study the role of the packing of surface atoms in the surface melting process. The observed results support the hypothesis that the tendency to surface melt is dependent on the packing of surface atoms and is most likely on open surfaces. The temperature dependence of photoelectron diffraction peaks gives information about the temperature dependence of surface structure. Below  $550 \pm 11$  K, the decrease in diffraction intensity is exponential with temperature, which is the same functional temperature dependence as expected from the Debye-Waller

effect. However, this intensity attenuation of the diffraction peaks is much larger than predicted by x-ray photoelectron diffraction models for a bulk-like lattice. A detailed discussion of the data and the models is included in this Chapter. For higher temperatures, above  $550 \pm 11$  K, more rapid intensity attenuation is observed and is attributed to surface disorder. The rate of attenuation dramatically increases above approximately 585 K and evidence for logarithmic divergence of the thickness of the surface disordered layer is seen, along with a slight anisotropy which favors disordering along the [011] azimuth. Approximate methods for calculating the disordered layer thickness predict that approximately 2.1 monolayers are disordered at  $T = 597$  K on Pb(100).

In Chapter 3 a superheating experiment on the Bi(0001) surface using time-resolved reflection high-energy electron diffraction with  $\sim 200$ -ps time resolution is discussed. The previous observation of superheating of Bi crystallites<sup>15-16</sup>, as well as some of the unique properties of Bi which may provide a barrier to rapid melting<sup>18</sup>, make it more likely that superheating could be achieved on this close-packed surface than on many other surfaces. In fact, superheating by approximately 90 K is observed using this experimental technique. Larger temperature excursions above the bulk melting temperature result in melting accompanied by irreversible laser damage to the surface. The rhombohedral structure of Bi leads to very different behavior of material parameters upon melting as compared to face-centered-cubic metals. Therefore, the observation of superheating of Bi(0001), together with the previous report of superheating of Pb(111)<sup>17</sup> suggests the generality of the superheating phenomenon.

## 1.2 REFERENCES

1. M. Faraday, Proc. R. Soc. Lond. **10**, 440 (1860).
2. J. W. M. Frenken and J. F. van der Veen, Phys. Rev. Lett. **54**, 134 (1984); J. W. M. Frenken, P. M. J. Maree, and J. F. van der Veen, Phys. Rev. B **34**, 7506 (1986).
3. J. G. Dash, Contemp. Phys. **30**, 89 (1989).
4. J. W. M. Frenken, Endeavour **14**, 2 (1990).
5. D. P. Woodruff, *The Solid-Liquid Interface* (Cambridge University Press, London 1973).
6. J. W. Herman and H. E. Elsayed-Ali, submitted to Phys. Rev. B.
7. J. F. van der Veen, B. Pluis, and A. W. Denier van der Gon, *Chemistry and Physics of Solid Surfaces VII*, edited by R. Vaneslow and R. Howe (Springer-Verlag, Berlin 1988), pp. 455-490.
8. B. Pluis, A. W. Denier van der Gon, J. F. van der Veen, and A. J. Riemersma, Surf. Sci. **239**, 265 (1990); B. Pluis, D. Frenkel, and J. F. van der Veen, Surf. Sci. **239**, 282 (1990).
9. B. Pluis, T. N. Taylor, D. Frenkel, and J. F. van der Veen, Phys. Rev. B **40**, 1353 (1989).
10. S. E. Kaykin and N. P. Bene, C. R. Acad. Sci. USSR **23**, 31 (1939).
11. A. P. Baikov and A. G. Shestak, Sov. Tech. Phys. Lett. **5**, 569 (1979).
12. J. Daëges, H. Gleiter, and J. H. Perepezko, in *Phase Transitions in Condensed Systems—Experiments and Theory*, edited by G. S. Cargill, F. Spaepen, and K.-N. Tu (Materials Research Society, Pittsburgh, 1987), Vol. **57**, p. 67.
13. G. D. T. Spiller, Philos. Mag. A **46**, 535 (1982).
14. J. J. Métois and J. C. Heyraud, J. Phys. (Paris) **50**, 3175 (1989).
15. S. J. Peppiatt, Proc. R. Soc. Lond. A **345**, 401 (1975).
16. M. Blackman, S. J. Peppiatt, and J. R. Sambles, Nature (Phys. Sci.) **239**, 61 (1972).
17. J. W. Herman and H. E. Elsayed-Ali, Phys. Rev. Lett. **69**, 1228 (1992).
18. J. D. Mackenzie and R. L. Cormia, J. Chem. Phys. **52**, 6325 (1970).

**CHAPTER 2**  
**TEMPERATURE-DEPENDENT X-RAY PHOTOELECTRON**  
**DIFFRACTION OF Pb(100)\***

**2.1 INTRODUCTION**

In this chapter, an x-ray photoelectron diffraction (XPD) study of the dependence of the diffraction intensity of the [001] and [011] azimuths of Pb(100) on temperature, both below and above the temperature for the onset of surface disorder is discussed. XPD is a highly surface-sensitive probe of crystallographic structure. The temperature dependence of the diffraction resulting from the surface structure provides a direct method of observing surface disordering. The open Pb(110) and the close-packed Pb(111) surfaces have been shown to experience and not experience surface melting, respectively. However, the behavior of the Pb(100) surface, which has an intermediate packing of surface atoms, had not been extensively studied at the time of this experiment.

Below the onset of surface disorder ( $300 \text{ K} \leq T \leq 550 \text{ K}$  where the bulk melting temperature  $T_m$  of Pb is 601 K), the experimental results of this XPD study of Pb(100) are compared to the predictions made by XPD models in order to better understand the observed thermal behavior. This analysis points to the need for further theoretical development in interpreting and predicting such data so that XPD may become a more quantitative tool in the study of temperature-dependent surface structural

---

\*contributing publications:

E. A. Murphy, H. E. Elsayed-Ali, Ken T. Park, Jianming Cao, and Y. Gao, Phys. Rev. B **43**, 12 615 (1991).

E. A. Murphy, H. E. Elsayed-Ali, Ken T. Park, and Y. Gao, to be published in Journ. Vac. Sci. Technol. A, NOV/DEC (1993).

behavior. In this temperature range, it is observed that the intensity attenuation of the diffraction peaks is exponential with temperature. The intensity attenuation is much greater than that predicted by the single-scattering cluster (SSC) model, including the Debye-Waller factor, for the diffraction peaks from a bulk-like lattice. Both surface relaxation and thermal expansion are included in the SSC model; however, the inclusion of such effects only results in slightly improved agreement between experiment and calculation. A slab-like multiple-scattering calculation that assumes a bulk-like lattice does not show significant improvement in the agreement with the experimental results.<sup>1</sup>

The second half of this Chapter includes a study of the temperature-dependent behavior of Pb(100) for T lying between 550 K, where Pb(100) begins to experience surface disordering, and  $T_m$ . It is found that Pb(100) experiences an attenuation of the forward-scattered intensity which, above  $550 \pm 11$  K, no longer exhibits the same functional dependence as the Debye-Waller effect; i.e., the intensity attenuation is no longer exponential with temperature. Above  $585 \pm 5$  K the rate of intensity attenuation increases and is attributed to the growth of a surface disordered layer. Slight anisotropy is seen upon disordering with the [011] azimuth experiencing a faster intensity attenuation. By comparing these results with previous experiments on Pb(110),<sup>2-4</sup> the disordered layer thickness on Pb(100) is estimated to be about 2.1 monolayers at  $597 \pm 0.6$  K. This is in reasonable agreement with more recent ion shadowing and blocking experiments on Pb(100) which measure a disordered layer thickness of 1.3 monolayers at and above this temperature.<sup>5</sup>

## 2.2 X-RAY PHOTOELECTRON DIFFRACTION

XPD is a probe of short-range order in which incident x-rays result in the ejection of electrons from core energy levels. These electrons are then attracted by nearby ions, resulting in enhanced intensities along interatomic axes; this effect is called forward scattering. Since it is core-level electrons with element specific energies that are detected, XPD is especially applicable in the study of phenomena such as: the orientation of adsorbed species on substrates, epitaxial growth, and interdiffusion at interfaces, in which chemical composition and structure are both important.<sup>1,6,7</sup> More recently, XPD has been extended to the study of temperature-dependent surface effects such as the Debye-Waller effect and surface disordering below the bulk melting temperature<sup>2,8,9</sup> due to its high surface sensitivity and the fact that the angular intensity distribution can be used to characterize the degree of surface order.<sup>10</sup> For electron energies of several hundred electron volts, multiple scattering defocuses electrons emitted below approximately four atomic layers.<sup>10</sup> Hence, XPD is a highly surface sensitive probe.

## 2.3 EXPERIMENT

The Pb(100) crystal used in the experiment was oriented within  $0.75^\circ$  of the (100) orientation as confirmed by Laue back reflection. The sample was cut with a fine band saw to twice its final thickness, polished with silicon carbide grit paper, and finally chemically etched in a mixture of 80% glacial acetic acid and 20% hydrogen peroxide (30% in water) until a mirror-like finish was obtained. Prior to insertion in the ultrahigh vacuum (UHV) chamber, the sample was again chemically etched.

The sample was clipped to a resistively-heated molybdenum button heater mounted on a three-axis manipulator which also has polar and azimuthal rotation. Two

thermocouples monitored the temperature of the front and back surfaces of the sample. The maximum temperature difference across the sample was 1 K with temperature stability better than  $\pm 0.6$  K. Data were taken to within  $1.7 \pm 0.6$  K of  $T_m$ . Reported errors in excess of  $\pm 0.6$  K result from a slight variation in the temperature dependence of each forward-scattered peak. The thermocouples were calibrated to the freezing and boiling temperatures of water, and to the melting temperature of Pb by melting the sample *in situ* at the conclusion of the experiment.

Before data acquisition, the sample was cleaned with cycles of argon-ion bombardment, and by annealing to approximately 2 K below  $T_m$  until an atomically clean surface was obtained as indicated by x-ray photoelectron spectroscopy (XPS). Oxygen and carbon levels were checked throughout the experiment with XPS of the 1s transition for both elements. See Fig. 3(a). Auger electron spectroscopy (AES) was occasionally used to confirm the XPS results. See Appendix A for a brief discussion of the XPS and AES processes. A magnesium  $K\alpha$  x-ray source ( $E = 1253.6$  eV) at  $28.8^\circ$  from the surface normal provided the incident radiation. The binding energy of the  $4f_{7/2}$  core-level photoelectrons is 136.6 eV; therefore, the photoelectrons have a kinetic energy of 1117.0 eV above the Fermi level. The electrons are detected using a hemispherical energy analyzer mounted on a two-axis goniometer. The analyzer is described in Appendix B. The resolution of the analyzer as determined with low-energy electron diffraction (LEED) is  $1.6^\circ$  full width at half maximum. The base pressure of the UHV system is  $< 1 \times 10^{-10}$  Torr. The actual pressure during the experiment was higher due to the x-ray source and heating of the sample. Sample orientation was confirmed with reflection high-energy electron diffraction and LEED.

Electrons with an energy of 1117.0 eV have an estimated inelastic mean-free path,  $\lambda_{in}$ , of 24 Å in Pb.<sup>11–13</sup> This corresponds to a maximum escape depth of 10

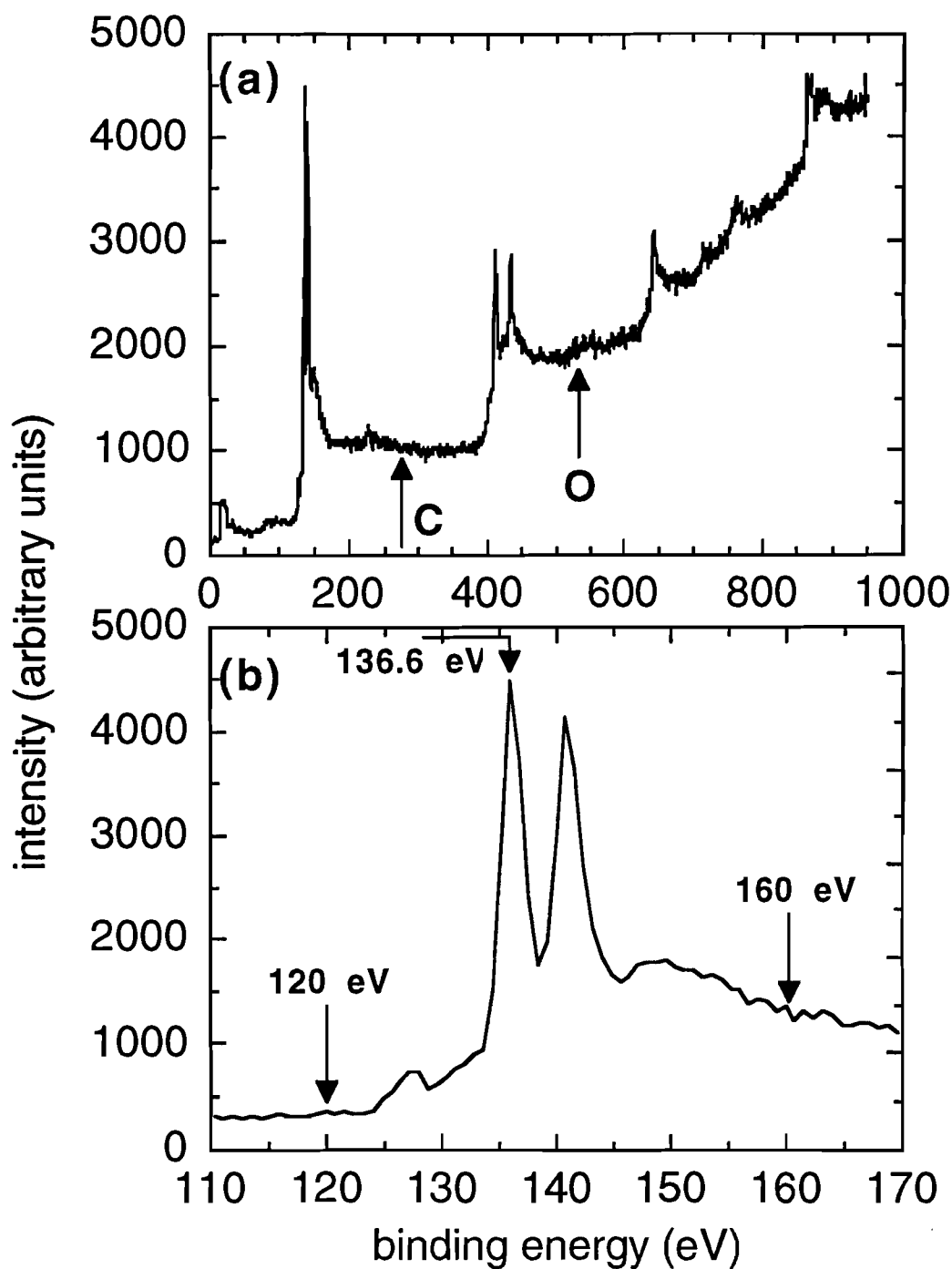
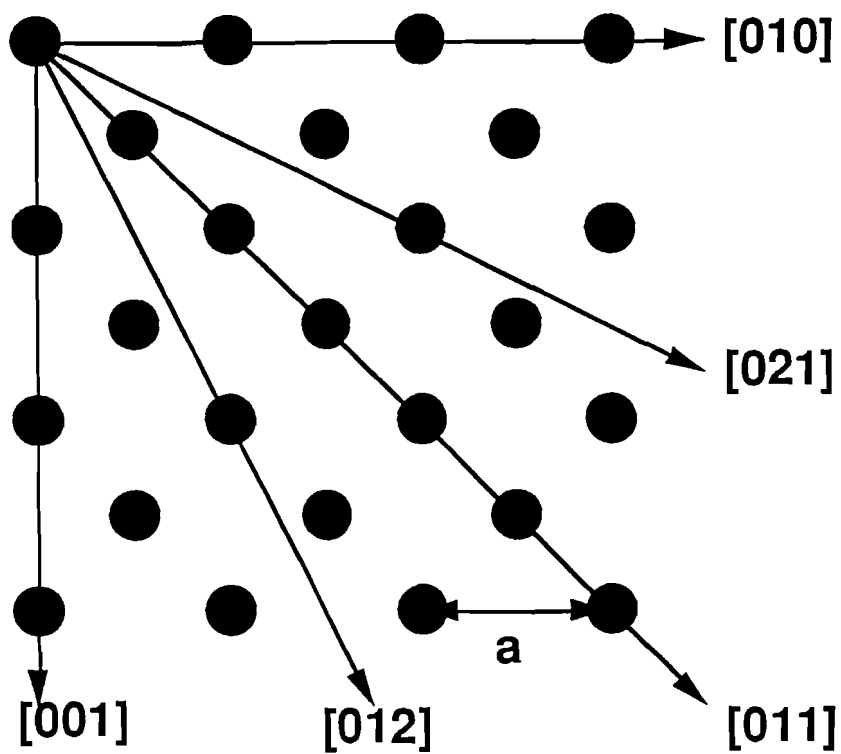


Figure 3: Surface cleanliness of Pb(100) confirmed with x-ray photoelectron spectroscopy. A full scan is shown in (a). The locations at which surface contaminants such as C and O would be present are labeled. Unlabeled peaks are from Pb. (b) Peak scans ( $Pb4f_{7/2}$ ) are taken at 136.6 eV, and off-peak scans are taken at 120 eV and 160 eV, as indicated.

monolayers for normal exit and 3 monolayers for  $\theta = 72^\circ$ , where  $\theta$  is the angle measured from the surface normal. However, multiple-scattering events effectively reduce  $\lambda_{\text{in}}$  and this must be taken into account in order to provide accurate predictions.<sup>14</sup> Unfortunately, such calculations are complicated and therefore are rarely incorporated in quantitative analysis. Recently, an effective electron mean-free path has been introduced that depends on both the elastic and inelastic mean-free paths; it has been suggested that multiple scattering can be partially accounted for in a single-scattering calculation by substituting  $\lambda_{\text{eff}}$  for  $\lambda_{\text{in}}$ , where  $0.5\lambda_{\text{in}} \leq \lambda_{\text{eff}} \leq 0.75\lambda_{\text{in}}$ .<sup>6,8,15</sup> The range in values results from a compilation of comparisons of XPD modeling techniques to experiment. The possible dependence of  $\lambda_{\text{eff}}$  on crystal direction is not accounted for here.

Figure 4 shows the atomic positions on the Pb(100) surface. Simple geometry predicts that forward-scattered peaks will be visible at  $0^\circ$ ,  $18^\circ$ ,  $45^\circ$ , and  $72^\circ$  for the [001] azimuth, and  $0^\circ$ ,  $19^\circ$ ,  $35^\circ$ , and  $55^\circ$  for the [011] azimuth for a non-relaxed (100) surface and are shown in Figs. 5(a) and 5(b). All eight of these peaks are analyzed. In these polar scans, forward-scattered peaks appear within  $1^\circ$  of these expected values, except for the peak at  $72^\circ$  which appears within  $2^\circ$ . Shifts in peak positions from what is predicted by simple geometry may be due to small errors in the spectrometer step size [ $(1 \pm 0.006)\theta$  for this experiment], interference effects, multilayer relaxation, and increased refraction for large  $\theta$ .<sup>10</sup> However, multilayer relaxation and refraction effects are ruled out for the peak predicted at  $72^\circ$  since both would result in a change opposite to what is observed. In addition, smaller peaks are observed at approximately  $32^\circ$  and  $58^\circ$  for [001] and  $68^\circ$  for [011]. These are due to first-order constructive interference at an off-axis angle which results when the phase difference between the two paths is  $2\pi$ .<sup>10</sup>



$a = 4.95$  angstroms

Figure 4: The Pb(100) surface with some of the azimuths indicated.

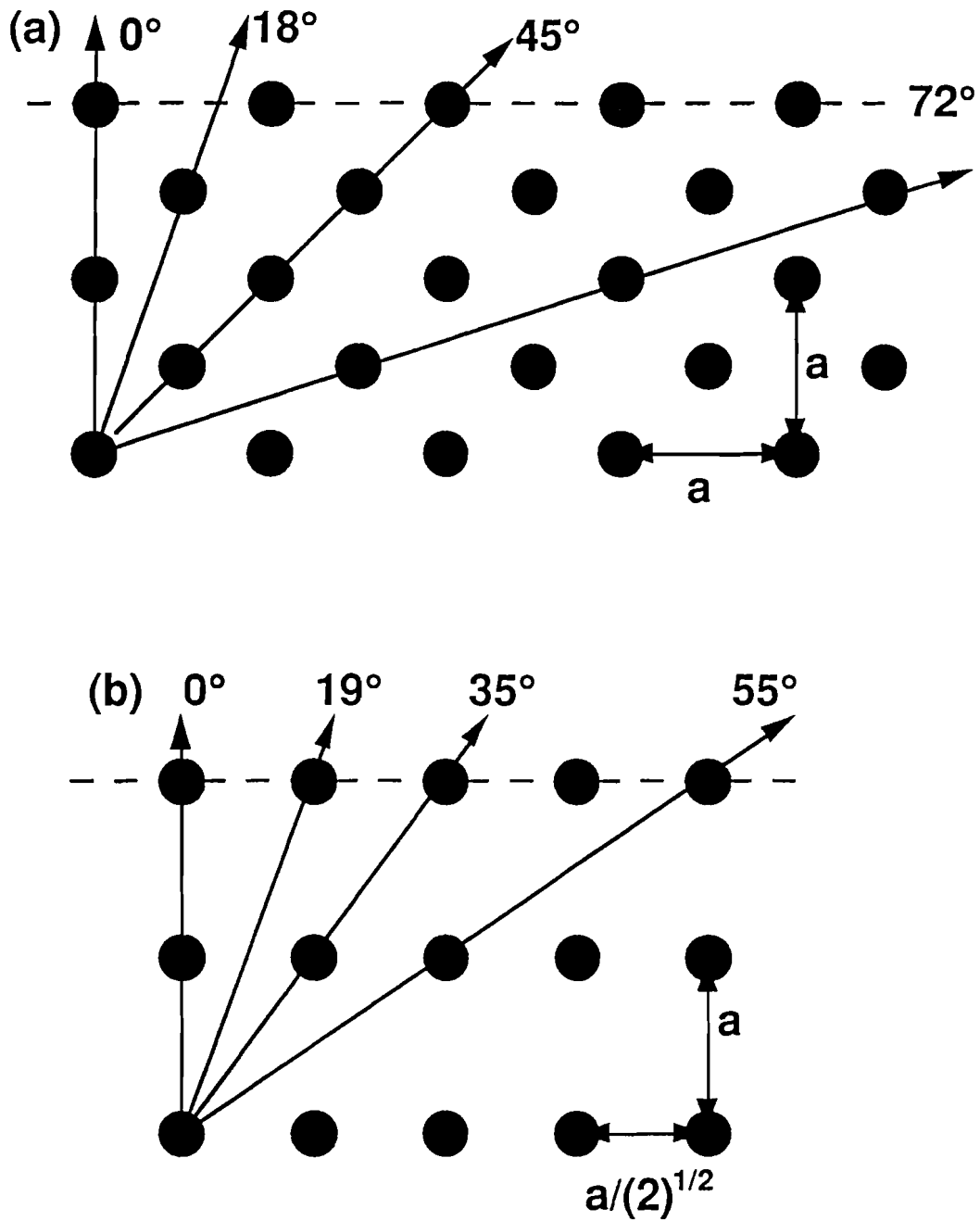


Figure 5: Simple geometry shows x-ray photoelectron diffraction peaks at (a)  $\theta = 0^\circ$ ,  $18^\circ$ ,  $45^\circ$ , and  $72^\circ$  for the [001] azimuth and at (b)  $\theta = 0^\circ$ ,  $19^\circ$ ,  $35^\circ$ , and  $55^\circ$  for the [011] azimuth of the Pb(100) surface.

The data acquisition was performed in the following manner. Polar scans were taken for electrons with a kinetic energy of 1117.0 eV and for two off-peak energies (1133.6 eV and 1093.6 eV) simultaneously with angular steps of  $1^\circ$ . Figure 6 demonstrates the acquisition of an XPD polar scan. The scans at the off-peak energies are used to determine instrumental effects. Background electrons are accounted for by fitting a polynomial to the highest-temperature scan after the remaining forward-scattered peaks are removed. At such high temperatures, approximately 1–2 K below  $T_m$ , the forward-scattered peaks are weak due to surface disordering. The instrumental response is determined from a polynomial fit to the scan at 1133.6 eV. The choice of this scan over the one at 1093.6 eV was originally made to avoid the effects of the secondary tail of the  $Pb4f_{7/2}$  peak (see Fig. 3(b)), although this is found to be unnecessary since the off-peak scans have the same shape and therefore only differ by a multiplicative constant. The data correction is accomplished as follows:

$$I_{\text{corr}}(\theta, \phi, T) = \frac{I(\theta, \phi, T) - I_{\text{bgd}}(\theta, \phi)}{I_{\text{ir}}(\theta)}, \quad (2.1)$$

where  $\phi$  is the azimuthal angle and is fixed for the polar scans.  $I(\theta, \phi, T)$ ,  $I_{\text{bgd}}(\theta, \phi)$ , and  $I_{\text{ir}}(\theta)$  are the as-acquired data, background, and instrumental response, examples of which are shown in Fig. 7(a).  $I_{\text{corr}}(\theta, \phi, T)$  is the corrected data given in Fig. 7(b) for the [001] azimuth of Pb(100) at  $T = 326 \pm 0.6$  K.  $\theta$  is the polar angle measured from the surface normal, and  $\phi = 0^\circ$  at the [001] azimuth.  $T$  is the temperature measured in degrees Kelvin.

The temperature dependence of the forward-scattered peaks is analyzed next. When  $\ln[I_{\text{corr}}(\theta, \phi, T)]$  is plotted versus  $T$ , it is seen that the intensity attenuation is

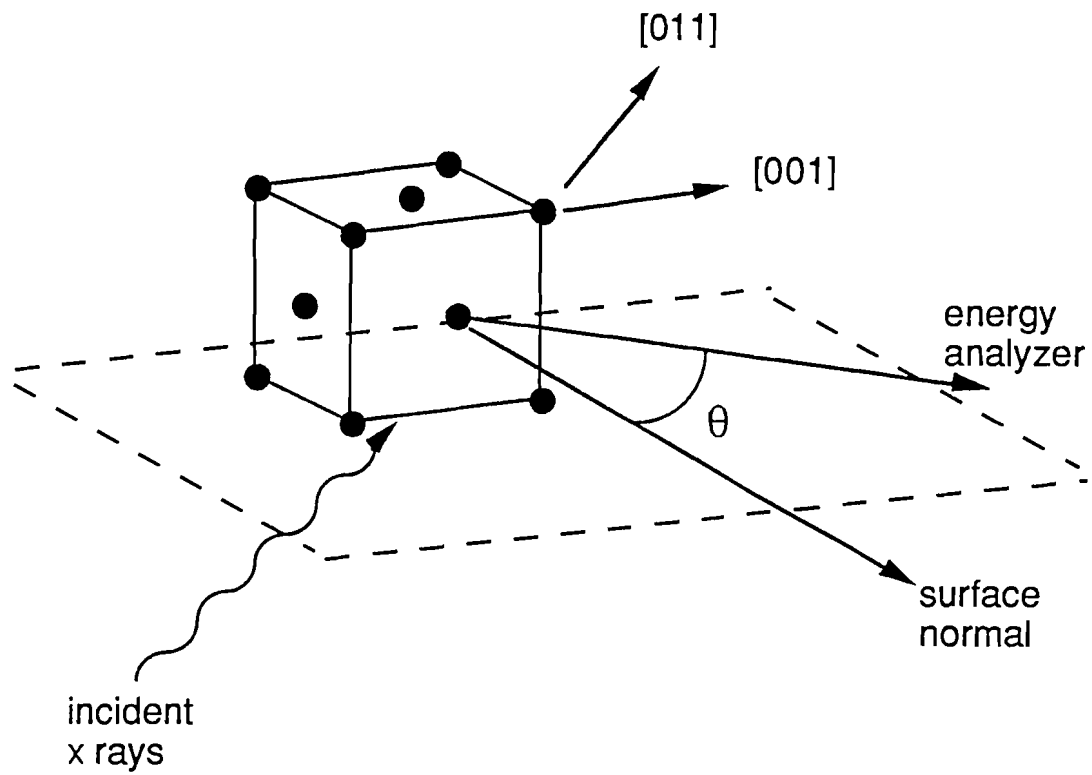


Figure 6: The x-ray photoelectron diffraction technique. X rays are incident at  $28.8^\circ$  from the surface plane.

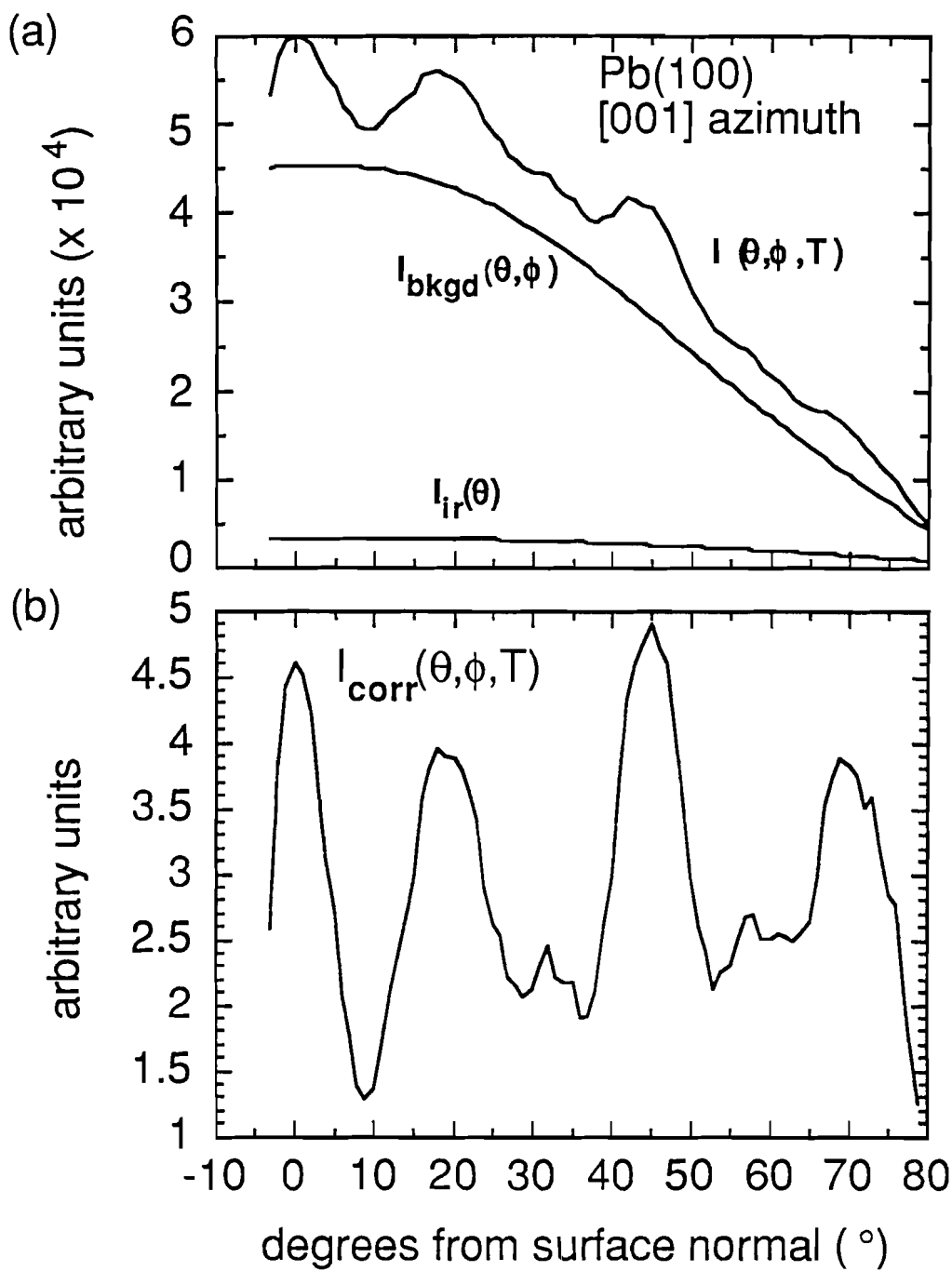


Figure 7: (a) The method of data correction for a polar scan of the [001] azimuth of Pb(100) at  $T = 326 \pm 0.6$  K. The as-acquired data, nonforward-scattered background, and instrumental response are given by  $I(\theta, \phi, T)$ ,  $I_{\text{bkgd}}(\theta, \phi)$ , and  $I_{\text{ir}}(\theta)$ , respectively. (b) The corrected forward-scattered intensity  $I_{\text{corr}}(\theta, \phi, T)$  is obtained from Eq. (2.1).

exponential with temperature up to  $550 \pm 11$  K. Above  $550 \pm 11$  K,  $\ln[I_{\text{corr}}(\theta, \phi, T)]$  versus  $T$  diverges rapidly from this exponential behavior. Figures 8 and 9 show  $\ln[I_{\text{corr}}(\theta, \phi, T)]$  versus  $T$  for  $\theta = 0^\circ, 18^\circ, 45^\circ,$  and  $72^\circ$  along the  $[001]$  azimuth and for  $\theta = 0^\circ, 19^\circ, 35^\circ,$  and  $55^\circ$  along the  $[011]$  azimuth. The best line fits are achieved using the method of least squares. The highest temperature data included in each fit is chosen so as to maximize the statistical correlation coefficient between the line fit and the data. At temperatures above  $550 \pm 11$  K the attenuation of the forward-scattered peaks is no longer exponential with temperature and additional phenomena other than a Debye-Waller-like effect are necessary to describe the observed behavior.

#### **2.4 TEMPERATURE-DEPENDENT X-RAY PHOTOELECTRON DIFFRACTION OF Pb(100): EXPERIMENTAL RESULTS AND THE SINGLE-SCATTERING CLUSTER MODEL**

In this section, the experimentally-observed intensity attenuation is compared with the SSC model<sup>6,7</sup>, and potential reasons for the discrepancies between observation and calculation are discussed. The relatively-simple SSC model has been successful in predicting surface structure and relative peak heights in photoelectron diffraction; however, the peak intensities are generally over predicted. Multiple scattering reduces the peak intensities and can be partially accounted for in the SSC model by reducing the mean-free path of electrons and the magnitude of the atomic-scattering factor. Often, detailed multiple-scattering calculations are necessary to achieve sufficient agreement with experiment.<sup>14,16</sup> In general, SSC calculations underestimate the dependence of the forward-scattered peaks on temperature. This has been demonstrated in temperature-dependent XPD azimuthal-scan studies of Cu(001)<sup>8</sup> and Ge(111).<sup>9</sup> While the Cu(001) experiment has shown reasonable agreement with the SSC method for the temperature dependence of forward-scattered peaks at large angles relative to the surface normal for which multiple scattering is not expected to be

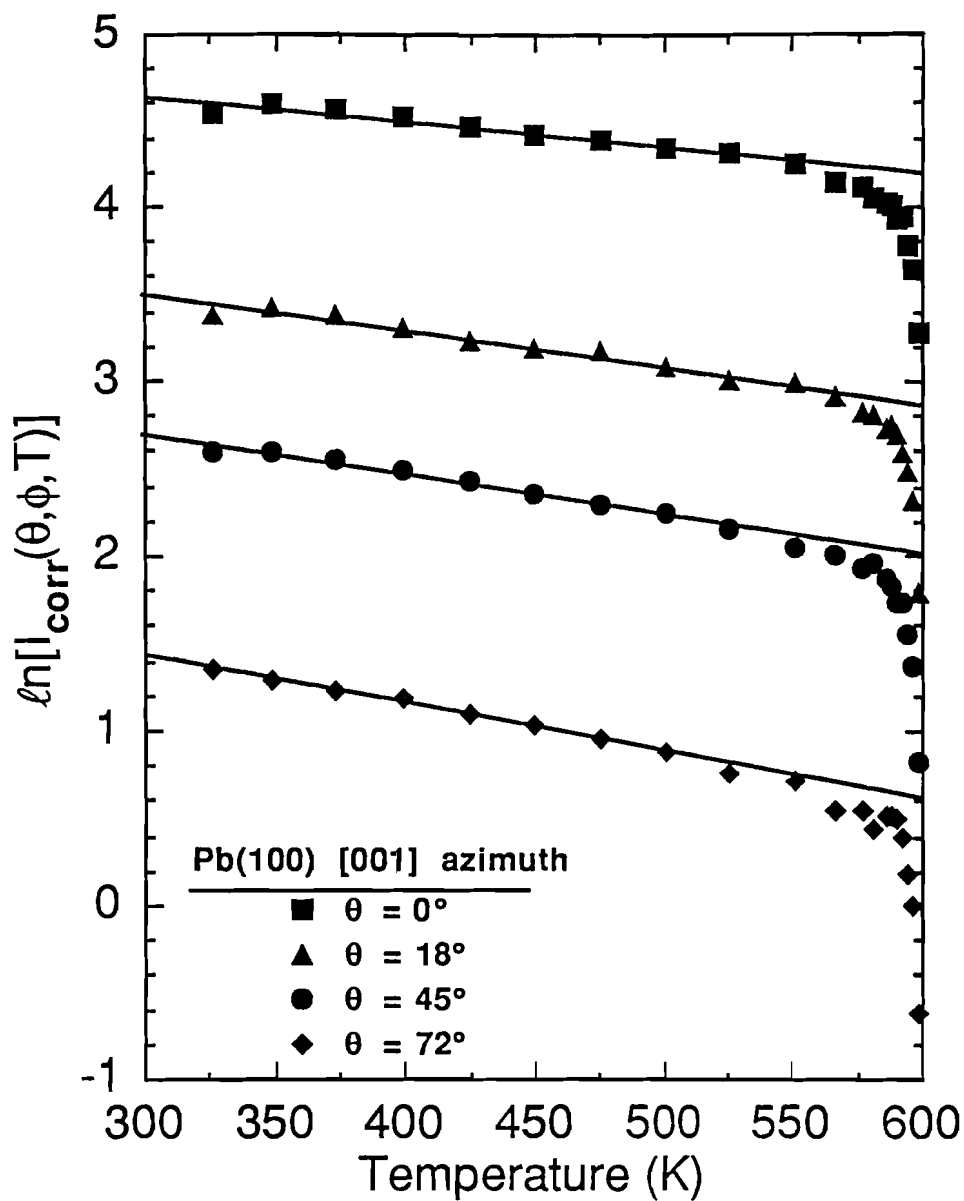


Figure 8: The logarithm of the corrected forward-scattered peak intensity,  $\ln[I_{\text{corr}}(\theta, \phi, T)]$ , plotted as a function of temperature for various angles along the [001] azimuth of Pb(100). Data have been shifted to eliminate overlap. The linear region for low temperature represents intensity attenuation which is exponential with temperature. Deviation from this behavior is seen above  $550 \pm 11$  K.

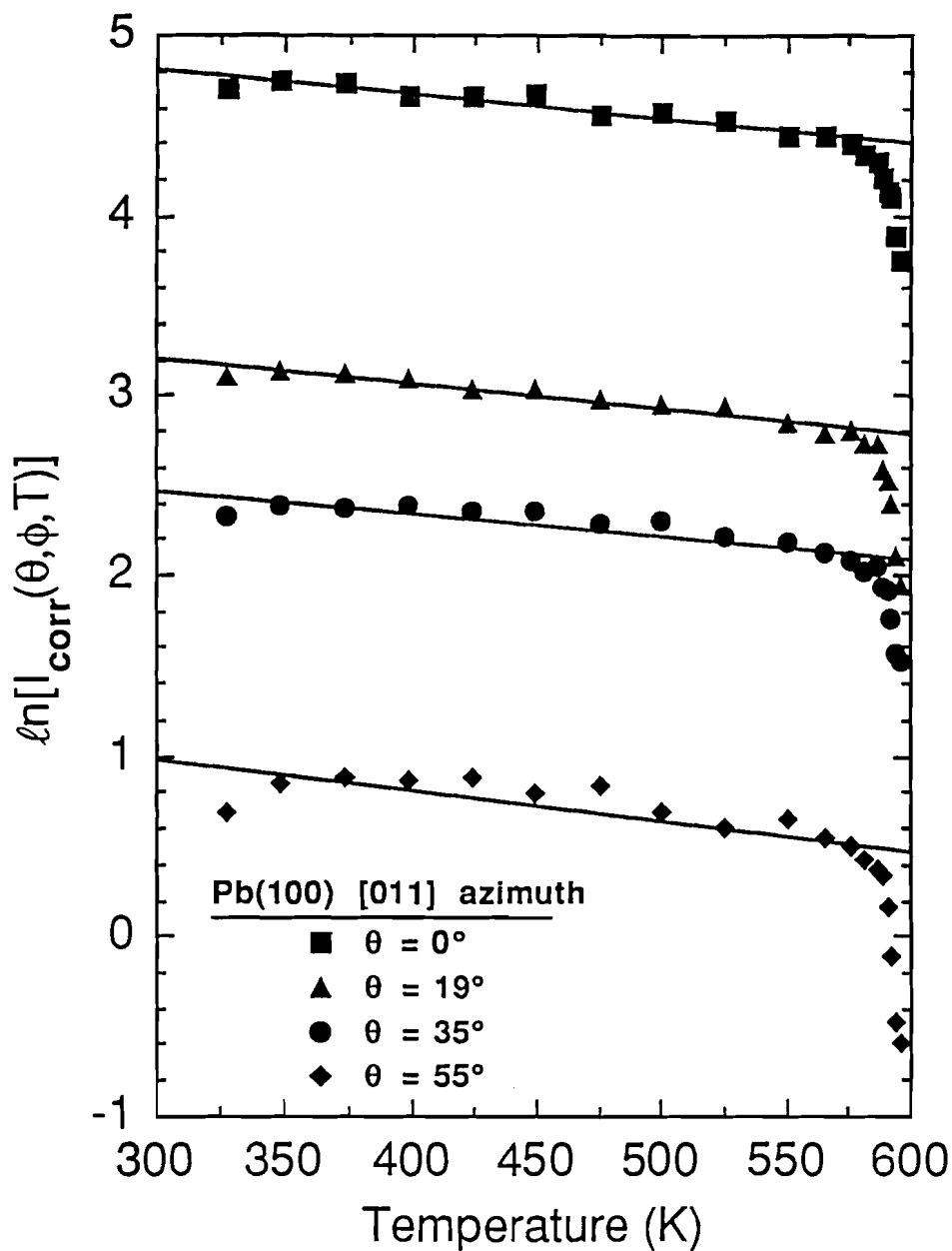


Figure 9: The logarithm of the corrected forward-scattered peak intensity,  $\ln[I_{\text{corr}}(\theta, \phi, T)]$ , plotted as a function of temperature for various angles along the [011] azimuth of Pb(100). Data have been shifted to eliminate overlap. The linear region for low temperature represents intensity attenuation which is exponential with temperature. Deviation from this behavior is seen above  $550 \pm 11$  K.

important, both studies suggest that multiple-scattering calculations are required for improved accuracy of the model.

#### 2.4.1 THE SINGLE-SCATTERING CLUSTER MODEL

Theoretically, an electron that is forward scattered immediately after being emitted experiences no Debye-Waller effect since it experiences no momentum change. See Appendix C for a calculation of the effect of lattice vibrations on forward scattering. The electrons contributing to a forward-scattered peak are either forward scattered immediately after being emitted, or elastically scattered one or more times before being scattered in the forward direction. The probability of another scattering event preceding forward scattering is quite low for electrons with kinetic energies >600 eV. This is due to the atomic-scattering factor, shown in Fig. 10 for a kinetic energy of 1000 eV, which is strongly peaked in the forward direction.<sup>17</sup> This property is responsible for the general success of the SSC method in predicting the structure and relative peak heights observed in XPD experiments.

In the SSC model, the photoelectron intensity,  $I(\mathbf{k})$ , is proportional to the absolute square of the sum of the electron wave amplitudes corresponding to forward scattering and single scattering; i.e.,

$$I(\mathbf{k}) \propto \left| \Psi_0(\mathbf{r}, \alpha) + \sum_j \Psi_j(\mathbf{r}_j, \alpha_j, \theta_j) \right|^2, \quad (2.2)$$

where  $\Psi_0$  and  $\Psi_j$  are the unscattered and scattered waves, respectively,  $\mathbf{r}$  designates the emitter to detector distance,  $\mathbf{r}_j$  is the emitter to scatterer distance, and  $\alpha$  and  $\alpha_j$  are the scattering angles between the surface and  $\mathbf{r}$  and the surface and  $\mathbf{r} - \mathbf{r}_j$ , respectively.

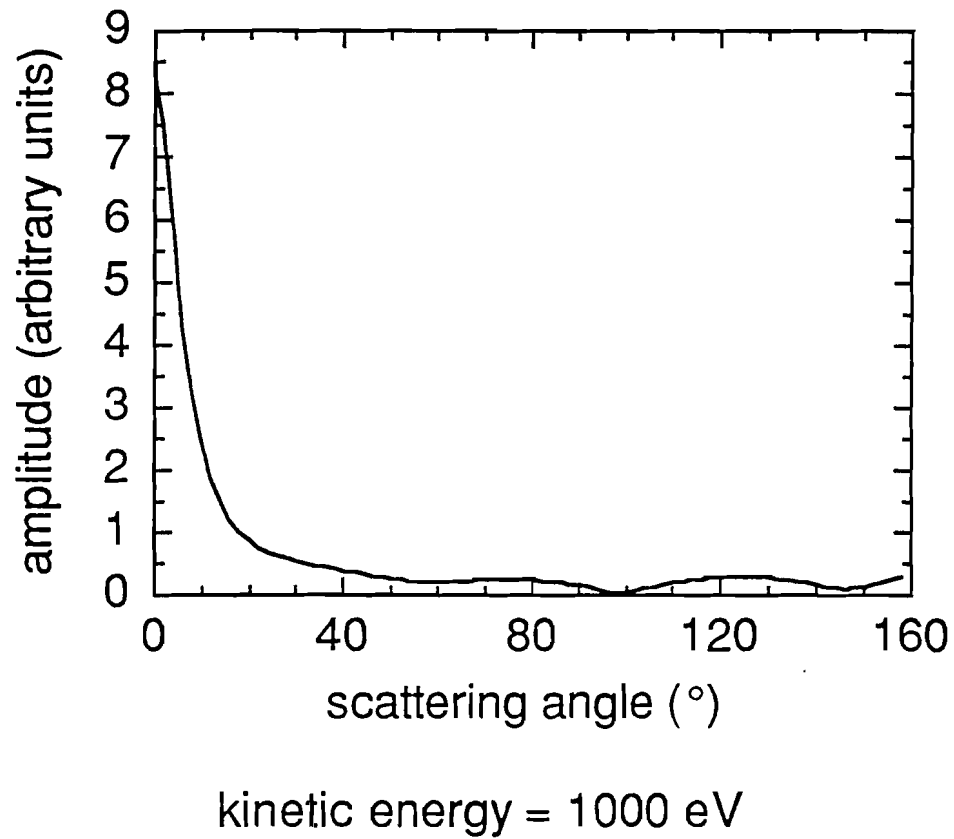


Figure 10: The atomic-scattering factor for high-kinetic energies is strongly peaked in the forward direction. From Ref. 17.

See Fig. 11 for these parameters.  $\theta_j$  is the scattering angle measured from the direction of forward scattering. Since the detector is situated at essentially infinity along  $\mathbf{k}$ , the unscattered and scattered waves are assumed to be spherical. For photoemission at high kinetic energies, the outgoing unscattered spherical wave associated with the emitted core-level electron can be expressed as

$$\Psi_0(\mathbf{r}, \alpha) = \left[ \frac{d\sigma_{n\ell}}{d\Omega} \right]^{1/2} \frac{\exp(i|\mathbf{k}|r)}{r}, \quad (2.3)$$

where  $\frac{d\sigma_{n\ell}}{d\Omega}$  is the differential cross section for the ionization event and  $n, \ell$  are the principle and angular momentum quantum numbers, respectively, corresponding to the core level from which the electron is ejected.  $|\mathbf{k}|$  is magnitude of the electron wave vector.

$$\Psi_j(\mathbf{r}_j, \alpha_j, \theta_j) = \Psi_0(\mathbf{r}_j, \alpha_j) |f(\theta_j)| \frac{\exp\{i[|\mathbf{k}||\mathbf{r} - \mathbf{r}_j| + \gamma_j(\theta_j)]\}}{|\mathbf{r} - \mathbf{r}_j|} \quad (2.4)$$

is the wave scattered by scatterer  $j$  at  $\mathbf{r}_j$  in the direction of  $\mathbf{k}$ .  $f(\theta_j) = |f(\theta_j)| \exp[i\gamma_j(\theta_j)]$  is the complex plane-wave scattering factor where  $\gamma_j(\theta_j)$  is the phase change resulting from the scattering. A spherical-wave scattering factor would result in a reduced forward-scattering amplitude. In this model, spherical-wave effects are accounted for by using a reduction factor,  $\beta$ . This reduction is usually around 50%, which corresponds to  $\beta = 2$ .<sup>6,7</sup> The angle  $\alpha$  is equal to  $90^\circ - \theta$  and is used here to avoid confusion between  $\alpha_j$  and  $\theta_j$ . In this model the differential cross section for both the scattered and unscattered parts is approximated to be the same since only  $\alpha \approx \alpha_j$  will

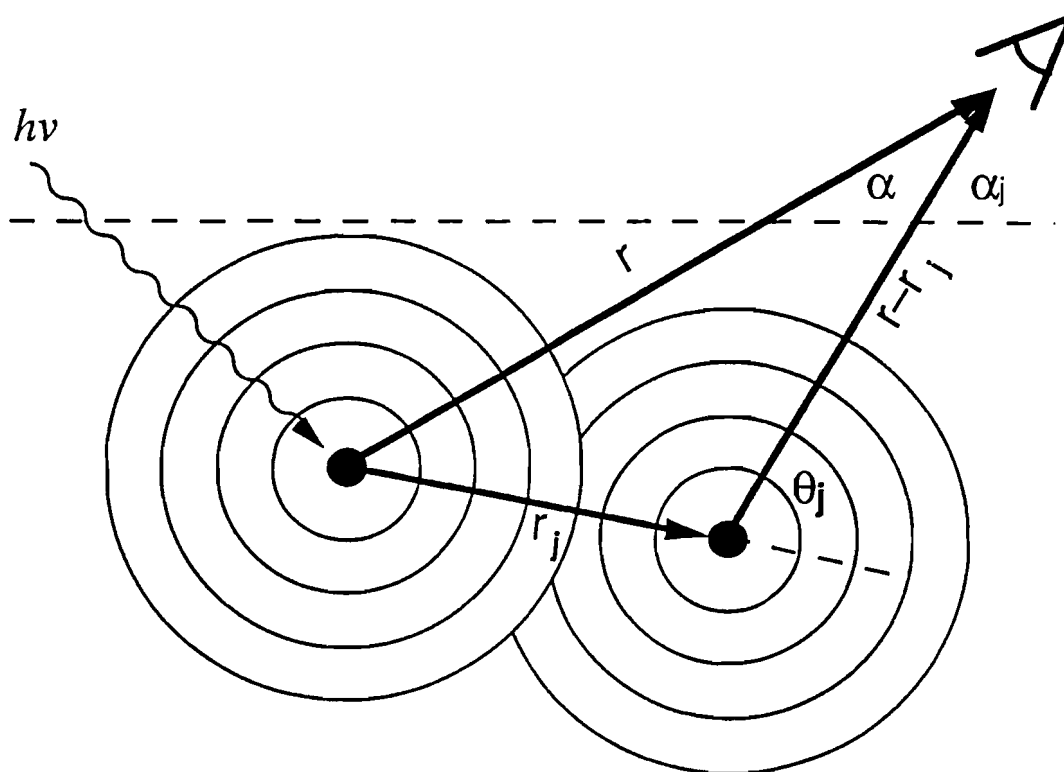


Figure 11: Schematic diagram of the processes included in the SSC model.  $|\mathbf{r}|, |\mathbf{r}-\mathbf{r}_j| \gg |\mathbf{r}_j|$  so that  $\mathbf{r}$  is essentially parallel to  $\mathbf{r}-\mathbf{r}_j$ . Therefore, it can be assumed that the angle between  $\mathbf{r}$  and  $\mathbf{r}_j$  is  $\theta_j$  and that  $\mathbf{r}$  and  $\mathbf{r}-\mathbf{r}_j$  are at an angle  $\alpha$  and  $\alpha_j$  above the surface, respectively.  $h\nu$  is the energy of the incident x rays and the dashed line indicates the surface.

result in significant scattering. The phase difference between  $\Psi_0$  and  $\Psi_j$  is  $|\mathbf{k}|r_j(1 - \cos\theta_j) + \gamma_j(\theta_j)$ .  $|\mathbf{r}-\mathbf{r}_j|$  is replaced with  $|\mathbf{r}|$  in the denominator of Eq. 2.4. The attenuation due to inelastic scattering, which decays exponentially with the distance traveled in the sample by the electrons divided by the mean-free path of the electrons, must also be accounted for. By factoring out common terms, the single-scattering diffraction intensity for unpolarized incident photons can be written as<sup>6,7</sup>

$$I^{(n)}(\mathbf{k}) \propto \left| \exp\left(\frac{-L_n}{2\lambda}\right) + \sum_j \frac{|f_j(\theta_j)|}{\beta r_j} W_j \exp\left(-\frac{L_j + r_j}{2\lambda}\right) \exp\left\{i\left[|\mathbf{k}|r_j(1 - \cos\theta_j) + \gamma_j(\theta_j)\right]\right\} \right|^2 \\ + \sum_j \frac{|f_j(\theta_j)|^2}{\beta^2 r_j^2} \exp\left(-\frac{L_j + r_j}{\lambda}\right) (1 - W_j^2) \quad (2.5)$$

for an emitter in the  $n$ th layer.  $L_n = \frac{z_n}{\cos\theta}$  is the path of the electron wave inside the solid,  $z_n$  is the distance between the  $n$ th layer and the surface,  $\theta$  is the polar angle defined from the surface normal, and  $\lambda$  is the mean-free path of electrons in the solid.  $W_j$  is the Debye-Waller factor which accounts for the increased atomic vibrational amplitude with temperature, where

$$W_j \propto \exp\left[-|\Delta\mathbf{k}_j|^2 \langle u_j^2(T) \rangle\right] \propto \exp\left[-2|\mathbf{k}|^2 (1 - \cos\theta_j) \langle u_j^2(T) \rangle\right] \quad (2.6) \\ \text{and } \langle u_j^2(T) \rangle = \frac{3\hbar^2 T}{M k_B \theta_D^2}.$$

$|\Delta\mathbf{k}_j|$  is the magnitude of the momentum change resulting from scattering with the  $j$ th atom,  $\langle u_j^2(T) \rangle$  is the mean-squared atomic displacement from equilibrium in the direction of  $\Delta\mathbf{k}_j$  and, in this instance, is assumed to be isotropic,  $\hbar$  is Planck's constant divided by  $2\pi$ ,  $M$  is the mass of the atom,  $k_B$  is Boltzmann's constant, and  $\theta_D$  is the Debye temperature. Since at high energies the scattering is primarily in the forward direction (i.e.,  $\theta_j \approx 0^\circ$ ),  $W_j$  is nearly 1. Therefore, vibrational effects are not expected to be very significant for single scattering. The last term in Eq. (2.5) accounts for over counting of lattice-vibration effects in the first term since only products of unlike waves should include Debye-Waller factors.

The model also incorporates refraction effects resulting from the passing of the photoelectron through the solid-vacuum interface. This is estimated as scattering through a potential step equal to the inner potential,  $V_0$ .<sup>6,7</sup>

$$\theta' = \cos^{-1} \left[ \left( \frac{E}{E + V_0} \right)^{1/2} \cos \theta \right], \quad (2.7)$$

where  $E$  is the kinetic energy of the electrons and  $\theta'$  is the internal emission angle measured from the surface normal. This effect is quite small for high-energy electrons, and therefore  $\theta'$  is not mentioned elsewhere in this discussion; however, this effect is included in calculating the final exit angle of electrons in the model.

In these SSC calculations the small-atom approximation is made; i.e., a plane-wave electron wave function is assumed. The cluster size is  $9 \times 9 \times 15$  atoms, corresponding to a crystal with 81 atoms in each layer and 35 Å thick. The contribution of the bottom layer to the diffraction is <5% of the total intensity. The center atom of each layer is chosen as the emitter. Scattering factors based on free-atom scattering of incident plane waves are obtained from the literature.<sup>17</sup> Electrons with an

energy of 1117.0 eV have an estimated inelastic mean-free path,  $\lambda_{\text{in}}$ , of 24 Å in Pb.<sup>11–13</sup> Multiple-scattering events effectively reduce  $\lambda_{\text{in}}$ , and it has been found that using  $0.5 \lambda_{\text{in}} \leq \lambda_{\text{eff}} \leq 0.75 \lambda_{\text{in}}$  instead of  $\lambda_{\text{in}}$  is more consistent with experimental results.<sup>7,9,15</sup> For Pb,  $\theta_{\text{D}} = 62 \text{ K} [\theta_{\text{D}}(\text{bulk})/\sqrt{2}]$ ,  $\lambda = 12 \text{ Å} (0.5\lambda_{\text{in}})$ , and  $V_0 = 15 \text{ eV}$  are used in the model. In addition,  $\beta = 2$  is chosen. The diffraction intensity is calculated for  $300 \text{ K} \leq T \leq 600 \text{ K}$  in 50 K temperature intervals and  $1^\circ$  steps in  $\theta$ .

#### 2.4.2 RESULTS AND DISCUSSION

These XPD experiments clearly show that for  $T < 550 \pm 11 \text{ K}$ , the intensity attenuation of the forward-scattered peaks is exponential with temperature. However, the degree of attenuation significantly exceeds that predicted by XPD models which include the Debye-Waller factor. From Eq. (2.6) it is seen that the intensity attenuation with temperature depends on the value of  $\theta_{\text{D}}$ . Therefore, in the following discussion qualitative information about  $\theta_{\text{D}}$  is extracted from the data. Experimentally,  $\theta_{\text{D}}$  is a combination of surface and bulk effects.

First, the behavior of  $\theta_{\text{D}}$  as a function of the thickness of the surface layer contributing to the diffraction is investigated. The thickness of the contributing surface-layer is equal to the component of the electron mean-free path perpendicular to the surface,  $\lambda_{\text{eff}} \cos \theta$ . For a given azimuth, the transition from a bulk-like to a surface-like  $\theta_{\text{D}}$  can be observed by monitoring how the slope of the linear region changes with decreasing surface-layer thickness. Figure 12 shows data from which this trend in  $\theta_{\text{D}}$  can be observed as a function of surface-layer thickness for  $\theta = 0^\circ, 18^\circ, 45^\circ, \text{ and } 72^\circ$  along the [001] azimuth of Pb(100). Notice the obvious trend of increasing slope with increasing polar angle. This trend is less obvious for the [011] azimuth as there is less change in the slopes with increasing polar angle. The slopes for the [011] azimuth are

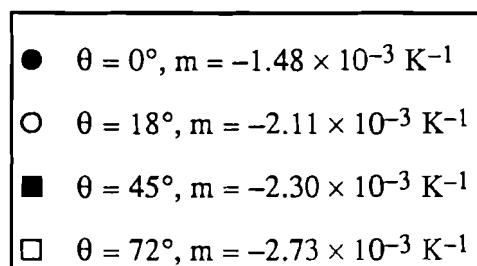
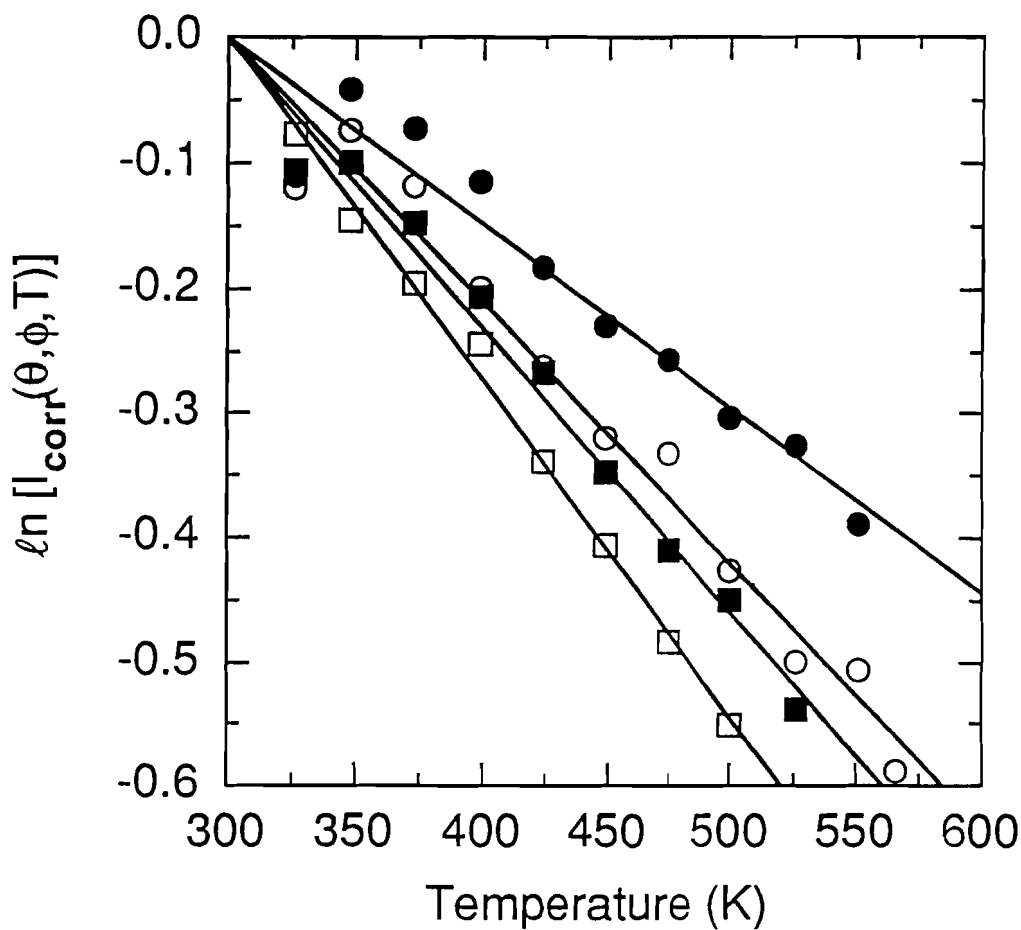


Figure 12: The logarithm of the corrected forward-scattered intensity plotted as a function of temperature for  $\theta = 0^\circ, 18^\circ, 45^\circ$ , and  $72^\circ$  along the [001] azimuth of Pb(100) in the region of exponential intensity attenuation. For the [011] azimuth the slopes are as follows:  $m(0^\circ) = -1.34 \times 10^{-3} \text{ K}^{-1}$ ,  $m(19^\circ) = -1.39 \times 10^{-3} \text{ K}^{-1}$ ,  $m(35^\circ) = -1.27 \times 10^{-3} \text{ K}^{-1}$ , and  $m(55^\circ) = -1.70 \times 10^{-3} \text{ K}^{-1}$ .

given in the caption of Fig. 12. The ~12% difference between the slopes for  $\theta = 0^\circ$  along [001] and [011] may be attributed to the relatively small number of data points that comprise the line fits or possibly to a slight tilt in the plane of crystal rotation relative to the electron-energy analyzer. However, the same trend in slopes for  $\theta = 0^\circ$  is observed in the SSC model as well. Comparing the experimental slopes corresponding to  $\theta = 0^\circ$  and  $\theta = 72^\circ$  for [001] (and  $\theta = 0^\circ$  and  $\theta = 55^\circ$  for [011]) it is seen that  $\theta_D$  decreases with the surface-layer thickness, i.e., as less and less of the bulk is sampled. From Eq. (2.6) one can calculate that  $\theta_D$  for a surface layer of ~2 monolayers ( $\theta = 72^\circ$ ) is approximately 70% of that obtained when ~5–7 monolayers are probed ( $\theta = 0^\circ$ ), assuming  $0.5\lambda_{in} \leq \lambda_{eff} \leq 0.75\lambda_{in}$  as discussed above. For  $\theta = 0^\circ$ ,  $\theta_D$  is a combination of both bulk and surface effects.

The SSC calculations described above are unsuccessful at providing reasonable agreement with the temperature dependence of the forward-scattered peaks that are observed for Pb(100). The slopes of  $\ln[I(\theta, \phi, T)]$  versus T are under predicted by the model by one to two orders of magnitude. This leads to the investigation of surface effects that have not yet been included in the model, such as surface relaxation and thermal expansion.

First, the fact that Pb(100) is not accurately modeled by a bulk-terminated surface is accounted for. In fact, unusually large surface relaxation has been observed on both Pb(100) and Pb(110) when compared to many other face-centered-cubic (100) and (110) metal surfaces. For example, the first interlayer contraction for Pb(100), Pb(110), Cu(001), and Ni(001) has been reported to be about 8%, 16%, 1%, and 3% respectively.<sup>18,19,20</sup> In addition, a large thermal expansion perpendicular to the surface has been observed for Pb(100) when  $300 \text{ K} \leq T \leq 470 \text{ K}$ . In this temperature range, the thermal-expansion coefficient is approximately  $2 \times 10^{-4} \text{ K}^{-1}$ ,

about seven times the bulk thermal expansion.<sup>21</sup> A large thermal expansion has also been observed for Pb(110) and Ni(001)<sup>20,22</sup>; however, no information on the thermal expansion of Cu(001) has been found in the literature.

The following corrections are made to the model: an 8.0% contraction to the first interlayer spacing, a 3.1% expansion to the second, and a 3.0% contraction to the third at 300 K.<sup>18</sup> Next, a thermal expansion of  $2 \times 10^{-4} \text{ K}^{-1}$  is included for the first interlayer spacing, and the SSC slopes are calculated for  $300 \text{ K} \leq T \leq 470 \text{ K}$ .<sup>21</sup> The SSC slopes including these effects show an increased temperature dependence; however, the change does not satisfactorily account for the discrepancy between the model and experiment. A polar scan including these corrections is given with the experimental data in Figs. 13 and 14 for  $T = 350 \text{ K}$  for the [001] and [011] azimuths, respectively. These plots show reasonable agreement with the experimental polar scans, especially for the first three peaks along [011]. However, the forward scattering along the nearest-neighbor direction,  $\theta = 45^\circ$  along [001], is still significantly overemphasized. This is most likely a result of not including multiple-scattering effects in the model. The calculated SSC slopes for several polar angles along [001] and [011] are obtained from plots of  $\ln(I)$  versus  $T$  for the two azimuths in Fig. 15.

When comparing the data and the model in Figs. 12 and 15, it is important to note that the model does not take into account the fact that a surface atom may experience a larger thermal vibrational amplitude perpendicular to the surface than parallel to it, or even that the vibrations in the plane of the surface may not be isotropic. In addition it does not account for a layer-dependent Debye temperature. Therefore, it is not surprising that the trend of increasing temperature dependence with increasing polar angle observed in the data is not observed in the calculation.

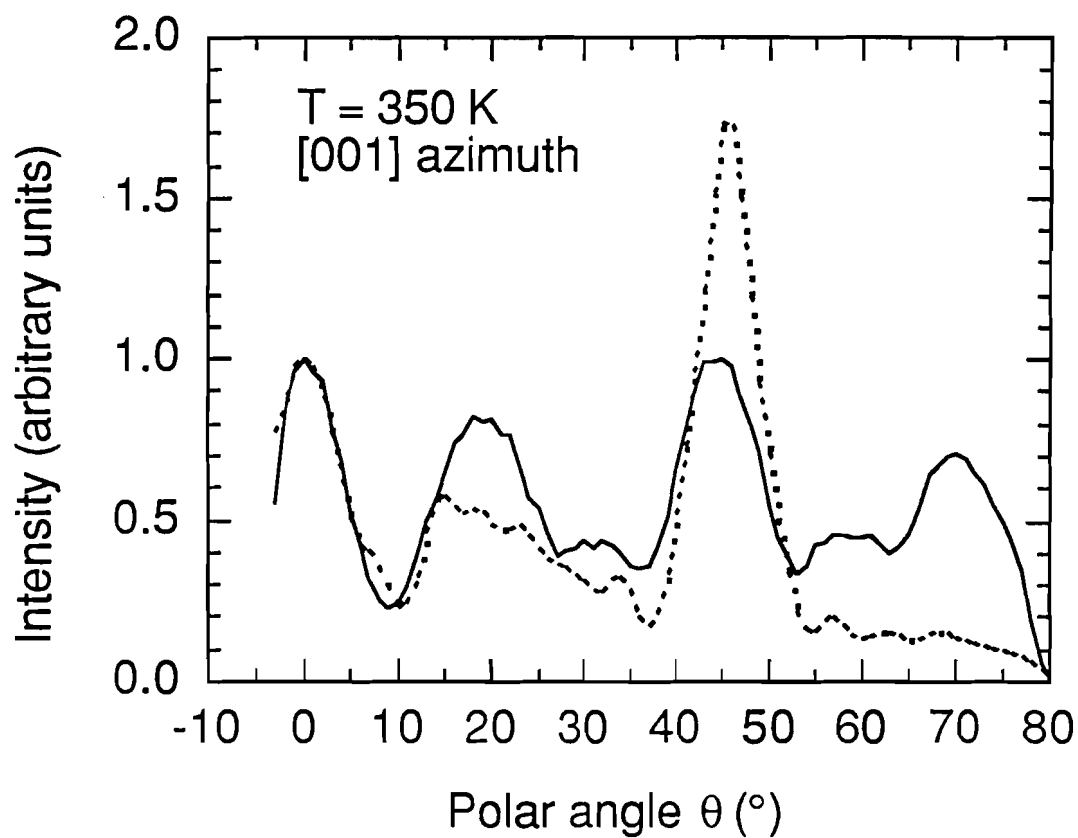


Figure 13: An experimental polar scan compared to the polar scan predicted by the single-scattering cluster model, when surface relaxation and thermal expansion are included, for the [001] azimuth of Pb(100) at  $T = 350$  K. The scan is normalized to unity for the peak at  $0^{\circ}$ . Solid and dashed lines represent the experimental data and the model, respectively.

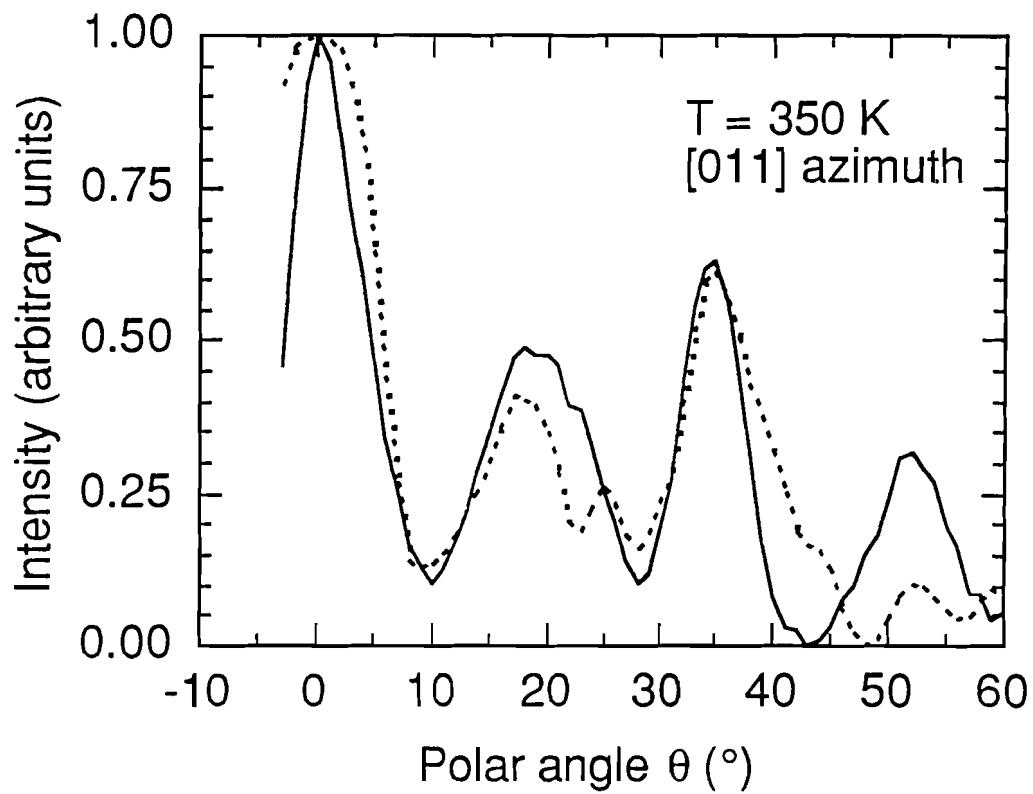


Figure 14: An experimental polar scan compared to the polar scan predicted by the single-scattering cluster model, when surface relaxation and thermal expansion are included, for the [011] azimuth of Pb(100) at  $T = 350$  K. The scan is normalized to unity for the peak at  $0^\circ$ . Solid and dashed lines represent the experimental data and the model, respectively.

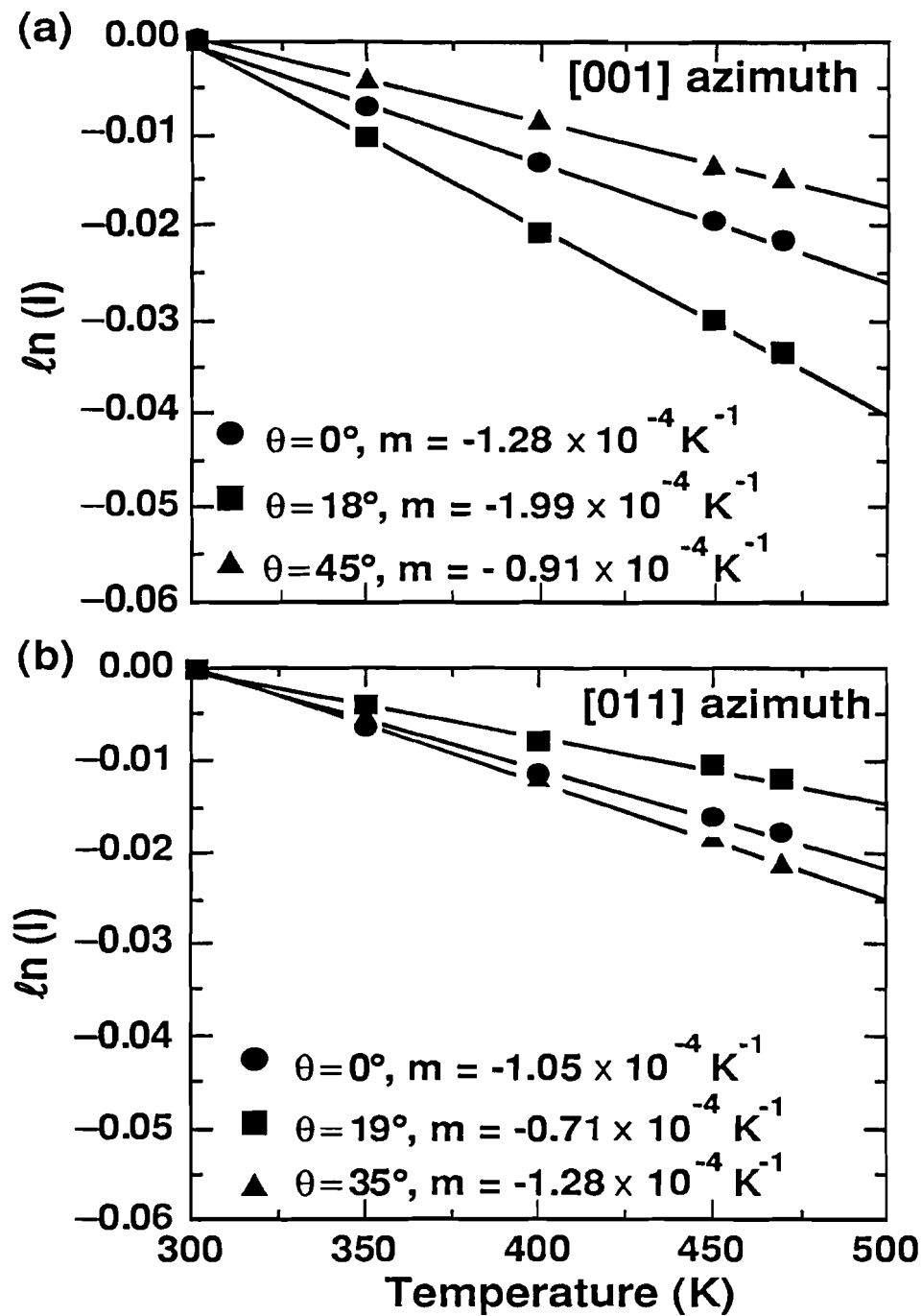


Figure 15: The logarithm of the forward-scattered intensity plotted as a function of temperature for the single-scattering cluster model including surface relaxation and thermal expansion for (a)  $\theta = 0^\circ$ ,  $18^\circ$ , and  $45^\circ$  along the [001] azimuth and (b)  $\theta = 0^\circ$ ,  $19^\circ$ , and  $35^\circ$  along the [011] azimuth.  $\theta = 72^\circ$  along [001], and  $\theta = 55^\circ$  along [011] are not included since the single-scattering cluster model does not predict the existence of these peaks much above the background level, as seen in Figs. 13 and 14.

The SSC method has previously been applied to the temperature-dependent behavior of forward-scattered peaks for azimuthal scans of Cu(001).<sup>8</sup> In this case, the effect of the surface was accounted for by assigning  $\theta_D(\text{surface})$  to the first atomic layer and  $\theta_D(\text{bulk})$  to the remaining layers. Multiple-scattering effects were partially accounted for by adjusting  $\beta$  and  $\lambda$ . However, the authors saw a significant difference between the experimental slopes and those predicted by the model, especially for forward-scattered peaks at  $\theta = 45^\circ$ , where multiple scattering is expected to play an important role. This work involved the calculation of an average scattering angle  $\bar{\theta}_j$  by inserting  $\theta_D(\text{bulk})$  and the slopes obtained from the model into Eq. (2.6). Using this  $\bar{\theta}_j$  with the experimental slopes allowed for the calculation of an effective  $\theta_D$ . A similar experiment on Ge(111) also showed a significant difference between the temperature dependence predicted by the SSC model and experiment.<sup>9</sup> Both of these studies attribute the intensity attenuation which is exponential with temperature to the Debye-Waller effect, although it is not clear that this is entirely accurate due to the large difference in slope between experimental observations and the corresponding models. As a check to the SSC model used here for Pb(100), the intensity attenuation of the forward-scattered peaks for Cu(001) is calculated and reasonable agreement with the results of Ref. 8 is obtained. Next, a similar calculation of  $\bar{\theta}_j$  is performed using the slopes from the model for Pb(100) and  $\theta_D(\text{bulk}) = 88 \text{ K}$  for  $\theta = 0^\circ, 18^\circ, \text{ and } 45^\circ$  [001], and  $\theta = 0^\circ, 18^\circ, \text{ and } 35^\circ$  along [011]. It is found that  $3^\circ \leq \bar{\theta}_j \leq 5^\circ$ , which leads to  $\theta_D(\text{effective}) = 24 \text{ K}$ . This is consistent with the Cu(001) and Ge(111) calculations that reported  $\frac{\theta_D(\text{bulk})}{\theta_D(\text{effective})} \approx 4$ . The experimental and calculated slopes for Pb(100), given in Figs. 12 and 15, are a little over one order of magnitude larger than those of Cu(001) and Ge(111) as a result of the significantly lower Debye temperature of Pb [ $\theta_D(\text{Pb}) = 88 \text{ K}$ , compared to  $\theta_D(\text{Cu}) = 343 \text{ K}$ ,  $\theta_D(\text{Ge}) =$

374 K]. A previous XPD experiment on Pb(110) shows experimental slopes of the same order of magnitude as is found in this experiment.<sup>2</sup>

Finally, this leads to an inquiry about multiple-scattering effects; but it is found that the attenuation of the Pb(100) forward-scattered peaks cannot be explained by even a slab-type spherical-wave multiple-scattering calculation performed by Tong *et al.*<sup>1</sup> In this model the sample was assumed to be 20 layers thick and to have a bulk-like lattice spacing and bulk  $\theta_D$ . Slight improvement is observed, but the experimental slopes still exceed the temperature dependence predicted by these calculations by at least an order of magnitude. Therefore, the discrepancy between the temperature dependence of the experiment and the SSC calculation is not completely explained by multiple-scattering effects, which implies that additional phenomena need to be investigated.

## 2.5 SURFACE DISORDERING OF Pb(100)

The temperature-dependent disordering of the Pb(110) surface has recently been under extensive study. A variety of surface sensitive techniques have been used to study this phenomenon, such as ion shadowing and blocking,<sup>3-5</sup> LEED,<sup>23-26</sup> x-ray scattering,<sup>27</sup> and XPD<sup>2</sup>. Results are conclusive that Pb(110) experiences surface melting, and the temperatures for the various stages of surface disorder are well established. Contrary to the Pb(110) surface, Pb(111) is densely packed and resists surface disordering up to the bulk melting temperature. Its temperature dependence up to  $T_m$  can be explained almost entirely by the Debye-Waller effect.<sup>24</sup> The (100) surface of a face-centered-cubic crystal is more closely packed than (110), but less packed than (111). Theoretical analysis has shown that the propensity for surface disorder with temperature depends on packing and is highest for open surfaces.<sup>28</sup> Ion shadowing and blocking has been used to study the temperature-dependent disordering

of Pb(100); approximately 1–2 disordered layers have been found on Pb(100) at about 600 K. In this experiment, the rate of change of the disordered layer thickness did not diverge as  $T_m$  was approached; thus, it has been suggested that Pb(100) is “on the verge” of surface melting.<sup>4</sup> A more recent experiment also using the ion shadowing and blocking technique the same technique measured 1.3 disordered monolayers at approximately  $T = 597$  K.<sup>5</sup> Using LEED, a weak disordering transition has been observed on Pb(100) beginning at about 570 K, which is distinctly different that what has been observed on Pb(110).<sup>21</sup>

### 2.5.1 RESULTS AND DISCUSSION

The effect of a surface disordered layer on the forward-scattered photoelectron intensity is now discussed. The attenuation resulting from a disordered layer of thickness  $\ell(T)$  can be expressed as<sup>2,6</sup>

$$I_{\text{corr}}(T) = I_0(T) \exp\left(\frac{-\ell(T)}{\lambda_{\text{eff}} \cos\theta}\right), \quad (2.8)$$

where  $I_0(T)$  is the photoelectron intensity at temperature  $T$  in the absence of a disordered layer.  $I_0(T)$  is determined by calculating the extension of the linear fit to  $\ln[I(T)]$  versus  $T$  in Figs. 8 and 9 to the higher temperature region. Hereafter  $I_0(T)$  is more descriptively called  $I_{\text{DW}}(T)$  because of the similarity between this functional form and that of the Debye-Waller effect. However, the degree of intensity attenuation greatly exceeds what is predicted for XPD using the SSC model including the Debye-Waller factor discussed in detail in Section 2.4. It has been previously shown both experimentally and theoretically that the disordered layer grows as a function of temperature according to the following relation under the conditions described below.

$$\ell(T) \propto \ln \left[ \frac{(T_m - T_0)}{(T_m - T)} \right], \quad (2.9)$$

where  $T_0$  is the characteristic temperature for the onset of surface disorder.<sup>2-4,29</sup> This behavior is expected for a system governed by short-range atomic interactions; such is the case for metals for sufficiently thin disordered layers.<sup>4,30</sup> If the disordered-layer thickness exceeds the range of these interactions, long-range forces become important and the disorder grows as a power law.<sup>4</sup> Given the exponential attenuation described in Eq. (2.8), and combining it with Eq. (2.9), the normalized intensity,  $I_{\text{corr}}(\theta, \phi, T)/I_{\text{DW}}(\theta, \phi, T)$ , is expected to have the following form<sup>2,24</sup>:

$$\frac{I_{\text{corr}}(\theta, \phi, T)}{I_{\text{DW}}(\theta, \phi, T)} = \left[ \frac{(T_m - T)}{(T_m - T_0)} \right]^r, \quad (2.10)$$

where  $r$  is a constant proportional to  $\frac{1}{\lambda_{\text{eff}} \cos \theta}$ .

The exponential attenuation in the experimental data is accounted for by dividing  $I_{\text{corr}}(\theta, \phi, T)$  by  $I_{\text{DW}}(\theta, \phi, T)$ . In Fig. 16,  $\ln[I_{\text{corr}}(\theta, \phi, T)/I_{\text{DW}}(\theta, \phi, T)]$  is plotted versus  $\ln(T_m - T)$ . The horizontal region where  $\ln[I_{\text{corr}}(\theta, \phi, T)/I_{\text{DW}}(\theta, \phi, T)] = 0$  corresponds to the region where the intensity attenuation is exponential with  $T$ , and the linear region for high temperatures indicates logarithmic growth of the disordered layer. The intermediate temperature region shows a slow intensity attenuation in excess of that corresponding to intensity attenuation that is exponential with temperature. This is attributed to partial disordering of the first atomic layer and/or anharmonic effects. The steep linear region at higher temperatures is interpreted as the spread of disorder to

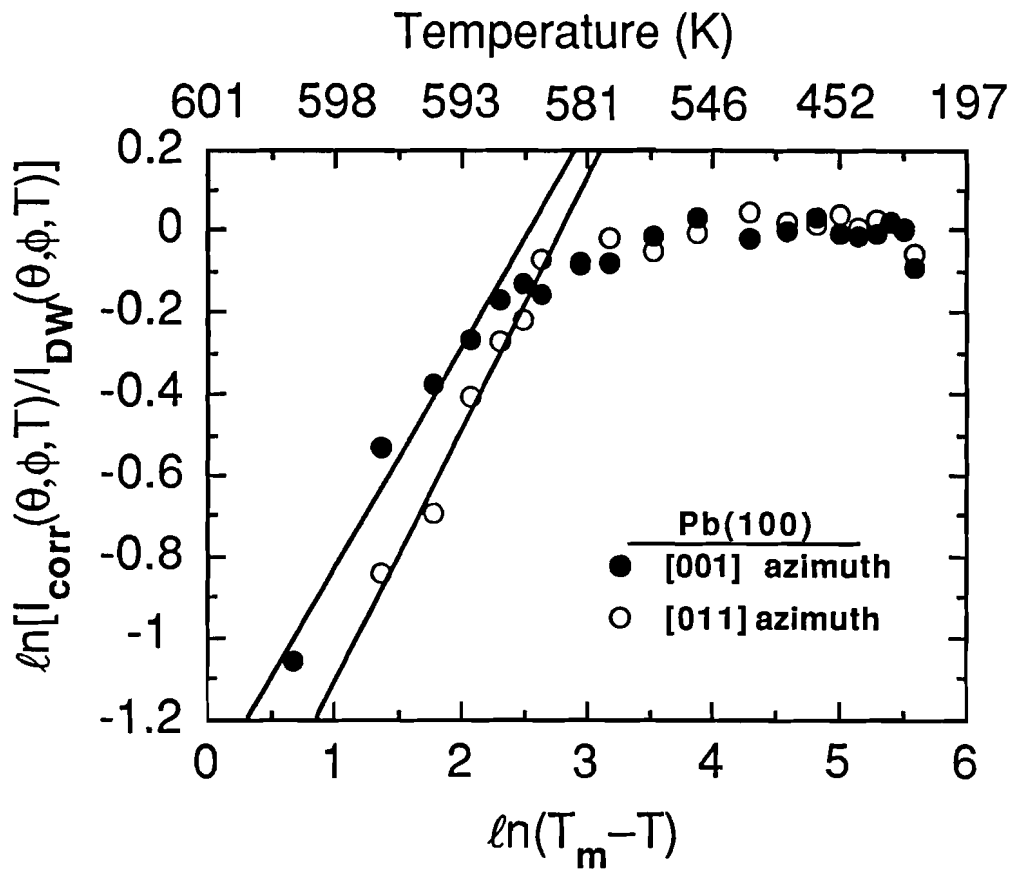


Figure 16: The logarithm of the corrected forward-scattered intensity normalized to the Debye-Waller fit,  $\ln[I_{\text{corr}}(\theta, \phi, T)/I_{\text{DW}}(\theta, \phi, T)]$  versus  $\ln(T_m - T)$ . The line-fit for  $T > 585 \pm 5$  K indicates that the disordered layer experiences logarithmic growth. Some anisotropy is seen; the [011] azimuth decays faster with temperature.

deeper atomic layers. If this line-fit is extrapolated to the temperature axis, it is found that  $T_0 = 585 \pm 5$  K for the [001] and [011] azimuths.

Slight anisotropy is observed; [011] experiences a more rapid decrease in intensity above  $T_0$ . Consideration of the solid-liquid interface provides an explanation for the observed anisotropy.<sup>23</sup> The interfacial free energy is lowest in the direction in which the atomic spacing of the solid is closest to the atomic spacing of the liquid. For Pb(100) this occurs along the [011] azimuth. This is consistent with Pb(110) where the  $[1\bar{1}0]$  azimuth disorders faster than [001].<sup>2,23,24,26,31</sup>

Using LEED, Prince *et al.*<sup>23</sup> have found  $T_0 = 543 \pm 3$  K for the [001] and  $[1\bar{1}0]$  azimuths of Pb(110). In their experiment, the intensity disappeared into the background above approximately 575 K for  $[1\bar{1}0]$ , and approached the background for [001]. In an XPD experiment on Pb(110), Breuer and co-workers<sup>2</sup> have observed logarithmic growth of the disordered layer for a temperature region close to  $T_m$ . For a lower temperature region they have reported the possible existence of another logarithmic growth law. They have concluded that  $T_0 = 530 \pm 5$  K, and that the higher temperature logarithmic growth law dominated above 575 K. Temperatures for the onset of surface disorder and the onset of complete surface melting were found by Frenken *et al.*<sup>3</sup> to be about 545 K and 580 K, respectively, with ion shadowing and blocking.

Contrary to the case of the Pb(110) surface, no evidence is found for a second logarithmic growth law for Pb(100). It is possible that such a growth law does not exist for Pb(100). This would indicate that Pb(100) experiences what is referred to as incomplete surface melting; that is, the rate of change of the thickness of the disordered layer does not diverge as  $T_m$  is approached. This is in contrast to complete surface melting where the disordered layer behaves increasingly like the bulk liquid and its

thickness diverges as the temperature nears  $T_m$ .<sup>31</sup> Another possibility is that a second growth law exists for Pb(100) at temperatures closer to  $T_m$  than is considered in these experiments. Ion shadowing and blocking experiments by van Pinxteren and Frenken performed after the time of this experiment and publication of these results show evidence that the surface melting of Pb(100) is indeed incomplete and no second logarithmic growth law is observed.<sup>5</sup>

Next, the temperature dependence of the number of disordered layers for Pb(100) is considered. To do this, the temperature-dependent intensity attenuation of Pb(110)<sup>2</sup> forward-scattered peaks, normalized in the same manner used in this experiment, is related to the number of disordered layers on the surface determined by Pluis *et al.*<sup>4</sup> using ion shadowing and blocking. These data are compared to the data reported here in Fig. 17. A deviation from behavior which is exponential with temperature is seen for Pb(110) around 500 K, and around 550 K for Pb(100). Two disordered layers have been found through analysis of the  $[1\bar{1}0]$  azimuth, on Pb(110) at 550 K, 4 disordered layers at 587 K, and 8 disordered layers at 599.3 K.<sup>2,4</sup> Next, in a comparison of the intensity attenuation of the [001] azimuth of Pb(100) with the above results, the disordered layer thickness for the [001] azimuth of Pb(100) is estimated to be 2 layers at about 590 K, and 4–5 layers at about 599 K. This prediction overestimates the previous results by Pluis *et al.* where about 1–2 disordered layers were visible around 599–600 K for Pb(100)<sup>4</sup> and the later results of van Pinxteren and Frenken<sup>5</sup> which show a maximum disordered layer thickness of 1.3 monolayers for  $T \geq T_m - 3$  K. The investigation of some of the possible reasons for this discrepancy are discussed.

It is important here to note that ion shadowing and blocking techniques provide a more accurate measurement of the thickness of the disordered layer than does XPD.

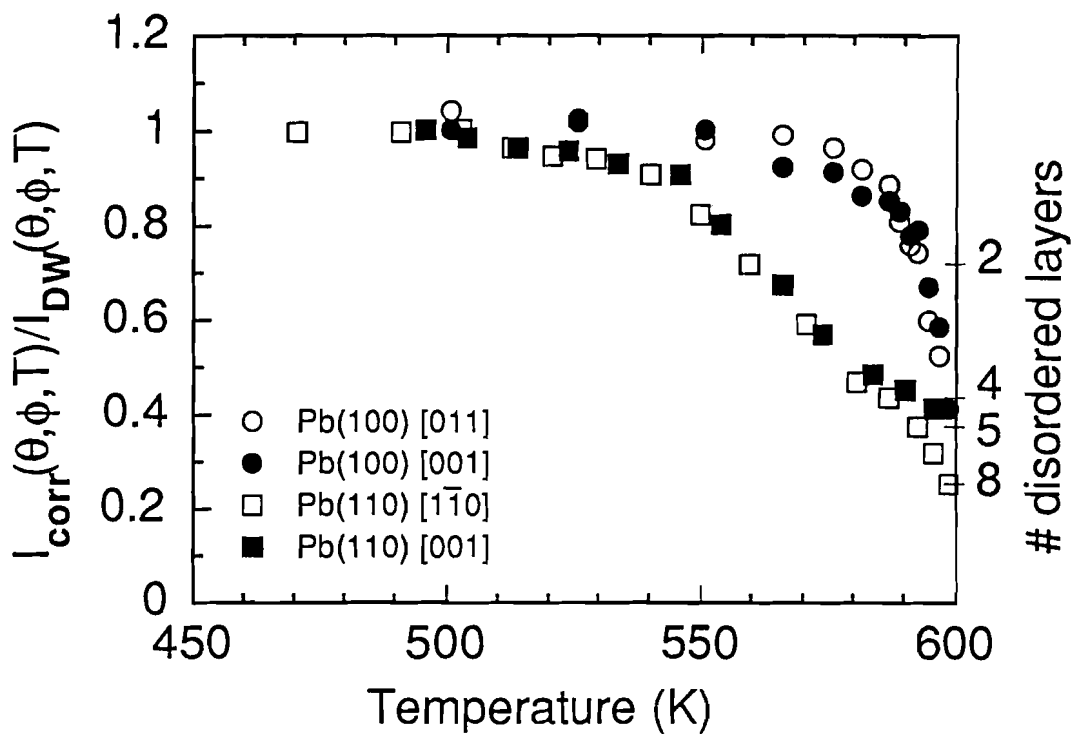


Figure 17: The corrected forward-scattered intensity,  $I_{\text{corr}}(\theta, \phi, T)$ , normalized to the Debye-Waller fit,  $I_{\text{DW}}(\theta, \phi, T)$ , plotted versus temperature for the [001] and [011] azimuths of Pb(100) for  $\theta = 0^\circ$  and compared to normalized intensities for the [001] and [1 $\bar{1}$ 0] azimuths of Pb(110) from Ref. 2. The number of disordered layers on Pb(110) as a function of temperature from Refs. 2 and 4 are compared to  $I_{\text{corr}}(\theta, \phi, T) / I_{\text{DW}}(\theta, \phi, T)$  as one method of predicting the number of disordered layers on Pb(100). Other methods are discussed in the text.

The XPD methods incorporated here, and elsewhere, are only approximate in determining the disordered layer thickness due to the difficulty in including multiple scattering into the models and the unavailability of accurate measurements of the effective mean-free path. Therefore, the thickness of the disordered layer is estimated by considering the predicted attenuation of the forward-scattered peaks by elastic and inelastic scattering as described in Eq. (2.8). For the [001] azimuth of Pb(100) at  $599 \pm 0.6$  K and  $\theta = 0^\circ$ , this leads to a prediction of 4.5 to 6.3 disordered layers for  $0.5 \lambda_{\text{in}} \leq \lambda_{\text{eff}} \leq 0.75 \lambda_{\text{in}}$ .<sup>6,8,15</sup> This is consistent with the above estimate but not with the ion shadowing and blocking results.

In an attempt to relate this data to the ion shadowing and blocking results on the Pb(100) surface near  $T_m$ , the ion shadowing and blocking and XPD experiments on the surface melting of Pb(110) are again considered. Through study of the ion yield as a function of temperature in the ion-scattering experiments, a quantitative measure of the number of disordered layers on the Pb(110) surface was obtained.<sup>4</sup> The XPD data for Pb(110) was found to predict the same number of disordered layers if  $\lambda_{\text{eff}} = 10 \text{ \AA}$  is assumed for photoelectrons with a kinetic energy of 1344.7 eV. It is known that the attenuation length ( $\lambda_{\text{eff}}$ ) in XPD can be significantly less than the inelastic mean-free path ( $\lambda_{\text{in}}$ ). In fact, for potassium  $\lambda_{\text{eff}}$  has been experimentally determined to be 4–5 times less than  $\lambda_{\text{in}}$  for 1344.7 eV photoelectrons.<sup>2</sup> Therefore, although  $0.5 \lambda_{\text{in}} \leq \lambda_{\text{eff}} \leq 0.75 \lambda_{\text{in}}$  is suggested in the literature, evidence exists that it may be reasonable to expect that the actual value of  $\lambda_{\text{eff}}$  in these XPD experiments is significantly less than this estimate. The recent experiments on the incomplete surface melting of Pb(100) showed logarithmic growth which saturated about 1–3 K below  $T_m$  for the [001] azimuth, estimating a disordered layer of 1.3 monolayers at the saturation temperature. No further growth of the disordered layer was observed up until  $T_m - 0.05$  K, the

highest temperature studied.<sup>5</sup> Using  $\lambda_{\text{eff}}$  for 1344.7 eV photoelectrons as suggested in Ref. 2 (even though 1117.0 eV photoelectrons are used in this experiment) in Eq. (2.8) an average disordered layer thickness of 2.1 monolayers is estimated at  $T = 597 \pm 0.6$  K for both azimuths, which is in much better agreement with the ion shadowing and blocking results. At  $T = 599 \pm 0.6$  K for [001], a disordered layer thickness of 3.2 monolayers is estimated. This is given in Fig. 18 where the disordered layer thickness is plotted versus  $\ln(T_m - T)$  to show that the disordered layer grows logarithmically. No evidence for leveling off of the thickness of the disordered layer is observed up to  $599 \pm 0.6$  K, however, this is probably due to the fact that temperatures closer to  $T_m$  were not explored in this experiment.  $\lambda_{\text{eff}} = 6.2 \text{ \AA}$  is necessary in this model to calculate a disordered layer thickness of 1.3 monolayers at  $T = 597$  K for Pb(100) from the XPD data. The fact that the forward-scattered peak at  $72^\circ$  for the [001] azimuth of Pb(100) nearly disappears at 599 K, although not completely suggests that slight order must still exist in the first 3 monolayers at 599 K (3 monolayers is the upper limit of the escape depth at  $72^\circ$ ) and that the predicted disordered layer thickness with  $0.5\lambda_{\text{in}} \leq \lambda_{\text{eff}} \leq 0.75\lambda_{\text{in}}$  is indeed an overestimate.

## 2.6 CONCLUSIONS

In this Chapter, it is demonstrated that the SSC model, including the Debye-Waller factor, shows reasonable agreement with the angular position of most forward-scattered peaks in experimental XPD polar scans on Pb(100) but significantly under-predicts the temperature dependence of the forward-scattered peaks. This model also includes reductions in the mean-free path of electrons and the atomic scattering factor which partially account for multiple-scattering effects. These observations support previous comparisons between experiment and the SSC model for azimuthal scans on

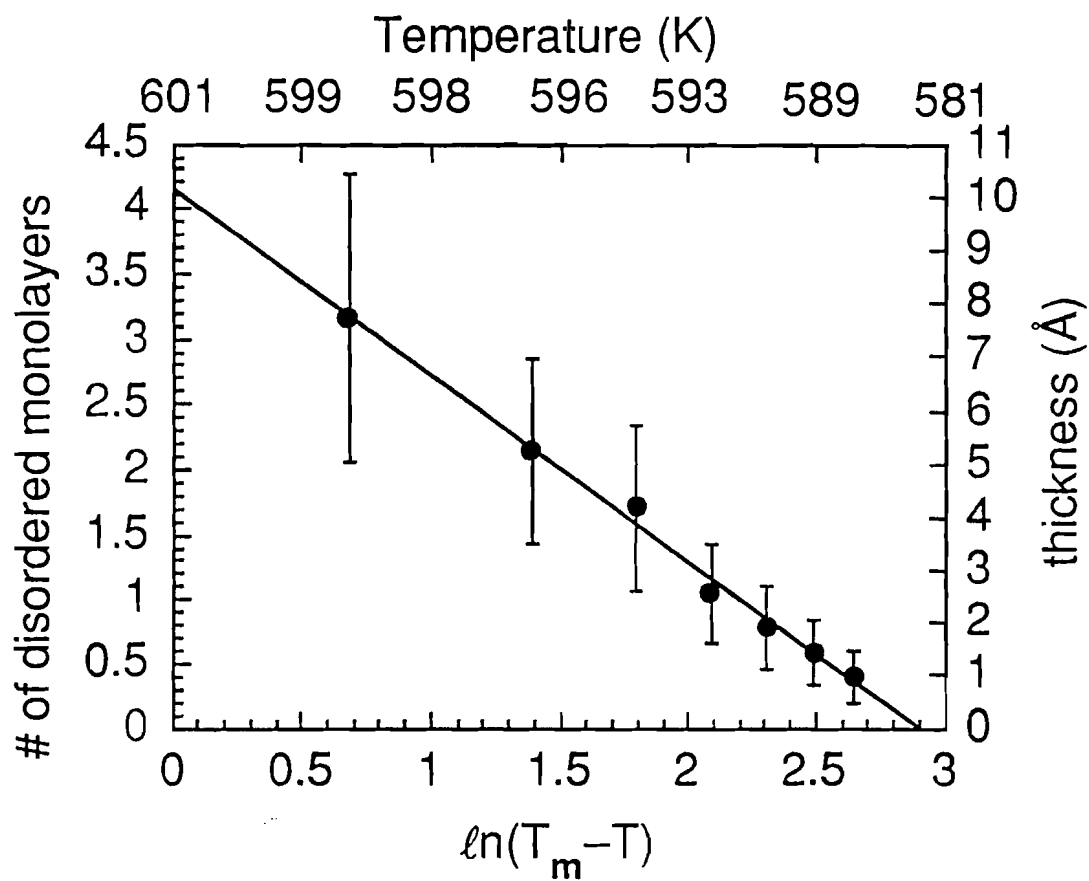


Figure 18: The number of disordered layers on Pb(100) determined using Eq. (2.8) with  $\lambda_{\text{eff}} = 10 \text{ \AA}$ . The data points represent the mean value of the number of disordered layers calculated from the eight forward-scattered peaks studied. The error bar designates  $\pm$  one standard deviation. The highest temperature point comprises data from the [001] azimuth only.

Cu(001) and Ge(111).<sup>8,9</sup> The results reported on in this Chapter show a much stronger temperature-dependent effect than is predicted by SSC calculations even when surface relaxation and thermal expansion are accounted for in the model. The experimental intensity attenuation exhibits the same functional dependence as the Debye-Waller effect; i.e., the attenuation is exponential with temperature. Larger lattice vibrations are observed on the surface relative to the bulk as an increase in the slope of  $\ln[I(\theta, \phi, T)]$  versus  $T$  for decreasing surface-layer thickness. This suggests that the enhanced lattice vibrations near the surface are important in XPD.

The increasing application of XPD to study temperature-dependent behavior of surface structure and the general inability of the SSC model to accurately predict the degree of experimentally observed forward-scattered peak attenuation suggest a need for further theoretical consideration. Although this study suggests that multiple-scattering effects are not completely responsible for the discrepancy, it would be interesting to see how the inclusion of surface relaxation, thermal expansion, and a layer-dependent Debye temperature would affect multiple-scattering calculations. Other thermal effects not discussed here, such as thermally produced surface defects (for example, vacancies), may also play a role. Further theoretical investigations are needed so that XPD may be used as a quantitative technique for the study of temperature-dependent surface behavior.

For higher temperatures, the [001] and [011] azimuths of Pb(100) exhibit incomplete surface melting below the bulk melting temperature. Intensity attenuation is no longer exponential with  $T$  above  $550 \pm 11$  K. The characteristic temperature for the onset of surface disorder,  $T_0$ , is  $585 \pm 5$  K for both the [001] and [011] azimuths. Slight anisotropy is exhibited; [011] has a more rapid intensity attenuation for temperatures above  $T_0$ . Approximate methods for calculating the thickness of the

disordered layer on Pb(100) suggest that the thickness is 2.1 monolayers at  $T = 597$  K. This is in reasonable agreement with ion shadowing and blocking experiments which measure a disordered layer thickness of 1.3 monolayers at approximately the same temperature.<sup>5</sup>

## 2.7 REFERENCES

1. S. Y. Tong, private communication.
2. U. Breuer, O. Knauff, and H. P. Bonzel, *Phys. Rev. B* **41**, 10848 (1990); U. Breuer, O. Knauff, and H. P. Bonzel, *J. Vac. Sci. Technol. A* **8**, 2489 (1990).
3. J. W. M. Frenken and J. F. van der Veen, *Phys. Rev. Lett.* **54**, 134 (1985); J. W. M. Frenken, Peter M. J. Maree, and J. Frisco van der Veen, *Phys. Rev. B* **34**, 7506 (1986).
4. B. Pluis, A. W. Denier van der Gon, J. W. M. Frenken, and J. F. van der Veen, *Phys. Rev. Lett.* **59**, 2678 (1987); B. Pluis, T. N. Taylor, D. Frenkel, and J. F. van der Veen, *Phys. Rev. B* **40**, 1353 (1989); B. Pluis, A. W. Denier van der Gon, and J. F. van der Veen, *Surf. Sci.* **239**, 265 (1990); B. Pluis, D. Frenkel, and J. F. van der Veen, *Surf. Sci.* **239**, 282 (1990).
5. H. M. van Pinxteren and J. W. M. Frenken, *Surf. Sci.* **275**, 383 (1992).
6. C. S. Fadley in *Synchrotron Radiation Research: Advances in Surface and Interface Science* edited by R. Z. Bachrach (Plenum Press, NY, 1992) p. 421–512; C. S. Fadley, *Progress in Surface Science* **16**, 275 (1984).
7. S. A. Chambers, *Adv. Physics* **40**, 357 (1991).
8. R. Trehan and C. S. Fadley, *Phys. Rev. B* **34**, 6784 (1986).
9. T. T. Tran, S. Thevuthasan, Y. J. Kim, D. J. Friedman, A. P. Kaduwela, G. S. Herman, and C. S. Fadley, *Surf. Sci.* **281**, 270 (1993); T. T. Tran, S. Thevuthasan, Y. J. Kim, G. S. Herman, D. J. Friedman, and C. S. Fadley, *Phys. Rev. B* **45**, 12 106 (1992).
10. W. F. Egelhoff, Jr., *Phys. Rev. Lett.* **59**, 559 (1987); W. F. Egelhoff, Jr., *CRC Crit. Rev. Solid State & Mater. Sci.* **16**, 213 (1990).
11. M. P. Seah and W. A. Dench, *Surf. Sci. Interface Anal.* **1**, 2 (1979).
12. P. Cadman and G. M. Gossedge, *J. Electron Spectrosc. & Relat. Phenom.* **18**, 161 (1980).
13. D. Chadwick, A. B. Christie, and M. A. Karolewski, *Surf. & Interface Anal.* **11**, 144 (1988).
14. S. Y. Tong, H. C. Poon, and D. R. Snider, *Phys. Rev. B* **32**, 2096 (1985).
15. H. P. Bonzel, U. Breuer, and O. Knauff, *Surf. Sci.* **237**, L398 (1990).
16. J. J. Barton, S. W. Robey, and D. A. Shirley, *Phys. Rev. B* **34**, 778 (1986).

17. M. Fink and J. Ingram, *At. Dat.* **4**, 129 (1972).
18. R. F. Lin, Y. S. Li, F. Jona, and P. M. Marcus, *Phys. Rev. B* **42**, 1150 (1990).
19. Y. S. Lin, J. Quinn, F. Jona, and P. M. Marcus, *Phys. Rev. B* **40**, 8239 (1989).
20. J. W. M. Frenken, F. Huussen, and J. F. van der Veen, *Phys. Rev. Lett.* **58**, 401 (1987).
21. H.-N. Yang, K. Fang, G.-C. Wang, and T.-M. Lu, *Phys. Rev. B* **44**, 1306 (1991).
22. Y. Cao and E. Conrad, *Phys. Rev. Lett* **65**, 2808 (1990).
23. K. C. Prince, U. Breuer, and H. P. Bonzel, *Phys. Rev. Lett.* **60**, 1146 (1988).
24. U. Breuer, H. P. Bonzel, K. C. Prince, and R. Lipowsky, *Surf. Sci.* **223**, 258 (1989).
25. H. -N. Yang, T. -M. Lu, and G. -C. Wang, *Phys. Rev. Lett.* **63**, 1621 (1989).
26. A. Pavlovska, H. Steffen, and E. Bauer, *Surf. Sci.* **234**, 143 (1990).
27. P. H. Fuoss, L. J. Norton, and S. Brennan, *Phys. Rev. Lett.* **60**, 2046 (1988).
28. A. Trayanov and E. Tosatti, *Phys. Rev. B* **38**, 6961 (1988).
29. R. Lipowsky, *Ferroelectrics* **73**, 69 (1987).
30. J. F. van der Veen, B. Pluis, and A. W. Denier van der Gon, *Chemistry and Physics of Solid Surfaces VII*, Eds. R. Vanselow and R. Howe (Springer-Verlag, Berlin 1988), pp. 455–490.
31. R. Lipowsky, U. Breuer, K. C. Prince, and H. P. Bonzel, *Phys. Rev. Lett.* **62**, 913 (1989).

## CHAPTER 3

### SUPERHEATING OF Bi(0001)\*

#### 3.1 INTRODUCTION

Supercooling of liquids is often observed; however, superheating of metals has only been observed under special conditions. The difficulty in superheating is attributed to the presence of nucleation sites for melting, such as crystal defects and free surfaces. For many metal surfaces, the formation of a surface-disordered layer below the bulk melting temperature provides a barrier to superheating. The role of the surface in the melting process can be suppressed by working with nearly defect-free small crystallites with predominantly close-packed surfaces that are less susceptible to disorder. Small crystallites of exposed Pb(111) facets<sup>1,2</sup> (0.01–0.5  $\mu\text{m}$  in diameter) and Bi(0001) facets<sup>3,4</sup> (0.07–0.15  $\mu\text{m}$  in diameter) have been superheated by 2–3 K and 7–10 K, respectively. Superheating has also been observed in cases where the nucleation of the melt at the free surface is suppressed. Superheating of Ag by at least 7.5 K has been observed for 120- to 160- $\mu\text{m}$ -diameter spheres of Ag coated uniformly with an 11- $\mu\text{m}$  layer of Au.<sup>5</sup> In other experiments, superheating by  $\sim 2$  K was achieved by preferentially cooling the surface of Sn and Cu rods while internally heating the bulk.<sup>6,7</sup> Superheating by tens to hundreds of degrees has been reported for metals and noble gases implanted in substrates with higher melting temperatures.<sup>8,9</sup> More recently, superheating of the Pb(111) surface by  $\sim 120$  K above the bulk melting temperature of 601 K has been observed using  $\sim 200$ -ps time-resolved reflection high-

---

\* contributing publication:

E. A. Murphy, H. E. Elsayed-Ali, and J. W. Herman, to be published in Phys. Rev. B **48** (1993).

energy electron diffraction (RHEED), the same technique that will be discussed here. In this case, melting of the free surface is bypassed by rapid heating and cooling of the surface with a pulsed laser.<sup>10</sup> A similar time-resolved study on Pb(110) showed that surface melting could not be bypassed with laser heating at the heating and cooling rates used in the experiment.<sup>11</sup> Because of the open rhombohedral (sometimes called pseudo-cubic) crystal structure of Bi, liquid Bi is more dense than the solid, and it has been suggested that such unusual structural differences between a crystal and its melt may provide a barrier to rapid melting.<sup>12</sup>

Bi has some very distinct physical properties when compared to Pb, such as the change in the volume, thermal conductivity, and electrical conductivity upon melting.<sup>13</sup> In fact, the only significant similarity between Bi(0001)\* and Pb(111) relevant to these studies is that both are close-packed surfaces which do not experience surface melting. Even the nature of atomic bonding for Bi and Pb is quite different, and the crystal structure of Bi is significantly more open than that of Pb. Bi is a semimetal, in contrast to Pb which is a very good conductor. The thermal and electrical conductivities of Bi are about one order of magnitude less than they are for Pb. As a result of its open rhombohedral crystal structure, Bi experiences a negative volume change and an increase in the thermal and electrical conductivities upon melting, in contrast to what is experienced by Pb and the majority of metals. These properties make liquid Bi a better metal than is the solid. This structure is also responsible for anisotropy in the atomic bonding and other material parameters of crystalline Bi. The rhombohedral structure of Bi is given in Fig. 19 with the anisotropic bonding indicated by solid and dashed lines,

---

\* The (0001) surface is similar to a cubic (111) structure. Hexagonal notation typically uses four indices. The first three indices are coefficients for co-planar lattice vectors which generate the hexagonal structure. The fourth index specified is the coefficient for a lattice vector perpendicular to the plane containing the other three.

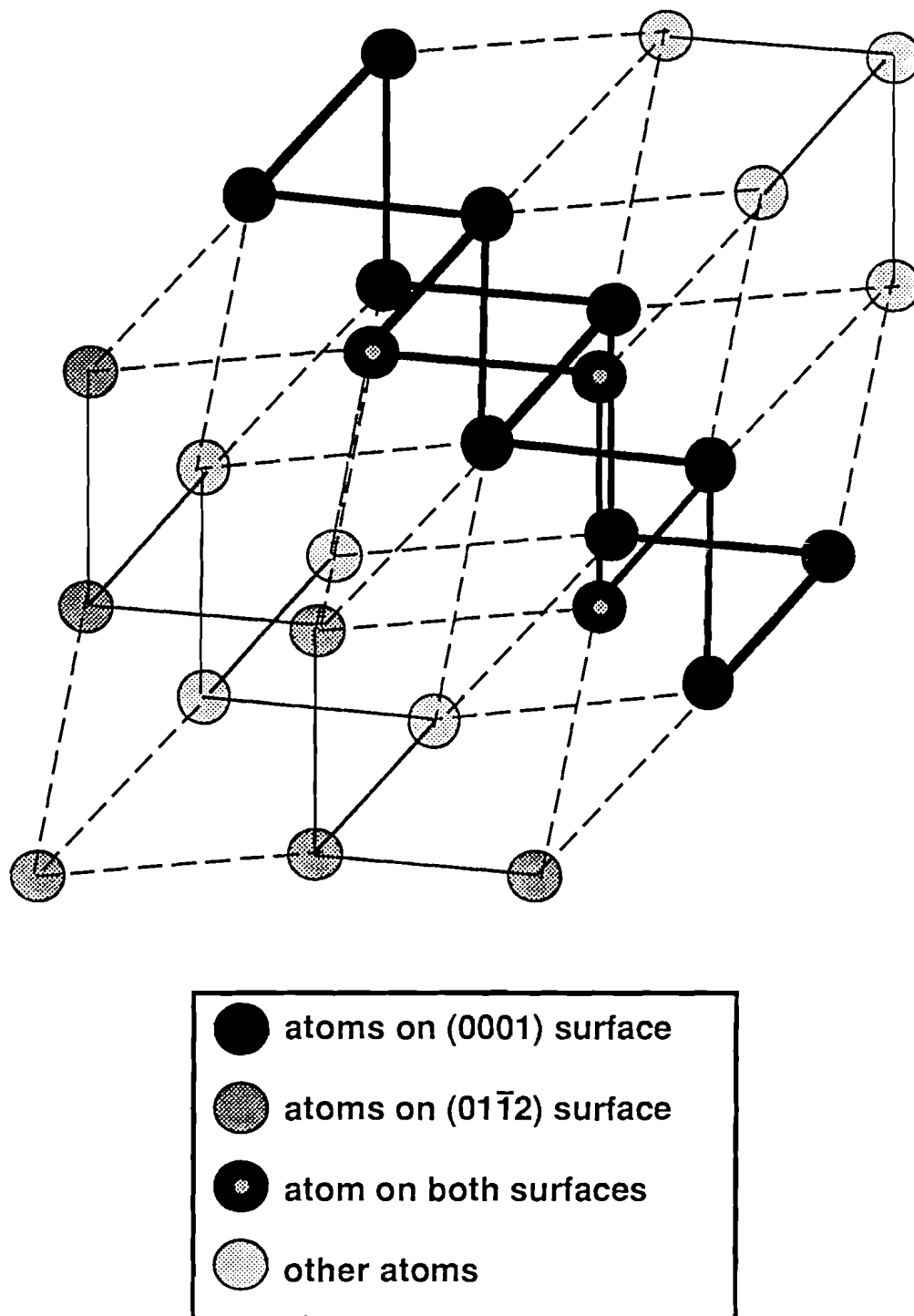


Figure 19: The rhombohedral structure of Bi. Solid lines and dashed lines represent nearest-neighbor bonds (covalent) and next-nearest-neighbor bonds (metallic), respectively. Bold solid lines connect atoms on the (0001) surface.

respectively. Bi has a two-point basis with a lattice constant of 4.75 Å. The angle between the primitive lattice vectors is  $57^{\circ}14'$ .<sup>14</sup> The real lattice of the Bi(0001) surface is given in Fig. 20. The observation of superheating of both the Bi(0001) and the Pb(111)<sup>10</sup> surfaces demonstrates that superheating is not strongly dependent on these properties, and is fundamentally a general phenomenon that is more dependent on properties such as the packing of surface atoms. Table 1 gives a comparison of some of the structural and thermal properties of Bi and Pb.

Table 1: Properties of Bi and Pb

ELEMENT →	Bi	Pb
<b>PROPERTY ↓</b>		
structure	rhombohedral	face-centered cubic
type of bonding	n. n.*: covalent next-n. n.: metallic	metallic
change in coordination number on melting?	increases	remains the same
volume change on melting	-3.35%	+3.5%
$K_s/K_l^{**}$	0.55	1.53
$\sigma_s/\sigma_l^{**}$	0.47	1.98

\*n. n. stands for nearest neighbor.

\*\* $K_s$ ,  $K_l$ ,  $\sigma_s$ ,  $\sigma_l$  are the thermal and electrical conductivities of the solid and the liquid phases, respectively. Reference: B. R. T. Frost, Prog. Met. Phys. 5, 96 (1954).

### 3.2 SUPERHEATING OF CRYSTALLITES IN THE ELECTRON MICROSCOPE

Superheating of Bi(0001)<sup>3</sup> and Pb(111)<sup>1,2</sup> crystallites have both been observed in the electron microscope. Both types of crystallites were found to experience a time

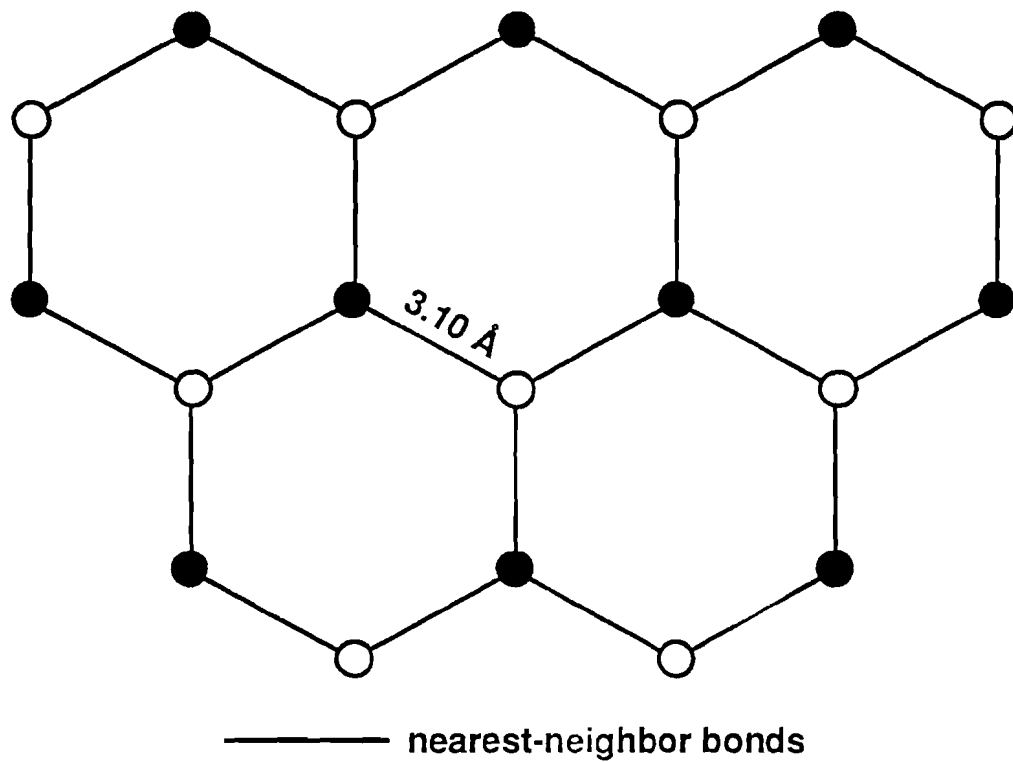


Figure 20: The Bi(0001) surface is similar to a (111) simple-cubic surface. Atoms designated by ● are slightly raised above those designated by ○ in the surface plane.

delay in melting which enabled the crystallites to be held at temperatures above the bulk melting temperature for a finite amount of time before melting. The presence of this time delay is evidence for the nucleation theory of melting.

In the Bi crystallite experiments<sup>3</sup>, Bi vapor was condensed onto carbon substrates at room temperature to form a uniform film of approximately 10 nm in thickness. The diffraction from this film showed many grains with (0001) faces. The film was heated to  $T \geq T_m - 50$  K which resulted in the formation of separated crystals. Heating further to  $T \geq T_m - 10$  K resulted in hexagonal crystallites and spherical liquid droplets. The hexagonal crystallites, made up primarily of (0001) facets, were called Type I platelets. Some of these platelets were melted, and then cooled. The resolidified crystallites formed hexagonal solid particles which showed a diffraction pattern corresponding to a randomly-oriented deposit. These were called Type II polyhedra. When the liquid droplets which formed below  $T_m$  were resolidified they formed hexagonal particles which exhibited different melting properties than the Type II polyhedra and thus were labeled as Type III polyhedra. All three of these Bi particles exhibited a time delay in melting, however, only Type I platelets remained solid above the bulk melting temperature. The time delay as discussed here corresponds to the time it takes melting to start, not to the actual time it took the crystallites to melt. In fact, once melting occurred, it was on a time scale much shorter than the resolution of these experiments. The particles were heated for various lengths of time and then cooled. After cooling the number of particles which had remained solid during the heating were counted for each type. The ratio of the number of particles remaining solid was found to decay exponentially with time held above  $T_m$ . A characteristic time of melting,  $\tau$ , was obtained as a function of temperature and it was shown that  $\ln(\tau)$  versus  $T$  is linear for all three types of crystallites. Only the Type I

platelets were observed to superheat on the time scales used in this experiment; the shortest time scale investigated was just under 1 minute.

These observations of superheating of and the time delay in melting for Bi crystallites are extended to the time scale of the Bi(0001) experiments that are the subject of this chapter. It is found that the exponential dependence of the characteristic time delay  $\tau$  on  $T$ , determined from the electron microscope experiments on Type I platelets, predicts close to the same amount of superheating that is observed using time-resolved RHEED. It is important to note here that this is a very rough comparison. Although lines are fit to the data in Ref. 3, there is a substantial amount of scatter, and the report does not describe the method of determining the best line fit. It is also found that, if the behavior observed in the crystallite experiments is valid on the time scales of the time-resolved RHEED experiments, then Type II and III polyhedra would also be predicted to superheat if fast enough heating rates were used. The extension of the line fit corresponding to Type I platelets to these time scales is shown in Fig. 21. It is found that the line fits predict a time delay of about 16 seconds, 48 seconds, and 16.2 minutes for  $T = T_m$  for the Types I, II, and III crystallites, respectively. The exact superheating time in the time-resolved Bi(0001) experiments reported on here is not obvious due to the transient behavior of the laser heating, however, it is known that it is larger than 200 ps, the pulse width of the laser, and less than tens of ns. In these time-resolved experiments on Bi(0001), the surface temperature can remain above  $T_m$  for several ns.

It is important to note that the extension of the behavior observed in the crystallite experiment to the time scales used here is only qualitative, although it may provide insight into the melting phenomenon. It is unknown how far the observations

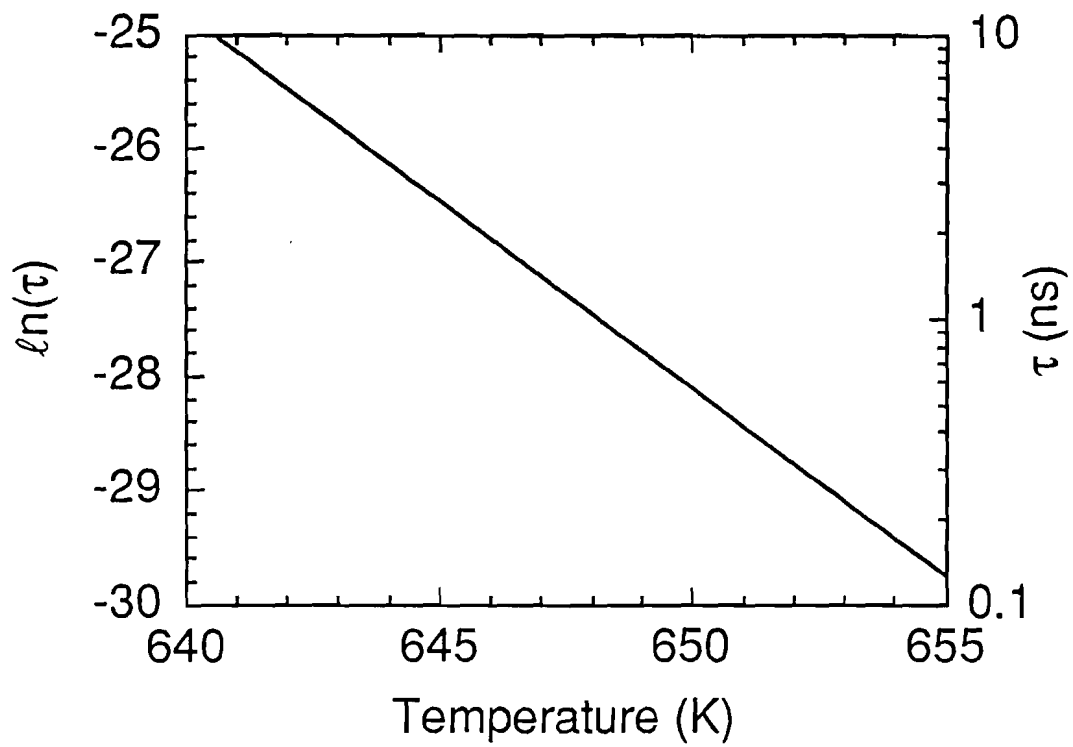


Figure 21: The characteristic time of melting versus bias temperature from Ref. 3 extended to the time scales used in time-resolved RHEED experiments on Bi(0001).

of the crystallite experiment can be extended, and it is expected that at some time delay this behavior should break down, i.e. that there is some maximum superheating temperature that is independent of time scale. Such a superheating temperature has been suggested.<sup>15</sup> It is predicted that every solid has a mechanical melting point which exceeds the thermodynamic melting temperature,  $T_m$ . The mechanical melting temperature results from an instability of the lattice under shear stress. In contrast to thermodynamic melting which is a heterogeneous process initiated at extended defects, mechanical melting occurs homogeneously throughout the crystal, in just a few lattice vibrations, independent of the number or nature of defects.<sup>15,16</sup>

One very interesting aspect of the Bi crystallite experiment is that a time delay in melting was observed for all of the types of crystallites, whether or not they superheated or melted below  $T_m$ .<sup>3</sup> A time delay in the melting of Pb crystallites bounded by (111) facets has been observed, however no time delay was observed for Pb crystallites with other exposed facets.<sup>1</sup> Other 200-ps time-resolved RHEED experiments on the (110), (100), and (111) surfaces of Pb found that only the (111) surface could be superheated, i.e. only the surface for which a time delay in melting was observed.<sup>10,11,17</sup> This opens the question of whether or not non-(0001) Bi surfaces could be superheated with time-resolved RHEED, and whether or not they would experience surface melting. The Bi crystallite experiment suggests that superheating of other Bi faces may be possible, but perhaps not to as high a temperature as for the (0001) facets. Bi(0001) and Bi(01 $\bar{1}$ 2) have both been reported to experience no surface melting, however, this same study also reported no surface melting for Pb(110).<sup>18</sup> Since these experiments, Pb(110) has been shown to exhibit significant surface melting, which leads one to question their interpretation of the data for other surfaces. Based on the argument that open surfaces are more likely to

experience surface melting than close-packed ones, the temperature-dependent behavior of the surface structure of Bi(01 $\bar{1}$ 2) [which is similar to a cubic (100) surface, see Fig. 22] was investigated. No evidence of surface melting was observed up to  $T_m - 30$  K in a preliminary x-ray photoelectron diffraction experiment. Time-resolved RHEED experiments on the Bi(01 $\bar{1}$ 2) surface, for example, would be very instrumental in determining the importance of a time delay, as well as testing the role of the degree of surface packing, in superheating.

### 3.3 EXPERIMENT

Here, a superheating study of Bi(0001) using time-resolved RHEED with ~200-ps time resolution is discussed. Bi was chosen for its relatively low melting temperature ( $T_m = 544$  K), low vapor pressure at the melting point ( $\sim 2 \times 10^{-10}$  Torr), and the fact that previous slow-heating experiments have demonstrated superheating of Bi crystallites. In addition, the close-packed Bi(0001) surface is chosen for these superheating experiments because, in general, open surfaces are more likely to exhibit surface melting, providing a nucleation site for bulk melting at  $T_m$ . Using time-resolved RHEED with ~200-ps resolution heating rates of  $\sim 10^{11}$  Ks $^{-1}$  can be achieved, approximately 13 orders of magnitude larger than that used in the Bi crystallite experiments. In fact, superheating of Bi(0001) by ~90 K is observed and is discussed in detail in the following sections.

Two Bi(0001) samples were used for these experiments. The single crystals were grown from Bi of 99.999% purity. The samples were cut to within  $\pm 1^\circ$  of the (0001) surface. The surface was then mechanically lapped to a 1- $\mu$ m finish and chemically etched in 20% HNO $_3$  followed by 10% HCl. The angle of incidence was approximately 1–2 $^\circ$ , corresponding to a probe depth of 1–3 Å. In both cases, the

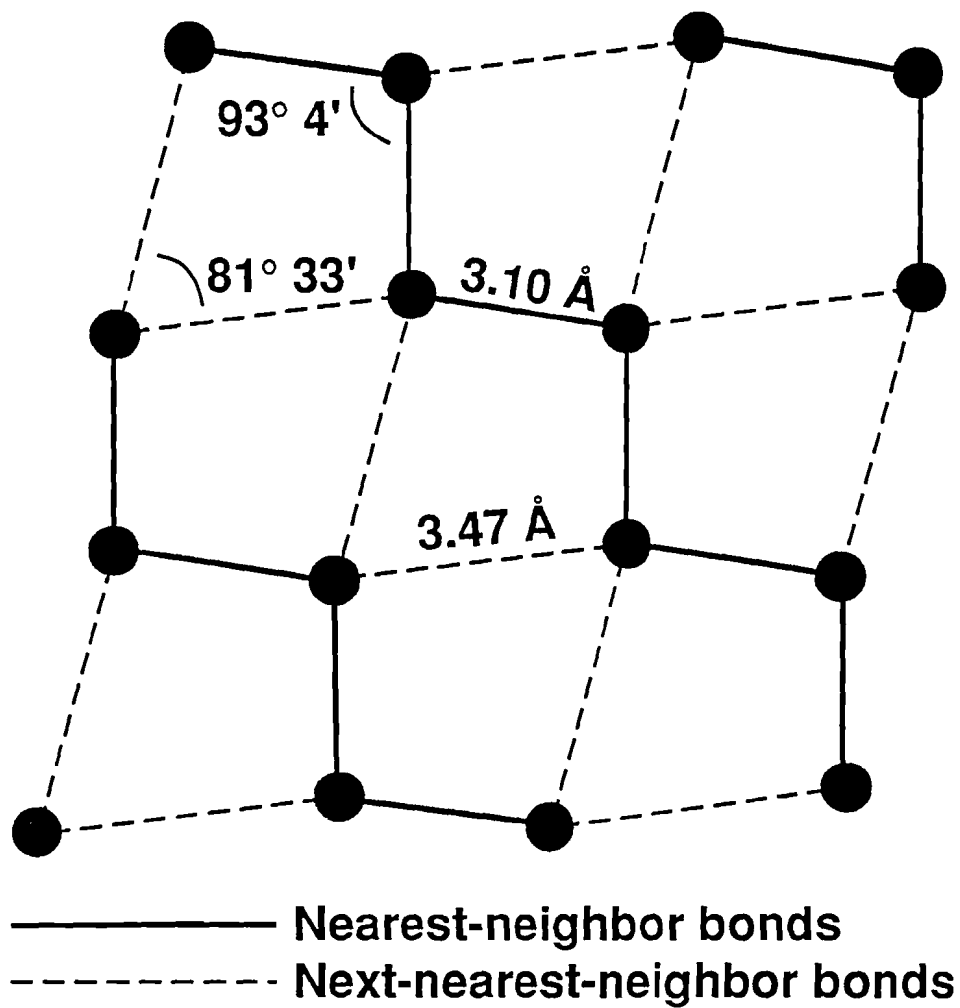


Figure 22: The Bi(011̄2) surface. Anisotropic bonding is labeled with solid lines (metallic bonds) and dashed lines (covalent bonds).

electron beam is incident along the  $[10\bar{1}0]$  direction. Base pressure in the ultrahigh vacuum system is in the low  $10^{-10}$  Torr range. Surface cleanliness is checked with Auger electron spectroscopy (AES). See Appendix A. Scans of clean and contaminated Bi(0001) are shown in Fig. 23. Before each experiment, the sample is cleaned with argon-ion bombardment and annealed to 523 K.

### 3.4 REFLECTION HIGH-ENERGY ELECTRON DIFFRACTION

RHEED is a surface-sensitive probe of long-range order ( $\sim 100$  Å or more) which provides information on the atomic structure of surfaces. A diffraction pattern gives a statistical average of the structure over the entire region probed. In RHEED, electrons are incident on the sample at a glancing angle as shown in Fig. 24. In these experiments, the diffraction pattern is amplified by an microchannel plate (MCP)/phosphor screen assembly and detected by a light sensitive device, such as photographic film, an array detector, a photomultiplier tube, or photodiode. The inelastic mean-free path of high-energy electrons is quite large, however, because of the glancing angle of incidence of electrons in RHEED, the incident electrons only probe a few atomic layers into the sample.

Diffraction results when the Laue condition

$$\begin{aligned} (\mathbf{k}' - \mathbf{k}) \cdot \mathbf{R} &= 2\pi m, \\ \text{where } \mathbf{R} &= n_1 \mathbf{a} + n_2 \mathbf{b} \end{aligned} \tag{3.1}$$

is satisfied.  $\mathbf{k}$  and  $\mathbf{k}'$  are the incident and scattered electron wavevectors.  $\mathbf{R}$  is the Bravais lattice vector where  $\mathbf{a}$  and  $\mathbf{b}$  are the primitive lattice vectors for the surface, and  $n_1$  and  $n_2$  are integers.<sup>19</sup>

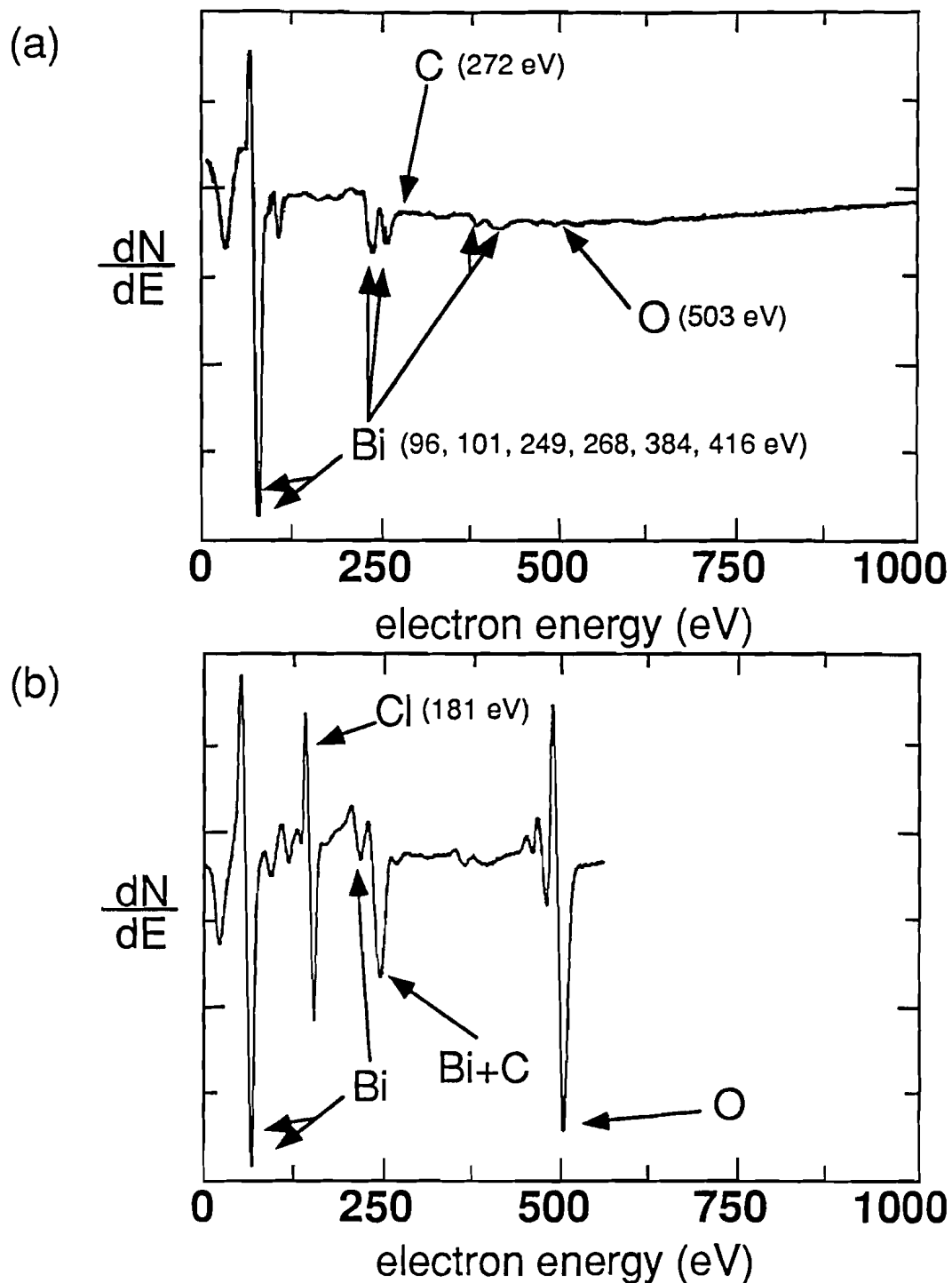


Figure 23: (a) AES confirms the cleanliness of the Bi(0001) surface. (b) A contaminated surface is shown for comparison. The Cl is a remnant of the chemical etching of the surface with HCl.  $N$  is the number of electrons counted by the energy analyzer. The primary beam energy is 3 keV. See Appendix A for a brief description of the technique.

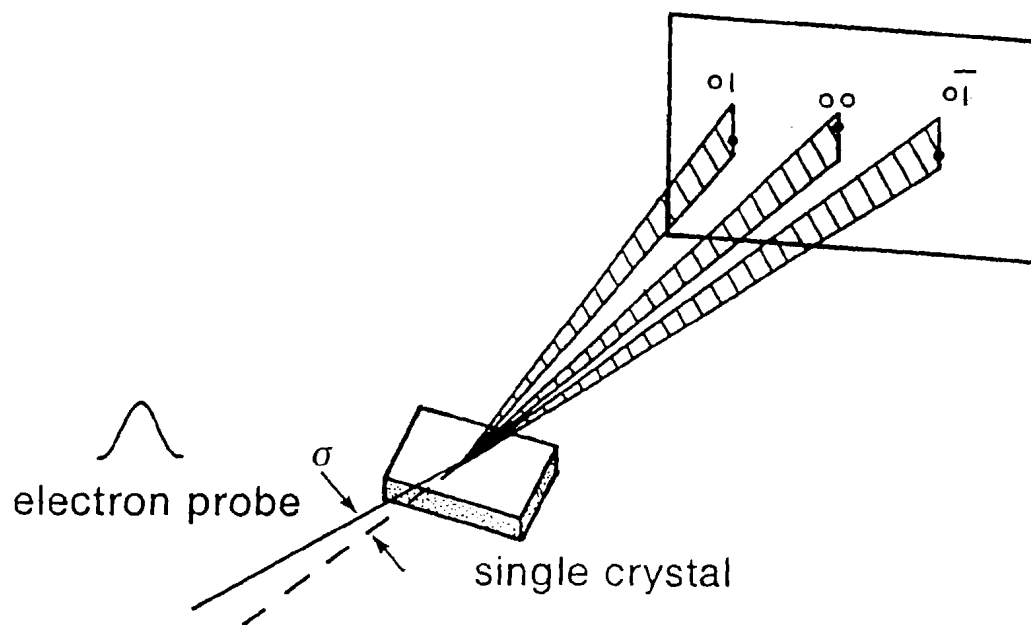


Figure. 24: High-energy electrons at glancing incidence generate the RHEED pattern.

The diffraction condition given in Eq. (3.1) can be visualized in the Ewald sphere representation shown in Fig. 25. The sphere itself gives conservation of energy and the superposition of the reciprocal lattice onto the Ewald sphere gives conservation of momentum. The diffraction is given by the intersection of the Ewald sphere with the reciprocal lattice.<sup>20</sup>

A diagram showing a typical RHEED pattern is given in Fig. 26. Thermal diffuse electrons, which result from electrons which experience multiple phonon collisions, account for the background signal. The amount of multiphonon scattering increases with temperature and is directly related to the thermal vibrations of the surface atoms, or equivalently, the surface Debye temperature. The shadow edge is due to the blocking of these electrons by the sample. Usually, a portion of the incident beam is either transmitted through the sample at its edge or never penetrates the sample resulting in the observation of the transmitted beam on the screen. For an electron beam exactly at glancing incidence, the RHEED pattern is positioned in a straight line along the shadow edge. As soon as the angle of incidence is increased from  $0^\circ$ , the pattern moves off the shadow edge and forms an arc. The angle of incidence can be determined from simple geometry if the distance from the shadow edge to the specular-beam center is measured on the screen, and the distance from the sample to the screen is known.

There are at least two common explanations for the observation of streaks (as opposed to spots) in RHEED. In one description, it is generally believed that under ideal experimental conditions a surface of high quality will generate a RHEED pattern consisting of spots, however, it is believed that the streaks frequently observed in RHEED can result from a high-quality surface and this is due to instrumental and sample effects. For example, the finite width and the divergence of the electron beam

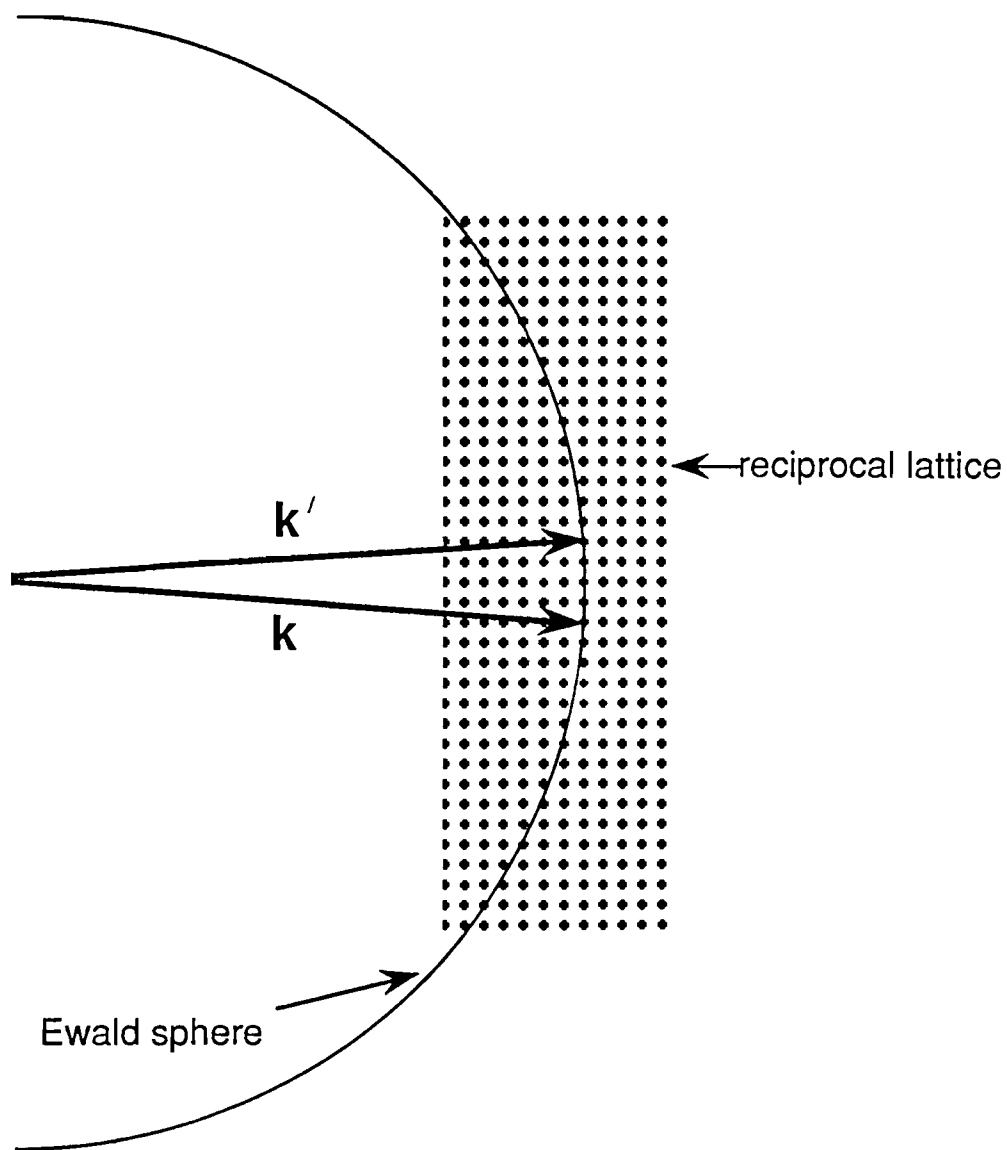


Figure 25: The Ewald sphere representation for RHEED. The scale corresponds to a lattice spacing of 3 Å and an electron energy of approximately 14 keV.

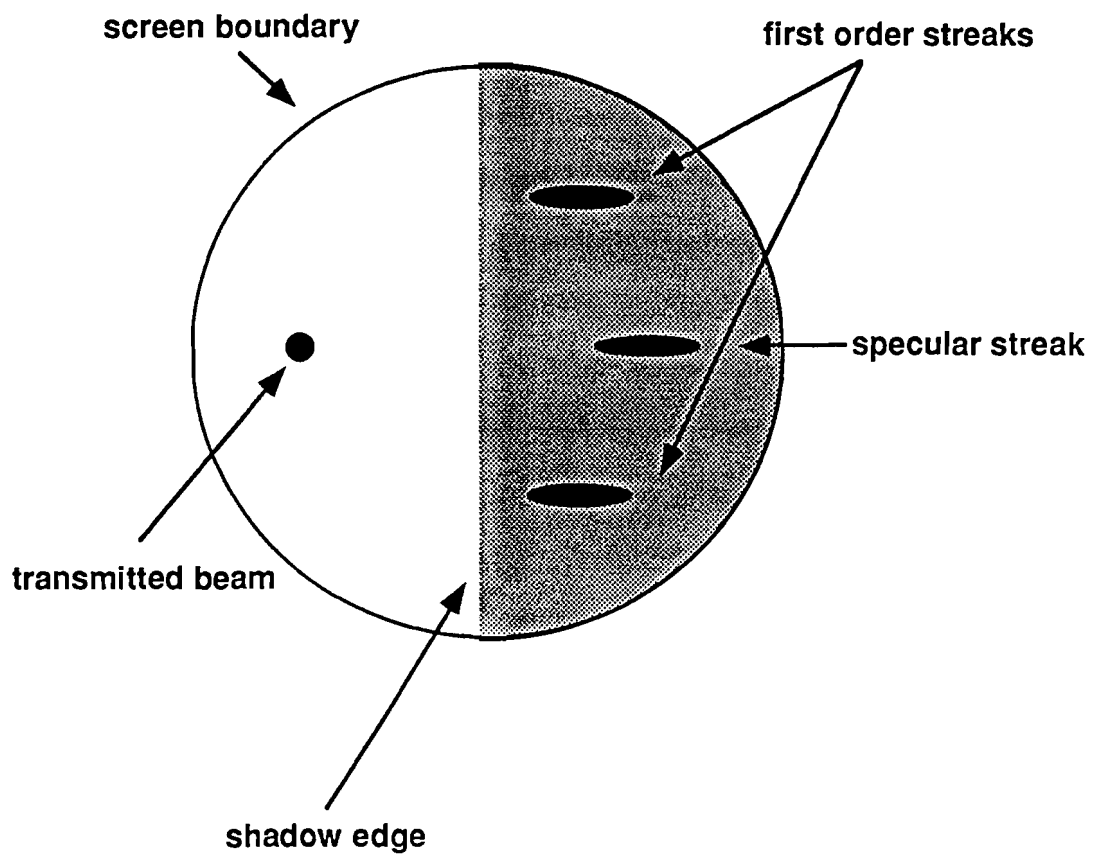


Figure 26: A typical RHEED pattern for non-zero angle of incidence.

result in smearing of the origin of k-space and hence the center of the Ewald sphere. A finite electron-energy window results in the Ewald sphere becoming a thin spherical shell, the thickness of which is governed by the spread in electron energy. In the other case, the streaks are thought to result from the glancing angle of incidence which effectively stretches out the reciprocal lattice points in the direction perpendicular to the surface into elongated spots or rods. In most experimental cases, the observation of streaks is probably a combination of both effects, and can result from high-quality surfaces.<sup>19</sup>

The RHEED patterns corresponding to a particular surface structure can be calculated from the real lattice and other easily obtained experimental parameters. The reciprocal lattice is given by

$$\begin{aligned} \mathbf{a}^* &= \frac{2\pi\mathbf{b} \times \hat{\mathbf{n}}}{A} \\ \mathbf{b}^* &= \frac{2\pi\hat{\mathbf{n}} \times \mathbf{a}}{A} \end{aligned} \quad (3.2)$$

$$\text{where } A = \mathbf{a} \cdot \mathbf{b} \times \hat{\mathbf{n}}.$$

These are the two-dimensional analogs of the standard equations for calculating the reciprocal lattice.  $\mathbf{a}$  and  $\mathbf{b}$  are the primitive lattice vectors which generate the surface structure,  $\mathbf{a}^*$  and  $\mathbf{b}^*$  are the corresponding reciprocal lattice vectors,  $\hat{\mathbf{n}}$  is a unit vector in the direction of the surface normal, and  $A$  is the area of the two-dimensional primitive cell. The anticipated spacing between RHEED streaks for the Bi(0001) surface is determined using similar triangles from

$$\frac{W}{L} = \frac{a^*}{(2\pi/\lambda)}, \quad (3.3)$$

where  $W$  is the streak spacing observed on the phosphor screen,  $L$  is the sample to screen distance in the UHV chamber,  $a^*$  is the reciprocal lattice spacing perpendicular to the direction of electron incidence, and  $2\pi/\lambda$  is the magnitude of the incident-electron  $k$ -vector. This is valid when  $\lambda$ , the wavelength of the electrons, is much smaller than the magnitude of the lattice constant.<sup>19</sup> This is generally the case for the electron energies used in RHEED. For example, in the experiments reported on here the electrons are accelerated through 15.0 kV which corresponds to  $\lambda = 0.09 \text{ \AA}$ . This is almost two orders of magnitude less than typical lattice constants. The electron wavelength is obtained from the relativistic expression

$$\lambda = \frac{h}{\left\{ 2m_0qV \left[ 1 + \frac{qV}{2m_0c^2} \right] \right\}^{1/2}}, \quad (3.4)$$

where  $h$  is Planck's constant,  $m_0$  is the electron rest mass,  $q$  is the electron charge,  $V$  is the accelerating voltage, and  $c$  is the speed of light.<sup>19</sup>

The surface structure of a sample can be determined or confirmed by observing the RHEED patterns obtained at different azimuthal angles and comparing the streak spacings for the different directions. The reciprocal lattice of Bi(0001), and RHEED patterns confirming its structure are shown in Fig. 27.

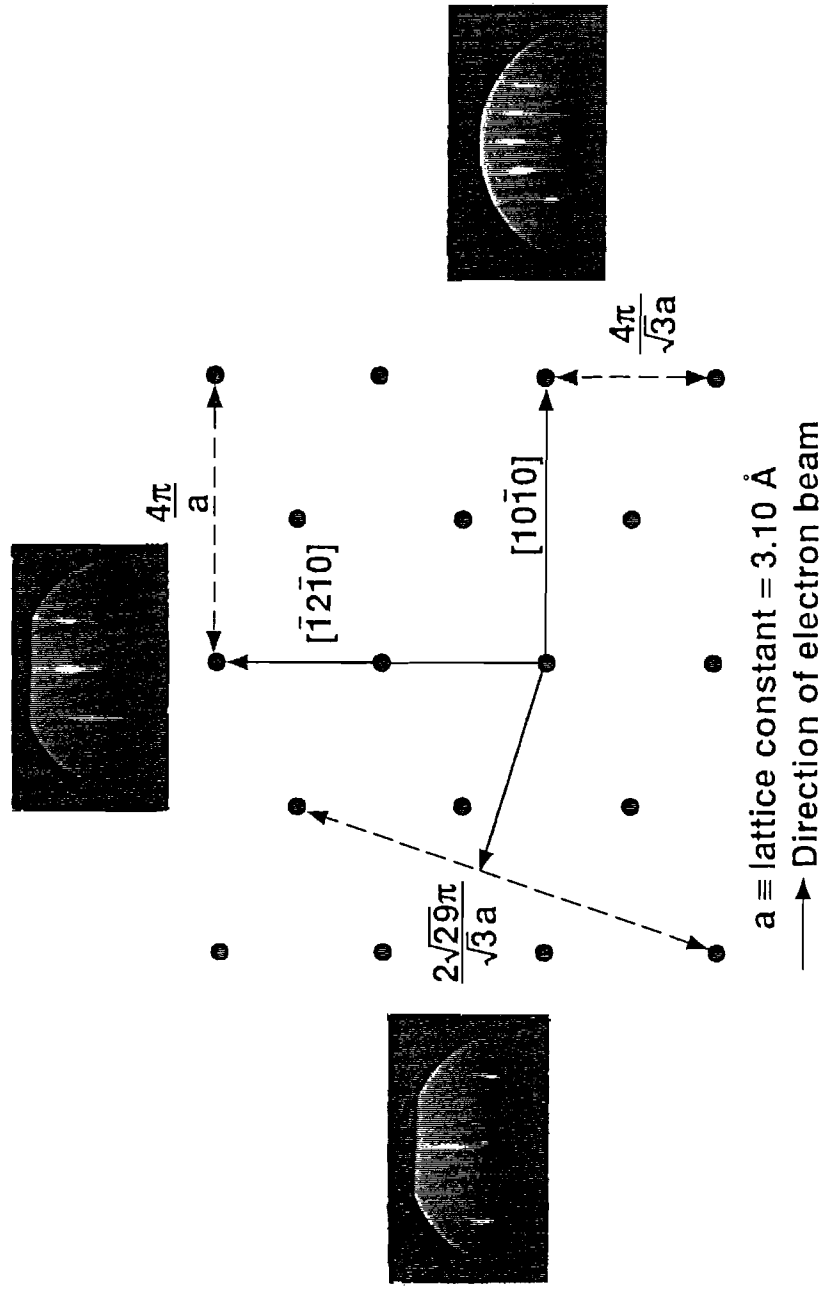


Figure 27: The reciprocal lattice of Bi(0001) is determined using RHEED by obtaining diffraction patterns in two or more azimuthal directions.

### 3.5 TIME-RESOLVED RHEED AND THE LASER SYSTEM

Time-resolved RHEED is a pump-probe technique in which the pump pulse rapidly heats the sample surface while a photoelectrically-generated electron pulse probes the surface structure at some time relative to the time of surface heating. The probing electron beam is incident on the surface at glancing incidence which facilitates the surface heating at near-normal incidence. In addition, RHEED has reduced space-charge effect limitations on the number of electrons per pulse due to the high electron energies, when compared to low-energy electron diffraction. This is extremely beneficial in observing the time-resolved diffraction pattern as the electrons are only probing the sample for  $\sim 200$  ps [the full width at half maximum (FWHM) of the laser pulse] at a 15 Hz repetition rate. In these experiments, the number of electrons incident on the sample per pulse is on the order of  $10^5$ .

The laser system used in this experiment consists of oscillator-driven Nd:yttrium aluminum garnet (YAG) regenerative amplifier. The Nd:YAG laser pulse is split into two beams and the fundamental wavelength ( $\lambda = 1.06 \mu\text{m}$ ) travels through a double-pass amplifier before being used to heat the surface. The spatial FWHM of the beam (1 cm for these experiments) is at least the diameter of the sample and has the purpose of uniformly heating the surface. The second portion of the beam is frequency quadrupled ( $\lambda = 0.266 \mu\text{m}$ ) and is incident on the cathode of a photoactivated electron gun, thus generating the pulsed electron beam. The electron pulses interact with the sample at glancing incidence to generate the time-resolved RHEED pattern. The electron energy is 15.0 keV and the temporal width of the electron pulse is comparable to that of the fundamental laser pulse. Only a small percentage of the laser pulse energy is frequency quadrupled so that most of the energy is available for surface heating.

Schematic diagrams of the laser system and the concept of time-resolved RHEED are given in Figs. 28 and 29, respectively. By optically delaying the probing electron pulse relative to the heating laser pulse, the time evolution of surface heating can be studied. The RHEED pattern is lens coupled from an MCP/phosphor-screen assembly to a linear-array detector. A RHEED streak is then monitored by a line scan perpendicular to the streak and through its peak intensity. A mechanical shutter is placed in the path of the heating laser beam allowing the accumulation of heated and unheated scans which are then stored in separate memories. See Fig. 30. An example of the behavior of the ratio of the heated to unheated intensities versus delay time is given in Fig. 31.

Shot-to-shot laser fluctuations as well as long-term fluctuations in the intensity of the electron beam are compensated for by normalizing the streak intensity associated with the heated surface to that associated with the unheated surface,  $I/I(T_{\text{bias}})$ , and averaging over  $\sim 800$  laser shots for each scan. Long-term laser fluctuations are controlled to within  $\pm 10\%$ . The spatial nonuniformity of the beam across the sample is determined to be  $\pm 15\%$  using a multi-shot image obtained with a two-dimensional array detector. A two-dimensional image and a line scan of the beam nonuniformity are given in Fig. 32. Figure 33 shows a histogram of the intensity distribution of the beam area of interest. The time-resolved temperature measurements are a result of the convolution of the temporal profile of the electron pulse with that of the surface temperature. The convolution effects are most significant for times where the rate of change of temperature with time is largest. This effect is not accounted for in this analysis, and, as a result, the peak surface temperature induced by the laser is actually somewhat larger than what is reported here. Time-resolved RHEED is further discussed in Ref. 21.



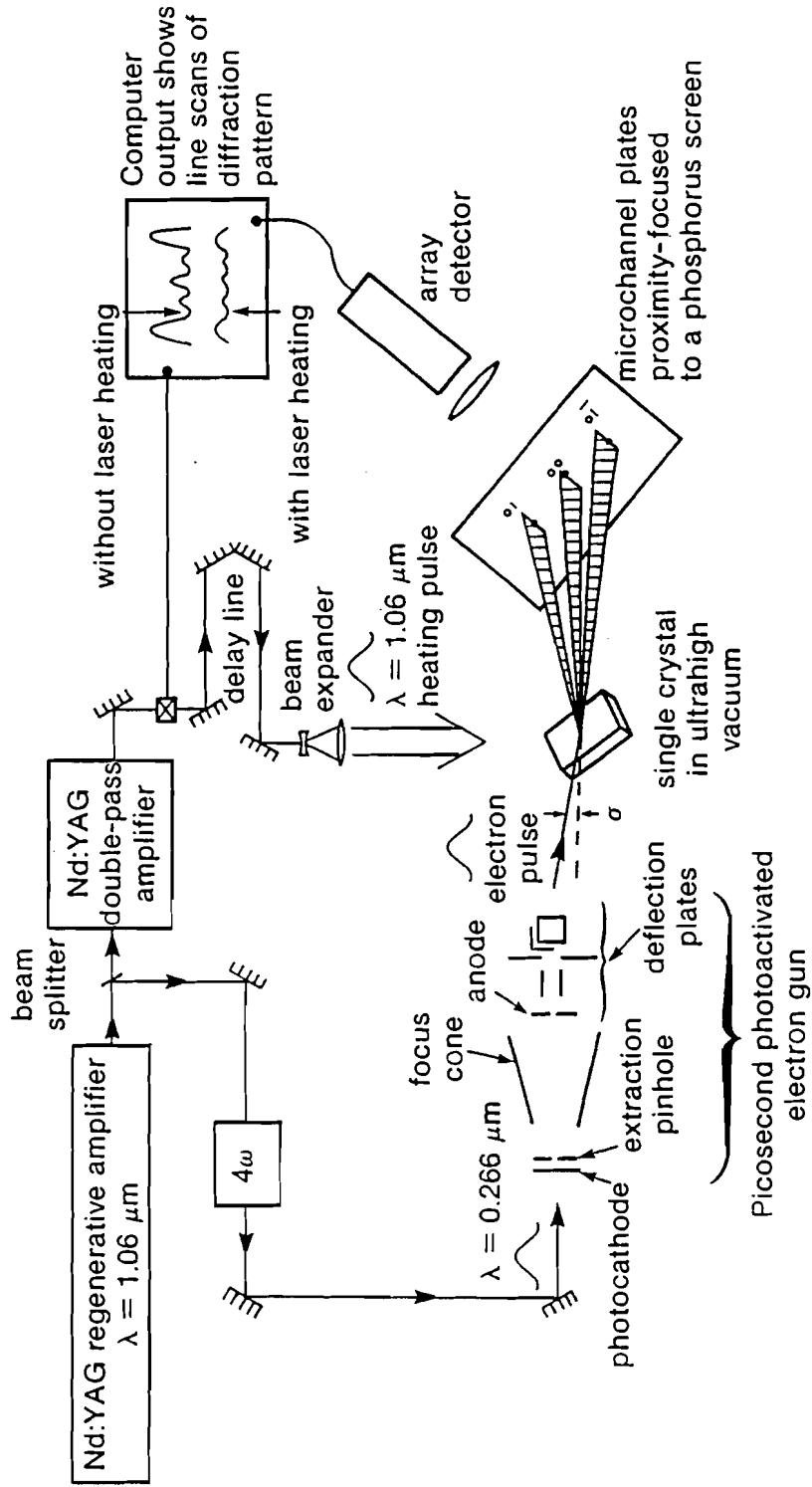


Figure 29: The time-resolved RHEED setup.

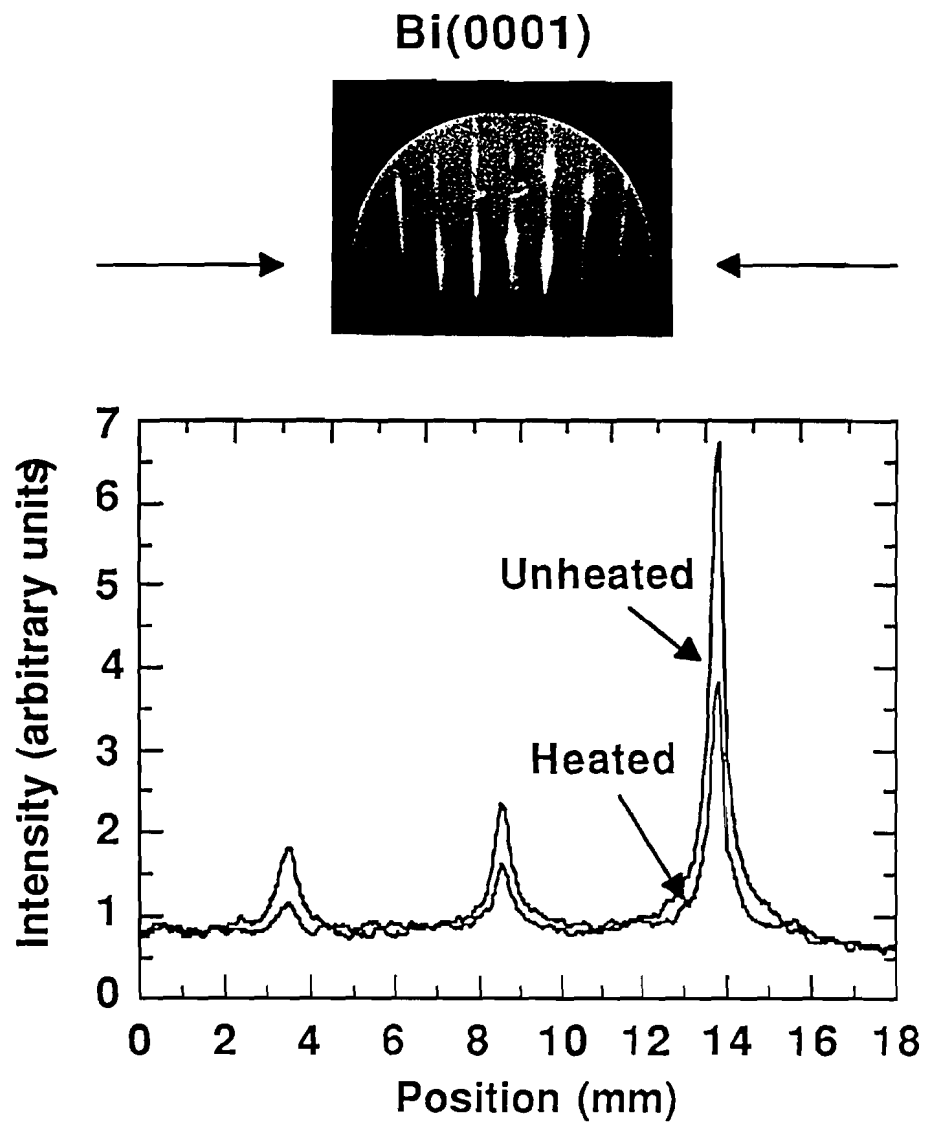


Figure 30: The diffraction intensity is monitored using a linear-array detector aligned with the peak intensity of the diffraction streak of interest. This figure shows the approximate alignment of the array detector and an example of heated and unheated line scans.

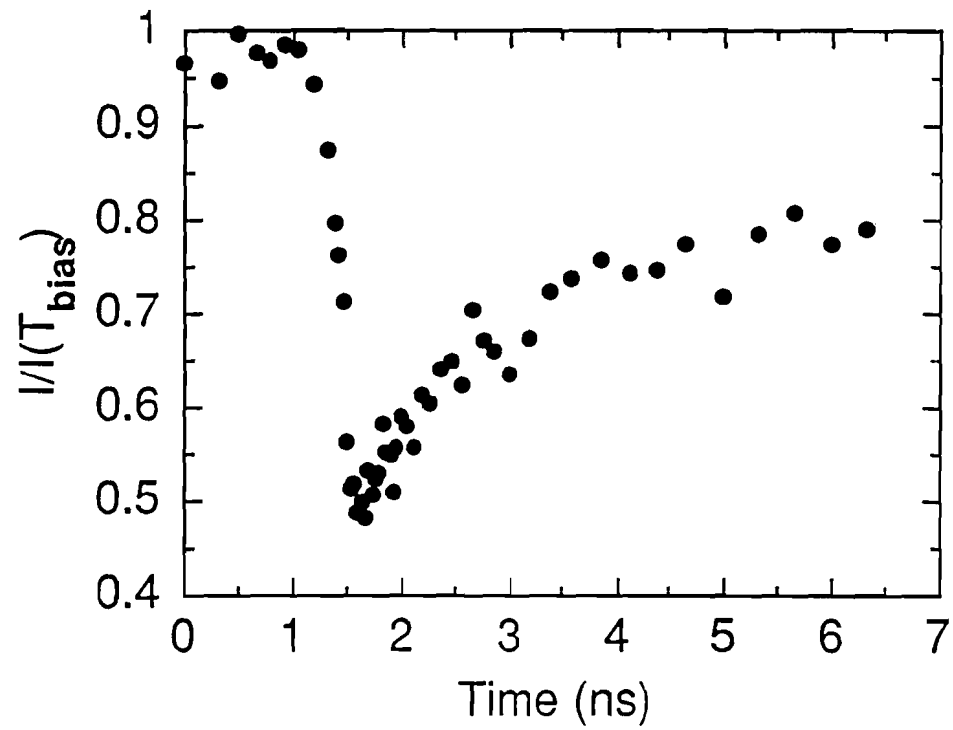


Figure 31: Time-resolved surface heating of Bi(0001) before, during, and after the arrival of the heating pulse at the surface.

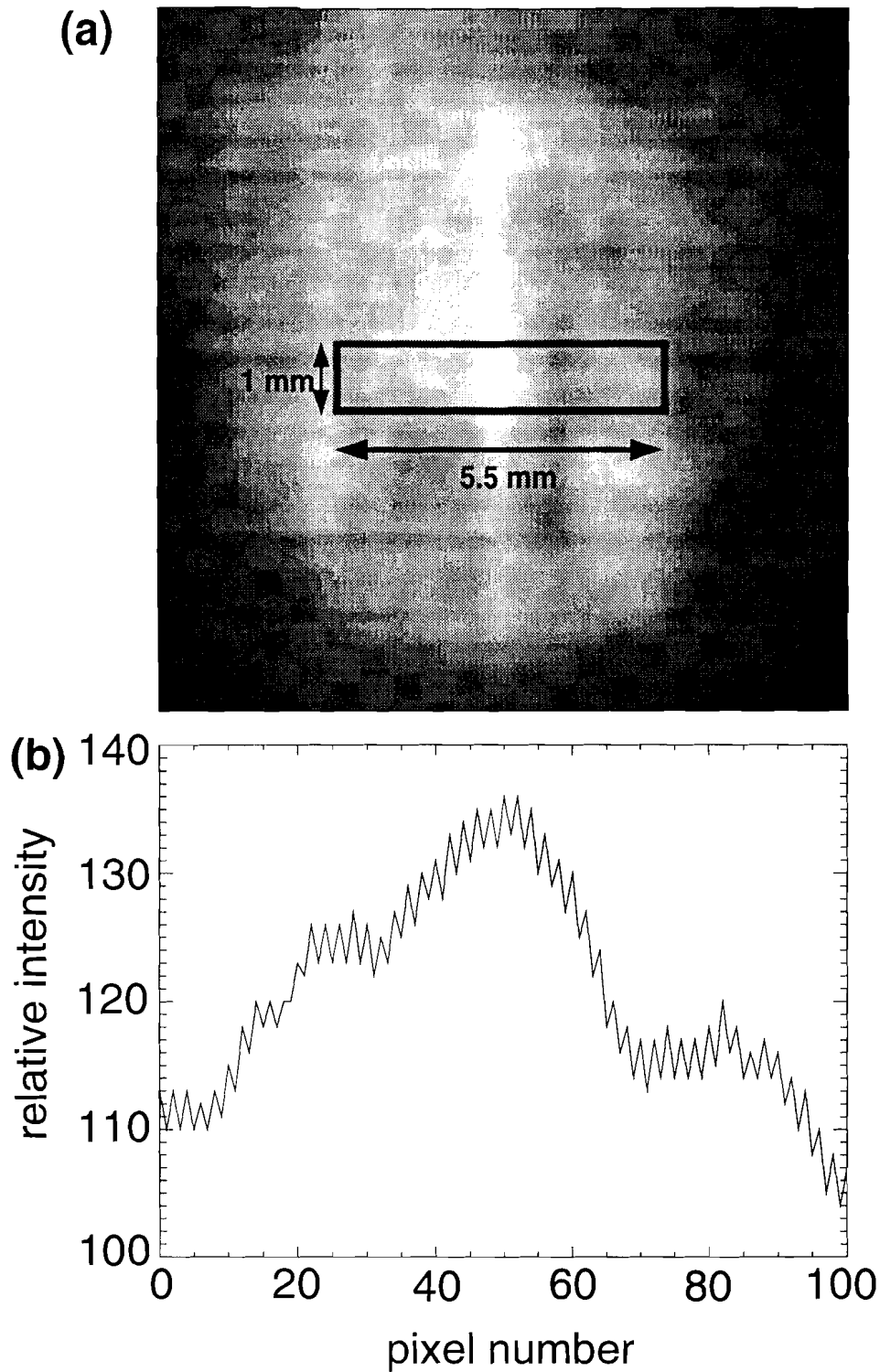


Figure 32: (a) The portion of the laser beam assumed to interact with the region of the surface probed by the electron beam is indicated by the box. The image is comprised of multiple laser shots. (b) A horizontal line scan through the center of the box. The noise in the line scan is due to pixel-to-pixel variation in the detector.

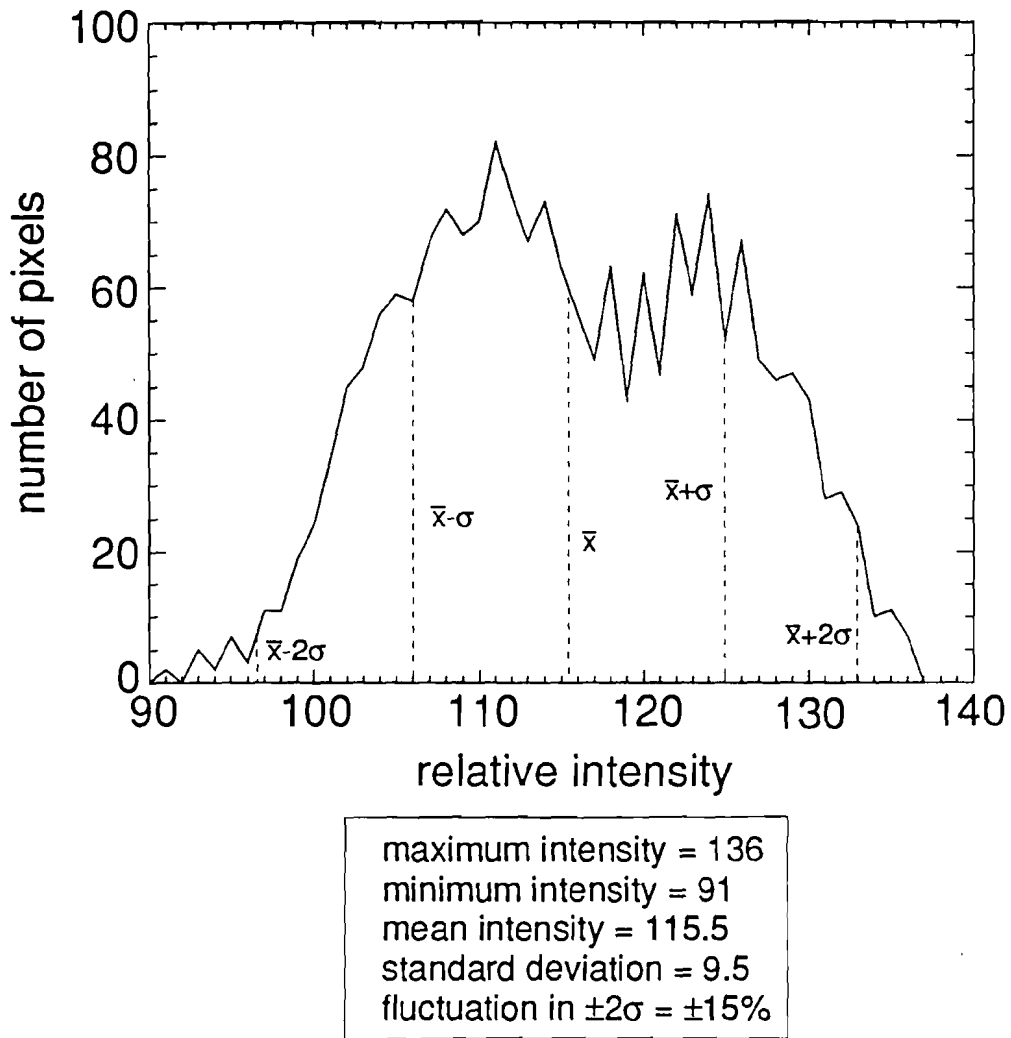


Figure 33: A histogram of the multishot laser-beam uniformity in the region indicated by the box in Fig. 32.

### 3.6 RESULTS AND DISCUSSION

In order to relate a given decrease in RHEED streak intensity to a temperature rise  $\Delta T$ , an intensity versus temperature calibration is obtained. Such a calibration is valid if the time scale of measurement is longer than the time needed for the electrons and lattice to equilibrate, which is typically a few picoseconds for metals<sup>22</sup>, and if no surface phase transitions or accumulated surface modifications occur. The sample is mounted on a resistively heated molybdenum stage, and the temperature is monitored by a thermocouple mounted on the surface. The thermocouple was calibrated to the freezing and boiling temperatures of water and to the melting temperature of Pb under vacuum in a previous experiment,<sup>11</sup> and to the melting temperature of Bi under vacuum. For the RHEED streak intensity versus temperature calibration, the electron gun is activated at a 1-kHz repetition rate with the frequency-quadrupled Nd:YAG laser. Examples of intensity versus temperature calibrations for each of the two samples studied are shown in Fig. 34. At least three calibrations were taken for each sample. The data are normalized to the streak intensity at the lowest temperature studied. The intensity of the diffraction pattern is consistent with Debye-Waller behavior up to the highest temperature studied, 523 K; i.e., the diffraction streak intensity is exponential with temperature indicating that no surface disordering occurs. The line fits of  $\ln[I/I(T_{\min})]$  versus  $T$  are forced through zero at the minimum temperature  $T_{\min}$ , and the best line fit is found by the method of least squares. From the slope of the calibration as well as parameters obtained from the RHEED pattern, a surface Debye temperature of  $42 \pm 9$  K can be extracted using the data from both samples, which is consistent with the previously reported value of  $48 \text{ K} \pm 20\%$  for Bi(0001) and Bi(01 $\bar{1}$ 2) using LEED.<sup>18</sup> The error bar is determined from the range of Debye temperatures calculated for all of the intensity calibration data. The bulk Debye

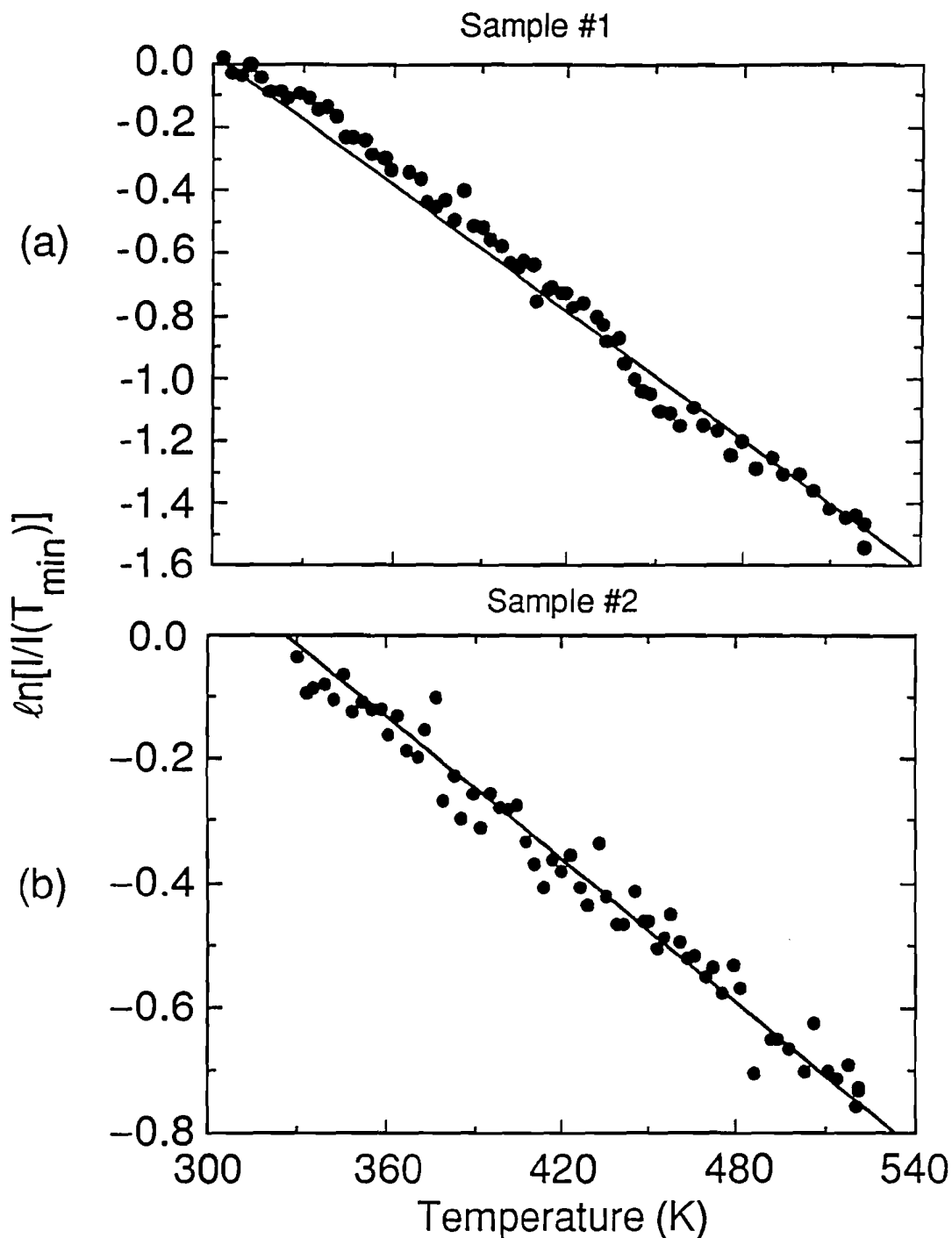


Figure 34: A calibration to determine the temperature rise induced by the laser. The intensity attenuation of the RHEED streaks is measured as a function of surface temperature. The behavior of  $\ln[I/I(T_{\min})]$  versus  $T$  can be explained by the Debye-Waller effect throughout the temperature range studied. A surface Debye temperature of  $42 \pm 9$  K is calculated for the Bi(0001) surface.

temperature for Bi is 120 K.<sup>23</sup> The Debye-Waller effect and the measurement of the surface Debye temperature using RHEED is discussed in greater detail in Appendix D. In Fig. 35, the ratio of heated to unheated diffraction intensities in Fig. 31 is converted to  $\Delta T$  using the calibration discussed here.

The time-resolved RHEED experiments are discussed next. To determine the maximum superheating temperature, observations of the behavior of  $I/I(T_{\text{bias}})$  versus peak laser intensity  $I_p$  for  $T_{\text{bias}} = 523$  K are made at four different time delays. Figure 36 shows  $\ln[I/I(T_{\text{bias}})]$  versus  $I_p$  for (a)  $t = t_0$ , (b)  $t = t_0 + 0.5$  ns, (c)  $t = t_0 + 1.0$  ns, and (d)  $t = t_0 + 4.0$  ns, respectively, where  $t_0$  is defined as the time of maximum modulation of  $I/I(T_{\text{bias}})$  due to heating. The linear regions in this Figure shows exponential decay consistent with Debye-Waller behavior. Deviation from this linear behavior is due to melting. By relating  $I_p$  to  $\Delta T$  using Figs. 34 and Fig. 36(a), the linear behavior of  $\ln[I/I(T = 523 \text{ K})]$  versus  $I_p$  at  $t = t_0$  is confirmed above  $T_m$  as a continuation of the Debye-Waller effect observed below  $T_m$ , within the experimental error. The linear relationship between  $\Delta T$  and  $I_p$  is established for low temperatures and then extrapolated to provide the temperature axis in Fig. 36. This is shown in Fig. 37 for the two samples used in the experiments where the line fits to the linear regions are forced through  $\ln[I/I(T_{\text{bias}})] = 0$  when  $I_p = 0$ . It is important to note that once  $\ln[I/I(T_{\text{bias}})]$  versus  $T$  deviates from linear behavior the relationship between  $I/I(T_{\text{bias}})$  and  $T$  is no longer known. The deviation corresponds to the onset of melting and increased laser energy is used to melt the sample rather than raise the temperature. The data for  $T$  above this deviation is shown for comparison reasons only.

In Fig. 36, the value of  $\ln[I/I(T_{\text{bias}})]$  corresponding to the maximum  $I_p$  before deviation from linear behavior is extracted and converted to a peak temperature rise  $\Delta T$  using the calibration in Fig. 34. It is found that for  $T_{\text{bias}} = 523$  K, observation of

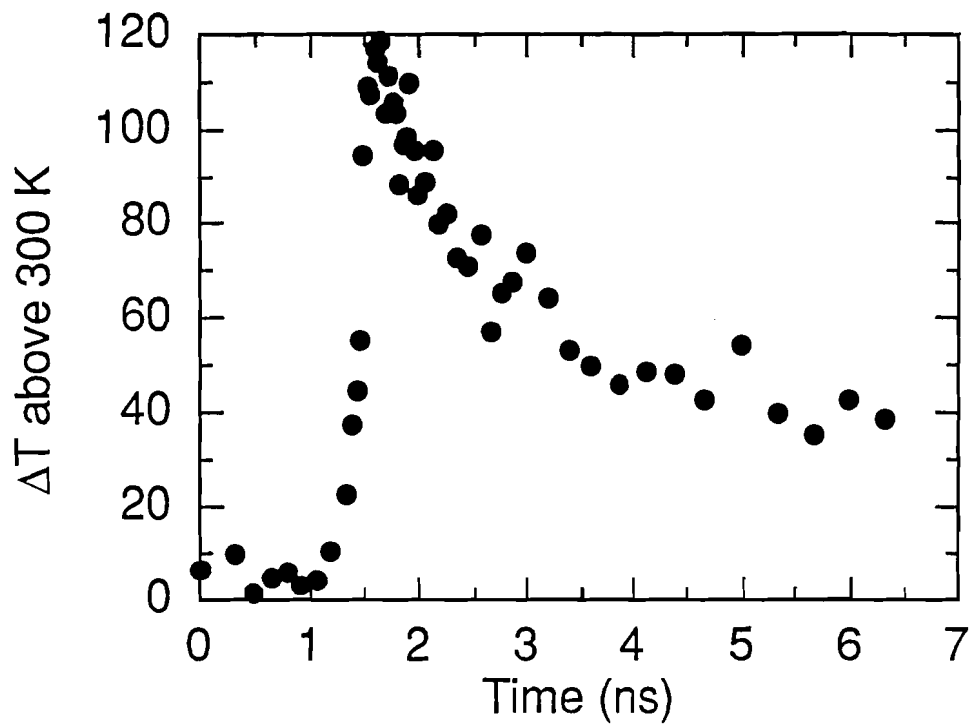
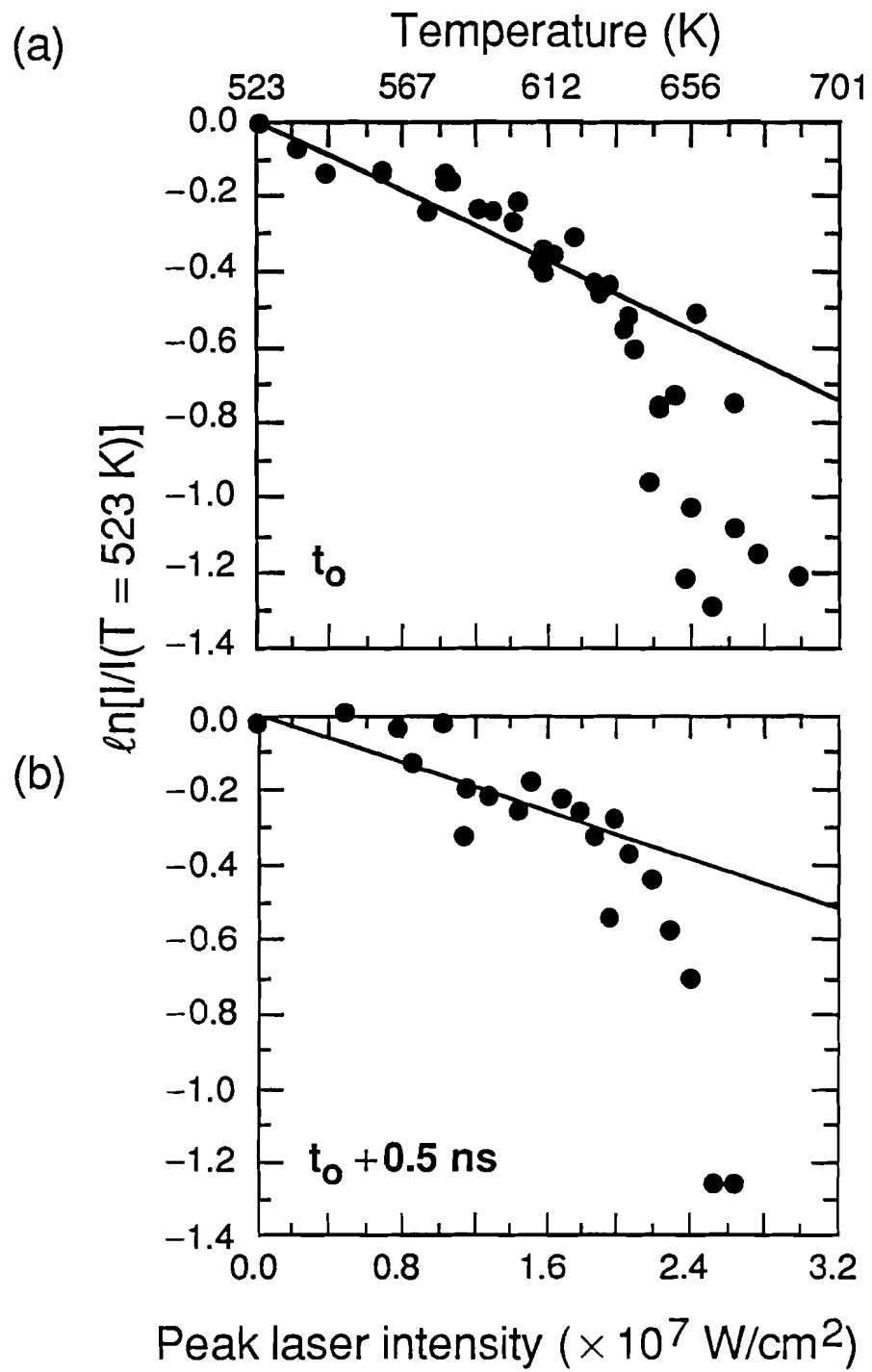


Figure 35:  $I(t)$  at  $T = 300$  K in Fig. 31 converted to  $\Delta T$ . A surface temperature rise of  $110 \pm 25$  K is induced by a peak laser intensity of  $2.0 \pm 0.2 \times 10^7$  W/cm<sup>2</sup>.



*continued on next page*

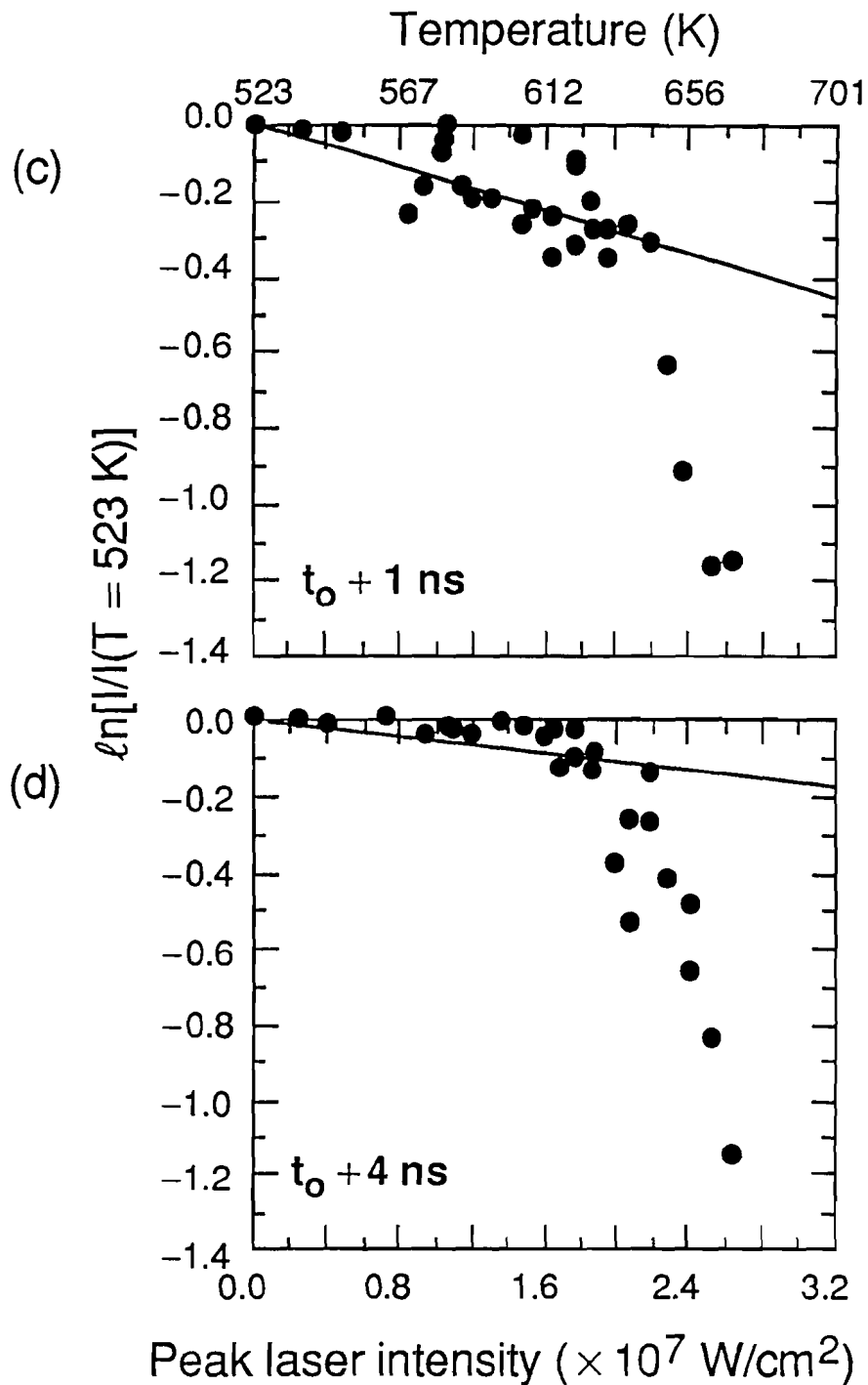


Figure 36: The logarithm of the ratio of the heated streak intensity to the intensity at  $T_{\text{bias}} = 523$  K versus peak laser intensity for (a)  $t = t_0$ , (b)  $t = t_0 + 0.5$  ns, (c)  $t = t_0 + 1.0$  ns, and (d)  $t = t_0 + 4.0$  ns. Deviation from Debye-Waller behavior corresponds to the onset of melting. Superheating of Bi(0001) occurs up until the break from the line fit that occurs at  $2.0 \pm 0.2 \times 10^7$  W/cm $^2$ , a superheating temperature of  $90 \pm 25$  K.

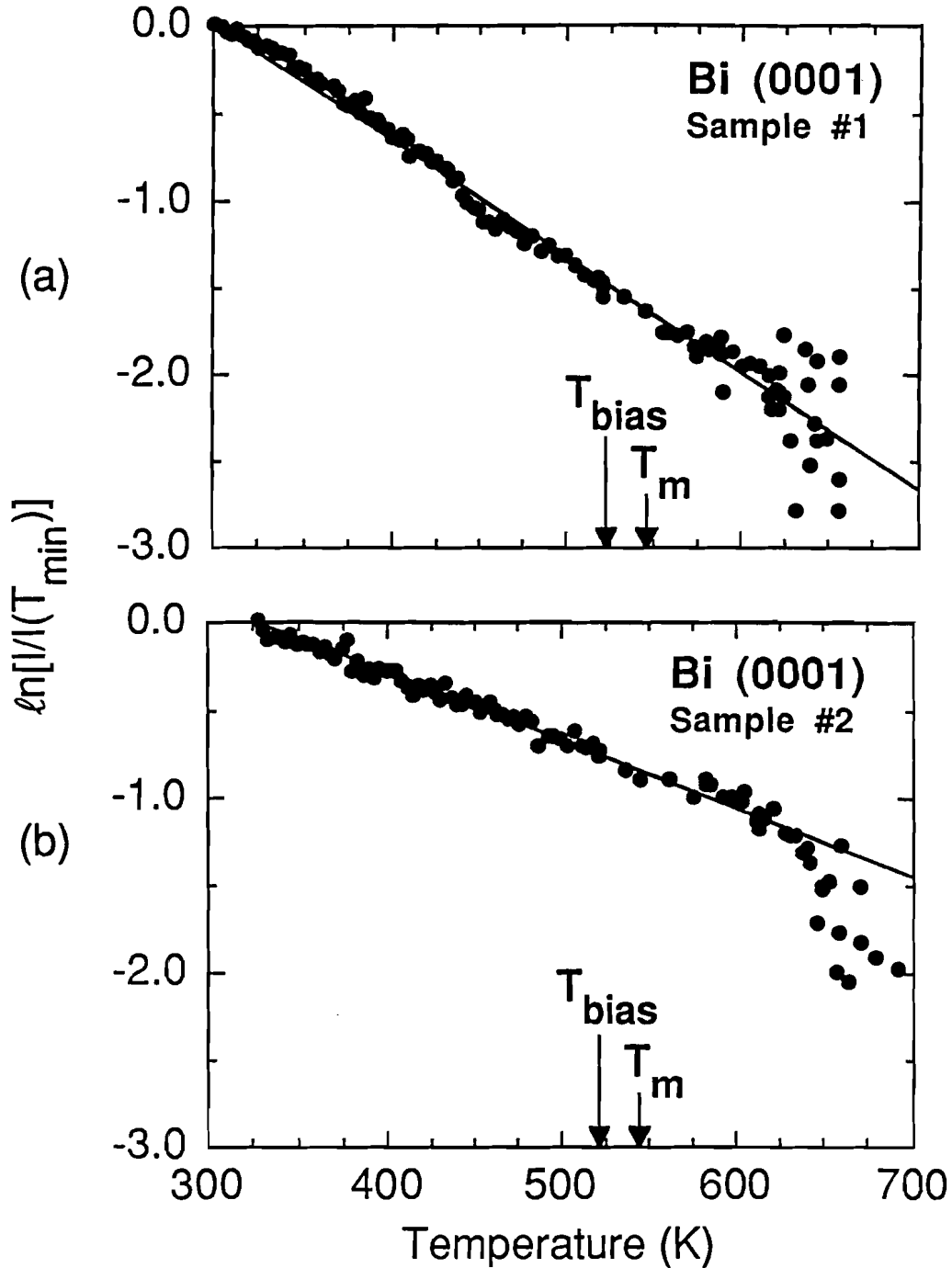
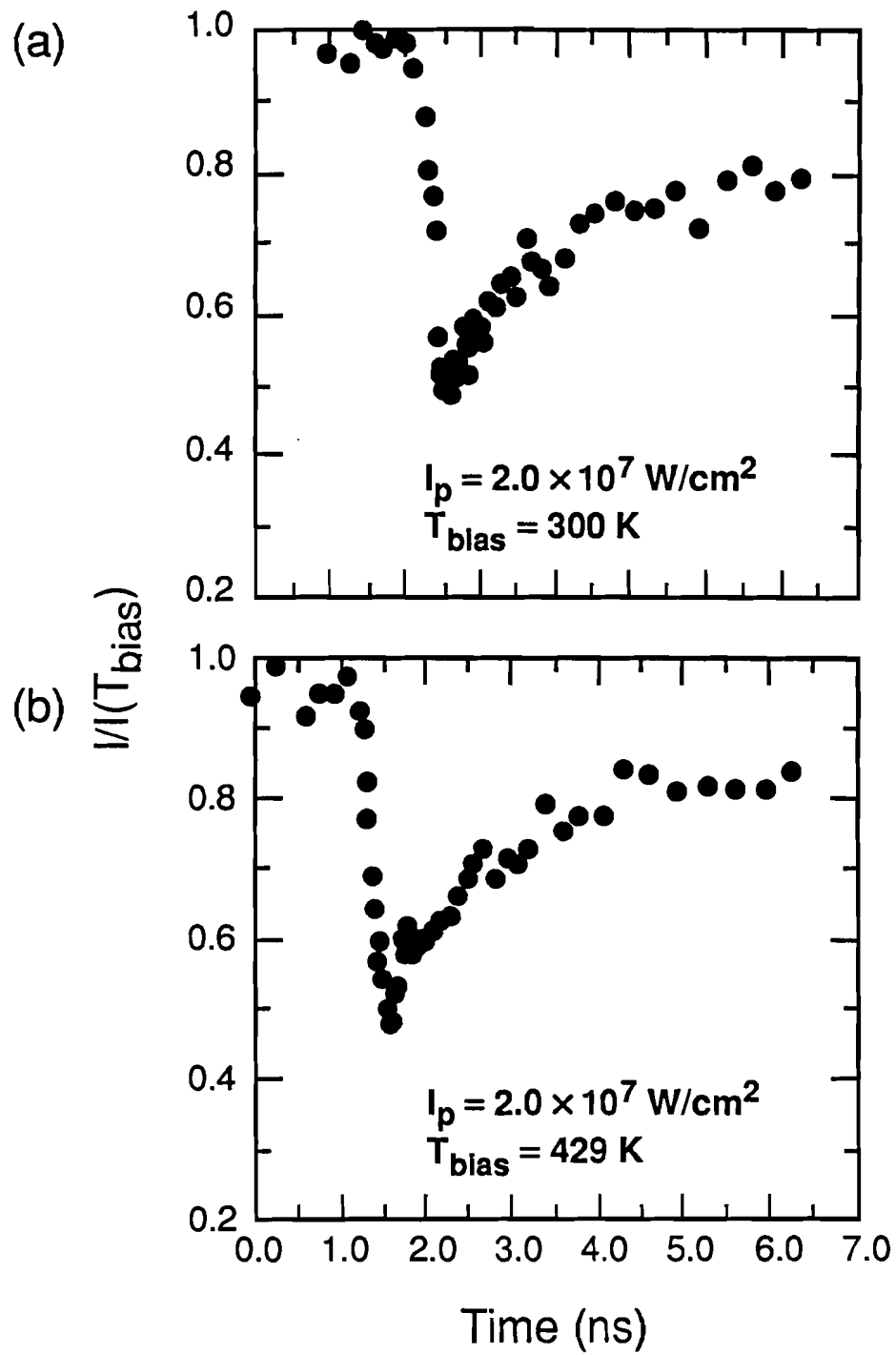


Figure 37: Figures 34 and 36 combined to show the extension of Debye-Waller behavior above  $T_m$  for both samples used in the experiment. Deviation from this behavior is seen near  $T = T_m + 90$  K, the maximum superheating temperature. This deviation corresponds to the onset of melting and increased laser energy is used to melt the sample rather than raise the temperature. The data for  $T$  above this deviation temperature is therefore shown for comparison reasons only.

melting occurs for  $I_p = 2.0 \pm 0.2 \times 10^7 \text{ Wcm}^{-2}$ . This corresponds to  $\Delta T = 110 \pm 25 \text{ K}$  or equivalently, a superheating temperature of  $90 \pm 25 \text{ K}$ , not accounting for convection effects. Included in this error bar is the range of temperatures obtained from the values of  $I_p$  corresponding to the point of deviation from Debye-Waller behavior in Fig. 36 ( $\pm 15 \text{ K}$ ), the error in converting intensity to temperature from the calibration of Fig. 34 ( $\pm 9 \text{ K}$ ), and the temperature introduced by the spatial nonuniformity of the laser, shown in Figs. 32 and 33 ( $\pm 15 \text{ K}$ ).

Ultrafast surface heating to peak temperatures below and above  $T_m$  is studied by temperature biasing the sample between room temperature and  $T_m - 21 \text{ K}$  while monitoring the modulation of the streak intensity before, during, and after the arrival of the heating pulse. Figure 38 shows  $I/I(T_{\text{bias}})$  versus delay time  $t$ . For  $T_{\text{bias}} = 300 \text{ K}$  and  $I_p = 2.0 \times 10^7 \text{ Wcm}^{-2}$  [Fig. 38(a)], the change in surface temperature  $\Delta T$  at  $t = t_0$ , is approximately  $115 \text{ K}$ . The surface temperature remains below  $T_m$ . In Fig. 38(b),  $T_{\text{bias}} = 429 \text{ K}$  and  $I_p = 2.0 \times 10^7 \text{ Wcm}^{-2}$ . The laser heating raises the surface temperature to  $\sim T_m$ . For  $T_{\text{bias}} = 512 \text{ K}$  and  $I_p = 2.0 \times 10^7 \text{ Wcm}^{-2}$  [Fig. 38(c)], the surface is heated to  $\sim T_m + 90 \text{ K}$ , approximately the maximum observed superheating temperature. When  $I/I(T_{\text{bias}})$  is converted to temperature using the calibration of Fig. 34, the temporal evolution of surface temperature is qualitatively consistent with a one-dimensional, heat-diffusion model.<sup>24,25</sup> The heat-diffusion model is discussed in Appendix E. For  $T_{\text{bias}} = 523 \text{ K}$  and  $I_p = 2.4 \times 10^7 \text{ Wcm}^{-2}$  [Fig. 38(d)], the maximum superheating temperature is exceeded and melting occurs. This is indicated by a strong deviation from the behavior predicted by the heat-diffusion model [i.e., difference in the behavior of Fig. 38(d) for  $t$  far from  $t_0$  when compared to Figs. 38(a)–(c)] as well as visible laser damage to the surface. The sample is monitored visually to obtain a qualitative estimate of the threshold for laser damage and it is found that the



*continued on next page*

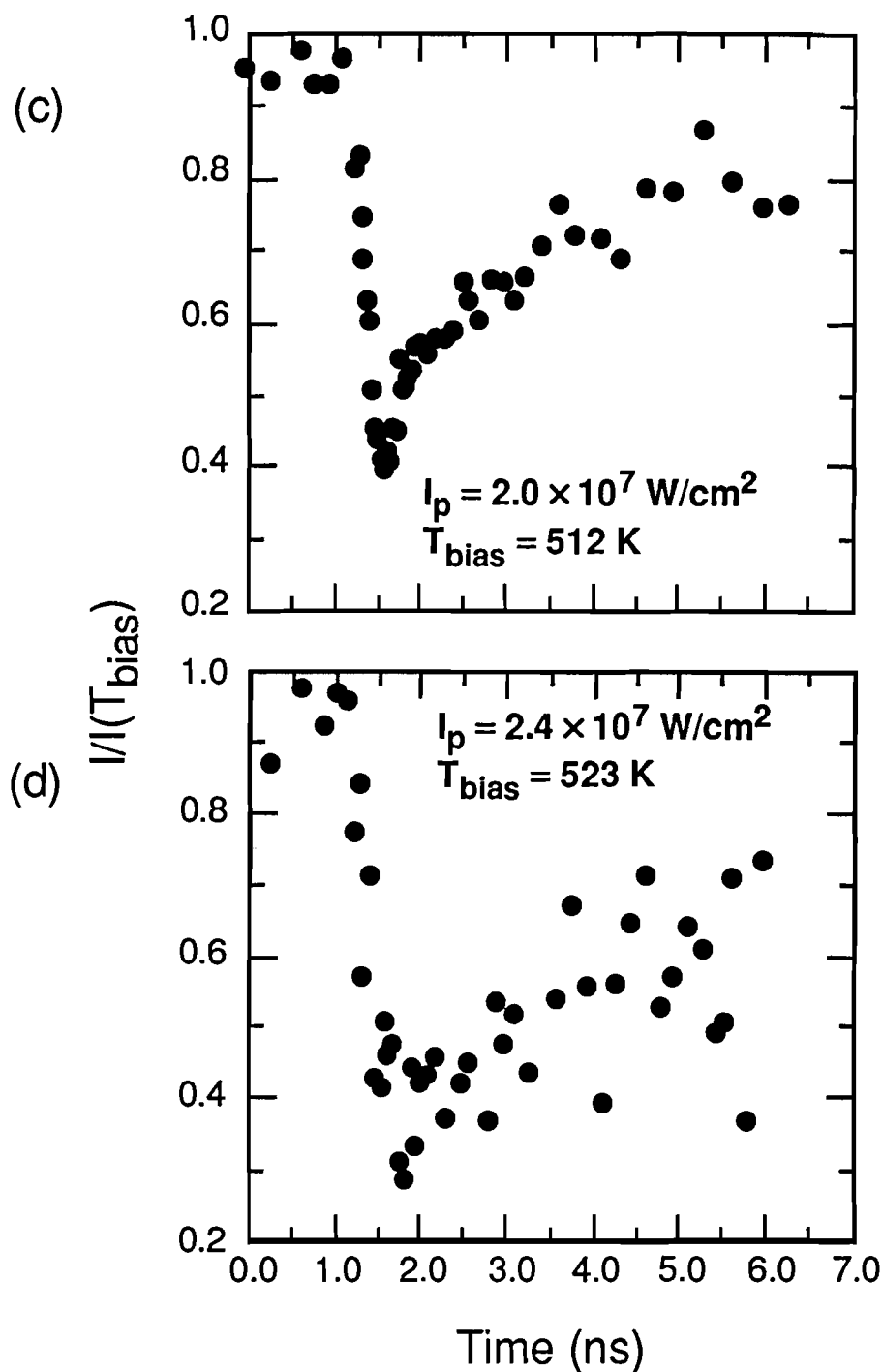


Figure 38: The ratio of the heated streak intensity to the intensity at the bias temperature versus delay time for various bias temperatures. At temperatures below that of maximum superheating [(a)–(c)], the behavior is qualitatively consistent with a one-dimensional heat-diffusion model for laser heating both below and above  $T_m$ . The heat-diffusion model is discussed in Appendix E. Melting is evidenced in (d) as a deviation from this behavior.

earliest visual observations of damage coincide with the point at which  $\ln[I/I(T_{\text{bias}})]$  versus  $I_p$  deviates from linear behavior.

### 3.7 LASER-INDUCED SURFACE DAMAGE OF Bi(0001)

After laser damage has occurred, the original RHEED streaks are still visible but their intensities are diminished, indicating a reduction in surface quality. The sample was checked for the formation of new crystalline structures by searching for RHEED patterns not corresponding to the Bi(0001) surface. However, the only patterns observed correspond to the Bi(0001) surface, indicating that the damaged surface is made up of epitaxial and possibly amorphous regions. The reflectivity of the surface is measured for  $\lambda = 1.06 \mu\text{m}$  at 300 K both before and after the occurrence of laser damage and it is found that the reflectivity has decreased from 0.67 to 0.49. SEM images of the laser-damaged surface show melted regions which are referred to here as "rows" and "dots". Figures 39 and 40 are a photograph of the damaged surface, and SEM images of the undamaged and damaged surface, respectively. The laser-induced surface structure is observed to have a periodicity about equal to the wavelength of the laser. The damaged surface can be seen in Fig. 41 with higher resolution. This periodic structure forms in a hexagonal arrangement of dots, which in some places coalesce into parallel rows.

Previous pulsed-laser melting experiments on the (0001),  $(\bar{1}010)$ , and  $(2\bar{1}\bar{1}0)$  surfaces of Bi with a ruby laser with a 30-ns pulse width have shown defect formation on the  $(\bar{1}010)$  and  $(2\bar{1}\bar{1}0)$  surfaces resulting from mechanical stress induced by slip planes parallel to the (0001) surface. In these experiments, the Bi(0001) surface regrew epitaxially from the liquid with no laser-induced periodic surface structure observed.<sup>26</sup> The different behavior observed in the time-resolved RHEED experiments



Figure 39: Laser-induced damage on Bi(0001) shows grating-like properties.

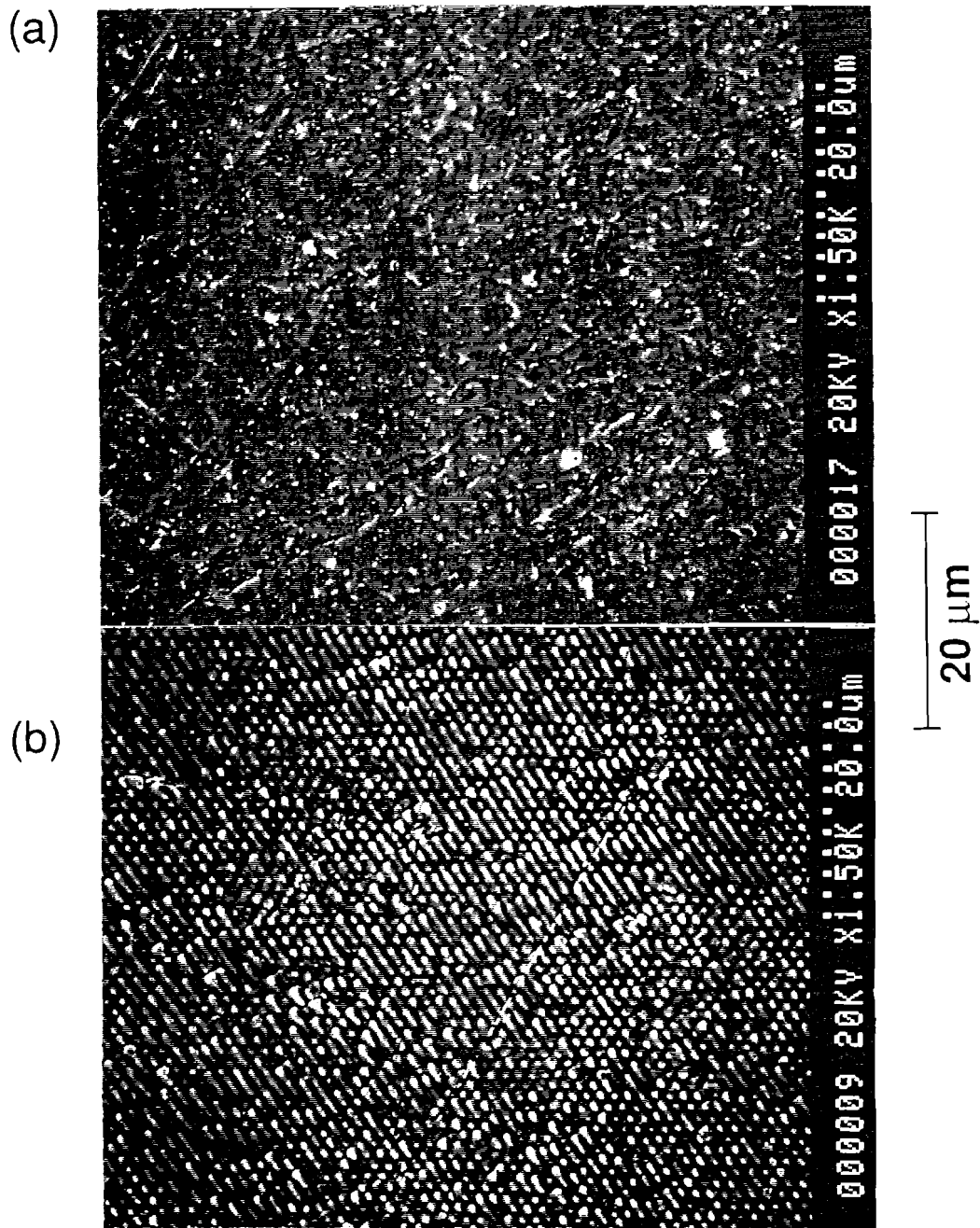
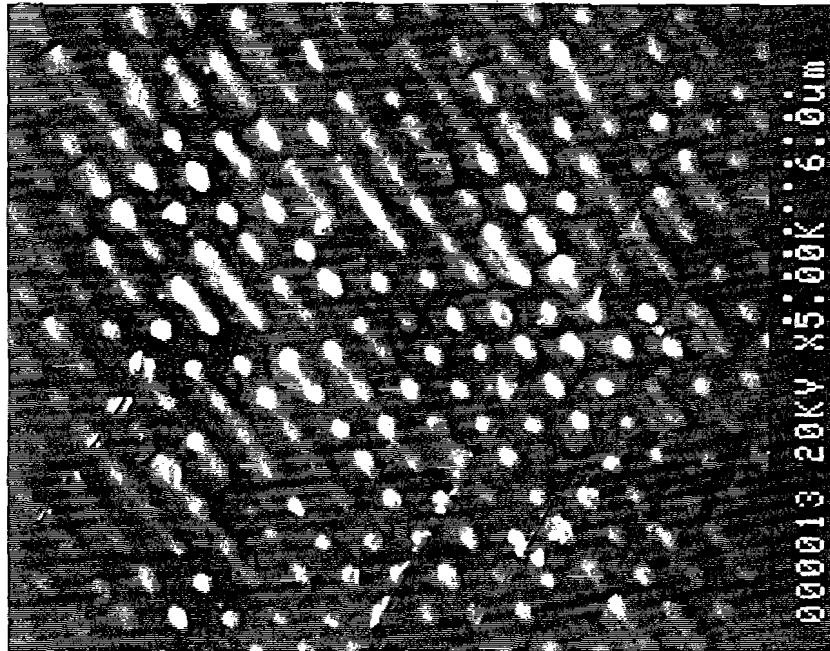


Figure 40: Scanning electron microscopy images of the (a) undamaged and (b) damaged Bi(0001) surface show characteristic properties of the mechanical polishing process, and a laser-induced surface structure consisting of ripples and “dots” with spacing equal to the wavelength of the laser, respectively.



6  $\mu\text{m}$

Figure 41: The scanning-electron microscopy image of the laser-damaged surface with higher resolution.

reported on here could be related to the two-orders-of-magnitude difference in pulse width.

Laser-induced periodic surface structure (LIPSS) has been found to occur on a variety of metals and semiconductors for a wide range of laser wavelengths, pulse widths, and polarizations states.<sup>27</sup> If a linearly-polarized laser beam causes damage to occur on a metallic or semiconducting surface at normal incidence, the resulting surface structures are rows of fringes with spacing equal to the wavelength of the laser and orientation perpendicular to the laser polarization. Circular polarization results in a two-dimensional damage pattern corresponding to the superposition of the one-dimensional damage structure associated with linear polarization occurring in all directions in the surface plane. LIPSS is generally believed to be the result of the interference between the incident wave and a surface-scattered wave, which causes inhomogeneous absorption of the incident-beam energy and originates from a surface defect, such as a scratch. LIPSS can be produced with a single laser shot, and after multiple shots the damage pattern is generally independent of the micro-roughness of the surface as well as particular beam qualities.<sup>27</sup>

As mentioned above, the spacing between the rows and dots that is observed on Bi(0001) is consistent with the wavelength of the laser. However, the periodic arrangement of the dots cannot be satisfactorily explained by the theory described above. The laser polarization is primarily linear, with only a very small elliptically-polarized component (<5%) resulting from the imperfections in the optics and their alignment. In addition, the hexagonal pattern is more regular than commonly observed for laser-induced damage from a circularly-polarized laser. It is suggested that the hexagonal structure may be a result of the thermal properties of Bi, rather than the properties of the laser<sup>28</sup>, and may be related to the underlying crystal structure.

Other cases in which the damage pattern appears to be related to the underlying crystal structure have been reported. For example, single-crystal Si subject to microsecond pulses from a Nd:glass laser have been shown to exhibit surface structures which are independent of the angle of incidence and polarization of the laser. The orientation of the structures has been found to be related to the orientation of the crystallographic axes on the surface. It is suggested that this is due to anisotropy in the elastic properties of crystalline Si which result in anisotropic strain during rapid heating and cooling of the near-surface region.<sup>29</sup> This leads us to believe that the anisotropic properties of Bi, as well as its negative volume change upon melting could very possibly result in thermally-produced surface structures during pulsed-laser melting of the near-surface region.

Anisotropic behavior of thermal, electrical, physical, and mechanical properties of Bi are all results of the anisotropic bonding character of its rhombohedral structure. For example, the thermal conductivity parallel to the Bi(0001) surface is nearly a factor of two larger than it is perpendicular to this surface.<sup>25</sup> In addition, other properties such as the critical-resolved shear stress, linear thermal expansion, and electrical resistivity, differ greatly in the direction perpendicular to the (0001) surface in comparison to parallel directions.<sup>26,30</sup> The open crystal structure of Bi leads to its contraction upon melting. This negative volume change is a unique property experienced only by a few elemental crystals such as Ga, Si, Ge, and Sb.<sup>13,29</sup>

In the previous superheating experiments on Pb(111),<sup>10</sup> with the sample biased close to  $T_m$ , surface damage was induced by the laser for an  $I_p$  much larger than the  $I_p$  which corresponded to maximum superheating. This damage was not investigated on a microscopic level and hence the damage structure was not determined. However, this damage could be removed by pulsed-laser melting with higher peak laser intensities.

For Pb(111) the threshold for pulsed-laser melting is lower than the threshold for pulse-laser damage, in contrast to Bi(0001) for which these two thresholds appear to be about the same. Although laser-induced damage was not investigated on the Pb(111) surface, it is interesting to note some of the qualitative differences in what is observed on Bi and Pb. In contrast to Bi, Pb is isotropic in terms of the nature of its bonding and thermal, mechanical, and other properties.

### 3.8 CONCLUSIONS

In conclusion, using time-resolved RHEED superheating of Bi(0001) by  $90 \pm 25$  K is observed. Superheating is characterized by an extension of the Debye-Waller region observed below  $T_m$  to temperatures above that of bulk melting. Although no surface melting is observed on the Bi(0001) surface in the temperature range studied, the surface Debye temperature is significantly reduced when compared to the bulk Debye temperature. This corresponds to increased lattice vibrations of surface atoms. For laser heating corresponding to  $\Delta T$  larger than that of maximum superheating, melting is observed as a deviation from Debye-Waller behavior. For these larger heatings, irreversible laser damage results in a superposition of one- and two-dimensional laser-induced periodic surface structures. The spacing of both types of structures appears to be equal to the wavelength of the laser. The one-dimensional structure is consistent with the type of damage expected from a linearly-polarized laser.<sup>27</sup> However, the hexagonal periodic surface structure is not similar to commonly observed surface damage and is most likely related to the anisotropic properties of crystalline Bi. Bi, in contrast to face-centered-cubic metals, has many distinct physical properties related to its unusual crystal structure. Therefore, the observations of

superheating of Bi(0001), coupled with the previously observed superheating of Pb(111)<sup>10</sup>, strongly suggest the generality of the superheating phenomenon.

### 3.9 REFERENCES

1. G. D. T. Spiller, *Philos. Mag. A* **46**, 535 (1982).
2. J. J. Métois and J. C. Heyraud, *J. Phys. (Paris)* **50**, 3175 (1989).
3. S. J. Peppiatt, *Proc. R. Soc. Lond. A* **345**, 401 (1975).
4. M. Blackman, S. J. Peppiatt, and J. R. Sambles, *Nature (Phys. Sci.)* **239**, 61 (1972).
5. J. Daëges, H. Gleiter, and J. H. Perepezko, in *Phase Transitions in Condensed Systems—Experiments and Theory*, edited by G. S. Cargill, F. Spaepen, and K.-N. Tu (Materials Research Society, Pittsburgh, 1987), Vol. 57, p. 67–78.
6. S. E. Kaykin and N. P. Bene, *C. R. Acad. Sci. USSR* **23**, 31 (1939).
7. A. P. Baikov and A. G. Shestak, *Sov. Tech. Phys. Lett.* **5**, 569 (1979).
8. C. J. Rossouw and S. E. Donnelly, *Phys. Rev. Lett.* **55**, 2960 (1985).
9. L. Gråbaek, J. Bohr, E. Johnson, A. Johansen, L. Sarholt-Kristensen, and H. H. Andersen, *Phys. Rev. Lett.* **64**, 934 (1990).
10. J. W. Herman and H. E. Elsayed-Ali, *Phys. Rev. Lett.* **69**, 1228 (1992).
11. J. W. Herman and H. E. Elsayed-Ali, *Phys. Rev. Lett.* **68**, 2952 (1992).
12. J. D. Mackenzie and R. L. Cormia, *J. Chem. Phys.* **39**, 250 (1963).
13. B. R. T. Frost, *Progr. Met. Phys.* **5**, 96 (1954).
14. F. Jona, *Surf. Sci.* **8**, 57 (1967).
15. M. Born, *J. Chem. Phys.* **7**, 591 (1939).
16. S. R. Phillpot, S. Yip, and D. Wolf, *Computers in Physics NOV/DEC* **20**, (1989).
17. J. W. Herman, H. E. Elsayed-Ali, and E. A. Murphy, *Phys. Rev. Lett.* **71**, 400 (1993).
18. R. M. Goodman and G. A. Somorjai, *J. Chem. Phys.* **52**, 6325 (1970).
19. J. E. Mahan, K. M. Geib, G. Y. Robinson, and R. G. Long, *J. Vac. Sci. Technol. A* **8**, 3692 (1990).

20. M. G. Lagally, *Methods of Experimental Physics*, edited by R.L. Park and M. G. Lagally (Academic Press, 1985) Vol. 22, p. 237–298.
21. H. E. Elsayed-Ali and J. W. Herman, *Rev. Sci. Instrum.* **61**, 1636 (1990).
22. H. E. Elsayed-Ali, T. B. Norris, M. A. Pessot, and G. A. Mourou, *Phys. Rev. Lett.* **58**, 1212 (1987).
23. N. W. Ashcroft and N. D. Mermin, *Solid State Physics* (W. B. Saunders Company, Philadelphia, PA, 1976).
24. J. H. Bechtel, *J. Appl. Phys.* **46**, 1585 (1975).
25. *Thermophysical Properties of Matter*, edited by Y. S. Touloukian (Plenum Press, New York, 1970), Vols. 1 and 2; J. N. Hodgson, *Proc. Phys. Soc. (London)* **B67**, 269 (1954).
26. A. L. Helms, Jr., C. W. Draper, D. C. Jacobson, J. M. Poate, and S. L. Bernasek, *J. Mater. Res.* **3**, 1097 (1988); A. L. Helms, Jr., C.-C. Cho, S. L. Bernasek, C. W. Draper, D. C. Jacobson, and J. M. Poate, in *Laser Surface Treatment of Metals*, edited by C. W. Draper and P. Mazzoldi (Martinus Nijhoff Publishers, Dordrecht, The Netherlands, 1986), p. 141–156; A. L. Helms, Jr., C. W. Draper, D. C. Jacobson, J. M. Poate, and S. L. Bernasek, in *Energy Beam-Solid Interactions and Transient Thermal Processing*, edited by D. K. Biegelsen, G. A. Rozgonyi, and C. V. Shank (Materials Research Society, Pittsburgh, 1985), Vol. 35, p. 439–444.
27. J. E. Sipe, J. F. Young, J. S. Preston, and H. M. van Driel, *Phys. Rev. B* **27**, 1141 (1983); J. F. Young, J. S. Preston, H. M. van Driel, and J. E. Sipe, *Phys. Rev. B* **27**, 1155 (1983), and references therein.
28. H. M. van Driel, private communication.
29. V. P. Veiko, I. A. Dorofeev, Ya. A. Imas, T. I. Kalugina, M. N. Libenson, and G. D. Shandybina, *Sov. Tech. Phys. Lett.* **10**, 6 (1984).
30. S. Otake, H. Namazue, and N. Matsuno, *Japan. Journ. Appl. Phys.* **19**, 433 (1980).

## APPENDIX A

### AUGER ELECTRON AND PHOTOELECTRON SPECTROSCOPY

Most elements have their strongest photoelectron and Auger peaks for electron energies <1000 eV. Therefore, because of the relatively short mean-free path of electrons in solids at this energy, XPS and AES indeed provide a compositional analysis of the first few atomic layers. Tables of the energies corresponding to strong photoelectron and Auger peaks can be found in the literature.<sup>1,2</sup>

#### A.1 X-RAY PHOTOELECTRON SPECTROSCOPY (XPS)

In XPS, incident photons result in ejecting core-level electrons from near-surface atoms. The kinetic energy of the ejected photoelectron is

$$E_k = h\nu - E_b - \phi, \quad (\text{A.1})$$

where  $h\nu$  is the x-ray energy,  $E_b$  is the core-level binding energy and  $\phi$  is the work function of the surface from which the electron escapes. The energy of the ejected electron is characteristic of the type of atom from which it came, and a scan of the number of electrons versus energy, shown in Fig. 3 for clean Pb, provides information on the chemical composition of the near-surface region of the sample.

#### A.2 AUGER ELECTRON SPECTROSCOPY (AES)

AES involves a slightly more complicated process than does XPS. An Auger electron results from the following process. First, an incident electron with a known energy ejects a core-level electron from energy level  $W$ . This is an unstable configuration making it highly probable that an electron will drop from a more shallow

energy level X to energy level W releasing energy  $E_W - E_X$ . This energy release either results in the ejection of an electron from shell Y or the release of a photon with the corresponding energy. The electron resulting from this process is called an Auger electron and has energy

$$E = E_W - E_X - E_Y, \quad (\text{A.2})$$

which is characteristic of the type of atom from which the electron came and is independent of the incident electron energy. If the energy E is large enough, the electron can escape from the sample and its energy can be measured. Because of the poor signal to noise ratio in the measurement of the number of Auger electrons N versus energy E, the derivative of the distribution  $\frac{dN}{dE}$  is more commonly measured. A plot of  $\frac{dN}{dE}$  versus E for clean and contaminated Bi can be found in Fig. 23. It is convention to label Auger peak energies as the sharp minima of  $\frac{dN}{dE}$ . The energy values listed in Fig. 23 correspond to the minima of the indicated peaks.<sup>3</sup>

## REFERENCES

1. C. D. Wagner, W. M. Riggs, L. E. Davis, and J. F. Moulder, *Handbook of X-ray Photoelectron Spectroscopy* edited by G. E. Muilengberg (Physical Electronics Industries, Eden Prairie, MN 1978).
2. L. E. Davis, *Handbook of Auger Electron Spectroscopy* Second Edition (Physical Electronics Industries, Eden Prairie, MN 1976).
3. J. C. Rivière, *Contemp. Phys.* **14**, 513 (1973).

## APPENDIX B

### HEMISPHERICAL ENERGY ANALYZER

The type of spectrometer used in the x-ray photoelectron diffraction studies is an angular dispersive electron spectrometer (ADES500) sold by VG Microtech, a diagram of which is shown in Fig. 42. Horizontal rotation of  $180^\circ$  (in the plane of the page in Fig. 42) allows for full angular scans and  $90^\circ$  vertical rotation allows for accurate alignment relative the sample.

The spectrometer consists of a  $150^\circ$  50-mm mean radius hemispherical analyzer with 2-mm slits at either end. The electrons which make it through both slits enter a channeltron detector. The channeltron consists of a small curved glass tube coated with a high resistance material that acts as an electron multiplier. One electron can generate approximately  $10^8$  electrons upon traversing the length of the tube under optimal experimental conditions. The charge pulse is then detected by a pulse amplifier-discriminator and stored for computer display and analysis. For x-ray photoelectron diffraction the spectrometer is run in constant energy mode. Therefore, electrons with energy  $E$  will reach the detector where  $E$  is determined from

$$e\Delta V = E( R_2/R_1 - R_1/R_2 ) \quad (\text{B.1})$$

where  $e$  is the charge of an electron,  $\Delta V = V_1 - V_2$  is the difference between the voltages on the inner and outer cylinders, and  $R_1$  and  $R_2$  are the radii of the inner and outer spheres, respectively.

#### REFERENCES

1. J. C. Rivière, *Practical Surface Analysis by Auger and X-ray Photoelectron Spectroscopy*, Eds. D. Briggs and M. P. Seah (Wiley and Sons, 1983) pp. 80-84.

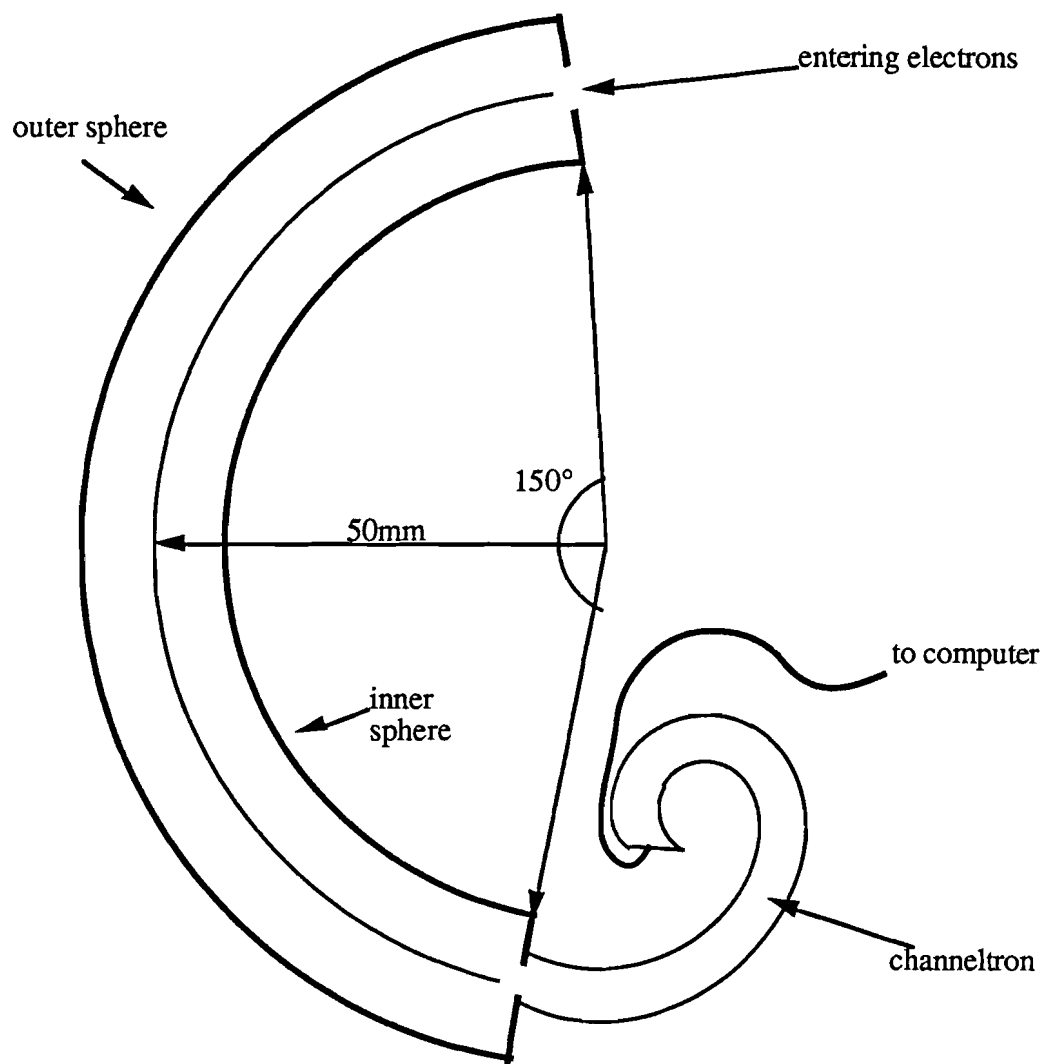


Figure 42: The hemispherical energy analyzer used in the x-ray photoelectron diffraction experiments. Electrons of a specific energy are selected to reach the channeltron by choosing appropriate values for the voltages on the outer and inner spheres. The voltage difference can be calculated from Eq. (B.1) if the detector geometry is known.

## APPENDIX C

### PREDICTION OF THE DEPENDENCE OF THE FORWARD-SCATTERING AMPLITUDE ON ATOMIC VIBRATIONS

In this Appendix, the dependence of the diffraction intensity on thermal vibrations is developed for XPD for the case of forward scattering. This calculation helps to illustrate the anomaly between the minimal dependence of forward-scattered peaks on lattice vibrations as predicted in the SSC model and the apparent significant contribution of the Debye-Waller effect to the intensity attenuation of forward-scattered peaks to the experimental data. If  $\mathbf{r}$ ,  $\mathbf{r}-\mathbf{r}_j$ , and  $\mathbf{r}_j$ , are designated as the vectors from the emitter to the detector, from the first scatterer to the detector, and from the emitter to the first scatterer, respectively, then the path length from the first scatterer to the detector is

$$|\mathbf{r}-\mathbf{r}_j| \cong |\mathbf{r}| - (\mathbf{r}_j \cdot \hat{\mathbf{r}}) \text{ when } |\mathbf{r}_j| \ll |\mathbf{r}|, |\mathbf{r}-\mathbf{r}_j|. \quad (\text{C.1})$$

The path difference between a single-scattered electron and an unscattered electron is given by

$$\Delta r = |\mathbf{r}-\mathbf{r}_j| + |\mathbf{r}_j| - |\mathbf{r}| \cong |\mathbf{r}| + |\mathbf{r}_j| - (\mathbf{r}_j \cdot \hat{\mathbf{r}}) - |\mathbf{r}| = |\mathbf{r}_j| - (\mathbf{r}_j \cdot \hat{\mathbf{r}}). \quad (\text{C.2})$$

For forward scattering without thermal vibrations  $\mathbf{r}_j \parallel \mathbf{r}$  and  $\Delta r = 0$ .  $\Delta r = r_j(1-\cos\theta_j)$  for a single-scattering event, as discussed in Section 2.4.1, since  $\mathbf{r}_j$  is not parallel to  $\mathbf{r}$  in this case.  $\theta_j$  is the angle between  $\mathbf{r}$  and  $\mathbf{r}-\mathbf{r}_j$ . If thermal vibrations are included, then  $\mathbf{r}_j \rightarrow \mathbf{r}_j^0 + \mathbf{u}$ , where  $\mathbf{u}$  is assumed to be isotropic and is small compared to  $\mathbf{r}_j^0$ .

For the case of forward scattering and  $\mathbf{r}_j^0 \parallel \mathbf{r}$ , the path difference becomes

$$\begin{aligned}
 \Delta r &= |\mathbf{r}_j^0 + \mathbf{u}| - (\mathbf{r}_j^0 \cdot \hat{\mathbf{r}}) - (\mathbf{u} \cdot \hat{\mathbf{r}}) \\
 &= \sqrt{|\mathbf{r}_j^0|^2 + |\mathbf{u}|^2 + 2\mathbf{r}_j^0 \cdot \mathbf{u}} - (\mathbf{r}_j^0 \cdot \hat{\mathbf{r}}) - (\mathbf{u} \cdot \hat{\mathbf{r}}) \\
 &\equiv |\mathbf{r}_j^0| \left[ 1 + \frac{1}{2} \left( \frac{|\mathbf{u}|^2}{|\mathbf{r}_j^0|^2} + \frac{2\mathbf{r}_j^0 \cdot \mathbf{u}}{|\mathbf{r}_j^0|^2} + \text{higher terms} \right) \right] - (\mathbf{r}_j^0 \cdot \hat{\mathbf{r}}) - (\mathbf{u} \cdot \hat{\mathbf{r}}) \\
 &\equiv |\mathbf{r}_j^0| + \frac{\mathbf{u}^2}{2|\mathbf{r}_j^0|} + \frac{\mathbf{r}_j^0 \cdot \mathbf{u}}{|\mathbf{r}_j^0|} - (\mathbf{r}_j^0 \cdot \hat{\mathbf{r}}) - (\mathbf{u} \cdot \hat{\mathbf{r}}) \quad (\text{C.3}) \\
 &= \frac{\mathbf{u}^2}{2|\mathbf{r}_j^0|}.
 \end{aligned}$$

Now, the exponent in the Debye-Waller factor goes as  $(\Delta \mathbf{k} \cdot \Delta \mathbf{r})^2$ . This shows that in the case of forward scattering thermal vibrations have no contribution to the diffraction intensity in the harmonic approximation, i.e. no term in the exponent goes as  $\mathbf{u}^2(T)$ , and therefore is linear in  $T$ . However, since the experimental data shows a very strong exponential dependence in  $T$ , the data suggest that single scattering, multiple scattering, and perhaps other effects are important in the thermal behavior of forward-scattered peaks.

## APPENDIX D

### CALCULATING THE SURFACE DEBYE TEMPERATURE USING RHEED

It is well known that a surface does not behave as a simple termination of the bulk. The asymmetric bonding and the reduced number of nearest-neighbors that characterize a surface atom as compared to an atom in the bulk of the crystal result in an increased vibrational amplitude of the surface atoms. Measurements of this enhanced vibrational amplitude of surface atoms have been carried out using LEED.<sup>1,2</sup> Although rarely used for this purpose, RHEED is a comparable technique with which to determine surface Debye temperatures. As a result of the glancing angle of incidence used in RHEED, the depth probed by the electrons into the sample is on the same order as that of the low-energy electrons are at near-normal incidence in LEED. Therefore, LEED and RHEED have comparable surface sensitivities. Below, the use of RHEED to determine effective surface Debye temperatures is demonstrated.

The sensitivity of diffraction intensity to temperature arises from the increase in the atomic vibrational amplitude with temperature. The temperature increase is observed as a decrease in the elastic diffraction intensity. The Debye-Waller effect, which describes this temperature dependence, was analyzed by Debye<sup>3</sup> in 1913 and later modified by Waller<sup>4</sup>. In this treatment, atomic vibrations are assumed to be harmonic and the influence of multiple scattering events is ignored. In general, this assumption is most valid for temperatures below the Debye temperature, however this assumption is valid at higher temperatures for the case of elastic diffraction. According to the Debye-Waller effect, the intensity attenuation of elastic diffraction is described by

$$I(T) = I(0)\exp(-MT) , \quad (D.1)$$

where  $I(T)$  is the diffraction intensity at temperature  $T$ ,  $I(0)$  is the diffraction intensity at  $T = 0$  K, and

$$-M\Gamma = -\langle (\Delta\mathbf{k} \cdot \mathbf{u}(T))^2 \rangle = -|\Delta\mathbf{k}|^2 \langle u^2(T) \rangle \quad (\text{D.2})$$

is the Debye-Waller factor. For the case of elastic diffraction, the momentum change resulting from elastic-scattering is

$$\Delta\mathbf{k} = \Delta\mathbf{k}_n = \mathbf{k}'_n - \mathbf{k}_0, \quad (\text{D.3})$$

where  $\mathbf{k}_0$  and  $\mathbf{k}'_n$  are the incident and  $n$ th-order elastically diffracted beams, respectively.  $\langle u^2(T) \rangle$  is the mean-square displacement of an atom from its equilibrium position and is assumed to be isotropic. The slope  $M$  of  $\ln[I(T)]$  versus  $T$  gives the surface Debye temperature and can be written as

$$M = \frac{|\Delta\mathbf{k}_n|^2}{|\Delta\mathbf{k}_0|^2} |\Delta\mathbf{k}_0|^2 \frac{\langle u^2(T) \rangle}{T} = \frac{|\Delta\mathbf{k}_n|^2}{|\Delta\mathbf{k}_0|^2} \left( \frac{4\pi}{\lambda} \sin\theta \right)^2 \frac{3\hbar^2}{mk_B\theta_D^2}, \quad (\text{D.4})$$

where  $\langle u^2(T) \rangle = \frac{3\hbar^2 T}{mk_B\theta_D^2}$  is valid for  $T > \theta_D$ . Specular diffraction corresponds to  $n = 0$  while  $n > 0$  corresponds to an  $n$ th-order diffraction peak. The angle of incidence  $\theta$  is defined from the plane of the surface,  $\lambda$  is the wavelength of the electrons,  $\hbar$  is Planck's constant divided by  $2\pi$ ,  $m$  is the atomic mass,  $k_B$  is Boltzmann's constant, and  $\theta_D$  is the surface Debye temperature.

A RHEED study of the temperature dependence of the elastic-diffraction intensity leads to a determination of the surface Debye temperature. The parameters  $\frac{|\Delta\mathbf{k}_n|}{|\Delta\mathbf{k}_0|}$  and  $\theta$  are obtained from a photograph of the diffraction pattern as demonstrated in

Fig. 43.  $\frac{|\Delta k_n|}{|\Delta k_0|}$  is the ratio of the distances from the transmitted beam to the center of the  $n$ th-order and specular streaks, respectively. The distances  $d$  and  $L$  from the center of the specular streak to the shadow edge, and from the sample to the image plane, respectively, allow us to calculate  $\theta$ .

Below, the use of this method is demonstrated in a measurement of the surface Debye temperature of the Pb(111) surface.<sup>5</sup> By observing the intensity attenuation of the RHEED streak maxima as a function of temperature, the dependence of  $\langle u^2(T) \rangle$  and hence  $\theta_D$  on surface orientation is obtained. The general procedures used for sample preparation, cleaning and heating are as described in the previous chapters. Quantitative analysis of the RHEED streak intensity is accomplished by imaging the output of a proximity-focused microchannel plate coupled to a phosphor screen onto a computer-interfaced linear-array detector. The detector was oriented to obtain a line scan perpendicular to a RHEED streak as shown in Fig. 30. In the experiments described below, line scans oriented perpendicular to the streak were taken at its peak intensity and at different positions along the streak by moving the diffraction pattern observed on the phosphor screen with deflection plates.

The RHEED streak intensity versus temperature for the Pb(111) surface is given in Fig. 44. The data is plotted on a semi-logarithmic scale and shows an exponential decrease of the RHEED streak intensity. For comparison, the Debye-Waller reduction in diffraction intensity assuming a bulk Debye temperature of 88 K is plotted on the same graph. The effective surface Debye temperature is obtained from Eq. (D.4), the experimentally-determined slope  $M$  of  $\ln[I(T)]$  versus  $T$ ,  $\theta$ , and  $\frac{|\Delta k_n|}{|\Delta k_0|}$ . The larger slope of the RHEED data as compared with the slope predicted assuming a bulk Debye temperature implies that the surface atoms experience an increased vibrational amplitude relative to bulk atoms. Values of  $\theta_D$  for the three low-index faces

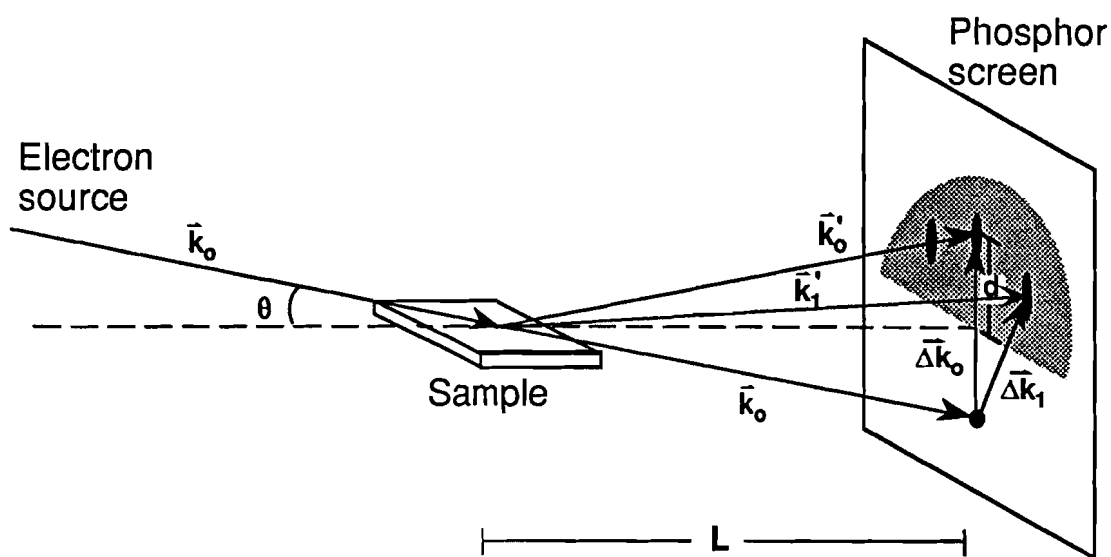


Figure 43: The parameters necessary for the calculation of the surface Debye temperature are obtained using RHEED. The incident electron beam, specular beam, and first-order diffracted electron beams are labeled  $\vec{k}_0$ ,  $\vec{k}_0'$ , and  $\vec{k}_1$ , respectively. The momentum changes corresponding to specular and first-order diffraction are given by  $\Delta k_0$  and  $\Delta k_1$ , and the ratio of their magnitudes is equivalent to the ratio of the measured distances from the transmitted beam. The angle of incidence  $\theta$  is calculated from the specular streak to shadow-edge distance  $d$  and the sample to image distance  $L$ .

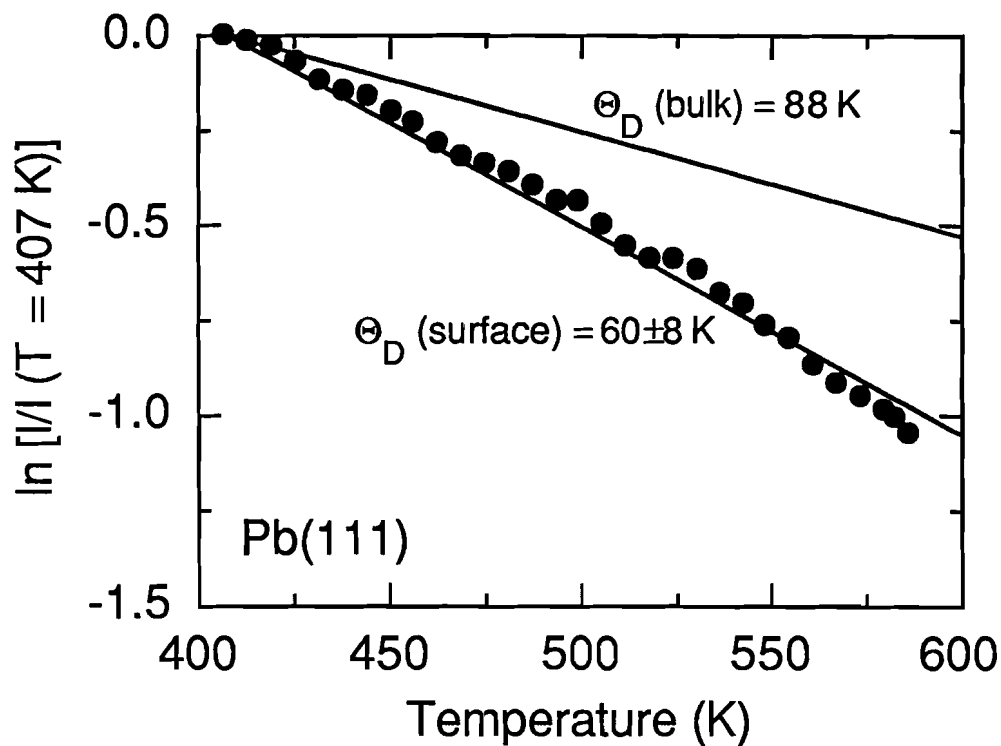


Figure 44:  $\ln[I/I(T = 407 \text{ K})]$  plotted versus temperature from Ref. 5. The slope gives the surface Debye temperature of Pb(111) obtained from the temperature-dependent RHEED intensity. The top solid line corresponds to the slope expected for a Debye temperature of 88 K, which is the Debye temperature of bulk Pb. The larger slope associated with the Pb(111) surface demonstrates the increased thermal vibrations of surface atoms relative to those of the bulk.

of Pb are given in Table 2 along with values obtained from LEED experiments for comparison.<sup>6-8</sup> The errors in the RHEED measurements are due to the spread in the slopes of the multiple semi-logarithmic plots obtained for these measurements, and the uncertainty in the measurement of the angle of incidence and momentum transfers as measured from photographs of the RHEED pattern as indicated in Fig. 43.

Table 2: The Debye Temperature for Low-Index Pb Surfaces from LEED and RHEED

technique	Pb(110) $\theta_D$	Pb(100) $\theta_D$	Pb(111) $\theta_D$	reference
LEED	37±10 K	-----	55±10 K, 49±10 K	6,7
RHEED	30±5 K	64±8 K	60±8 K	8

The RHEED measurements referenced here correspond to the temperature dependence of a first-order streak. The momentum change for a first-order streak,  $\Delta k_1$ , has components both perpendicular and parallel to the surface plane. However, the thermal behavior of both the specular and first-order streaks is monitored and it is determined that the errors associated with the measurements do not allow for an accurate separation of these components. To separate the components, a more detailed study which probes multiple crystallographic directions is necessary.

To confirm the relationship between the momentum change corresponding to different positions along a streak and temperature given in Eq. (D.4) the slope of  $\ln[I(T)]$  versus  $T$  is monitored for the positions along the RHEED streak corresponding to different values of  $|\Delta k_n|$ . This confirmation is observed graphically in Fig. 45 is a plot of  $\frac{|\Delta k_n|}{|\Delta k_0|}$  versus  $(M/\alpha)^{1/2}$  where,

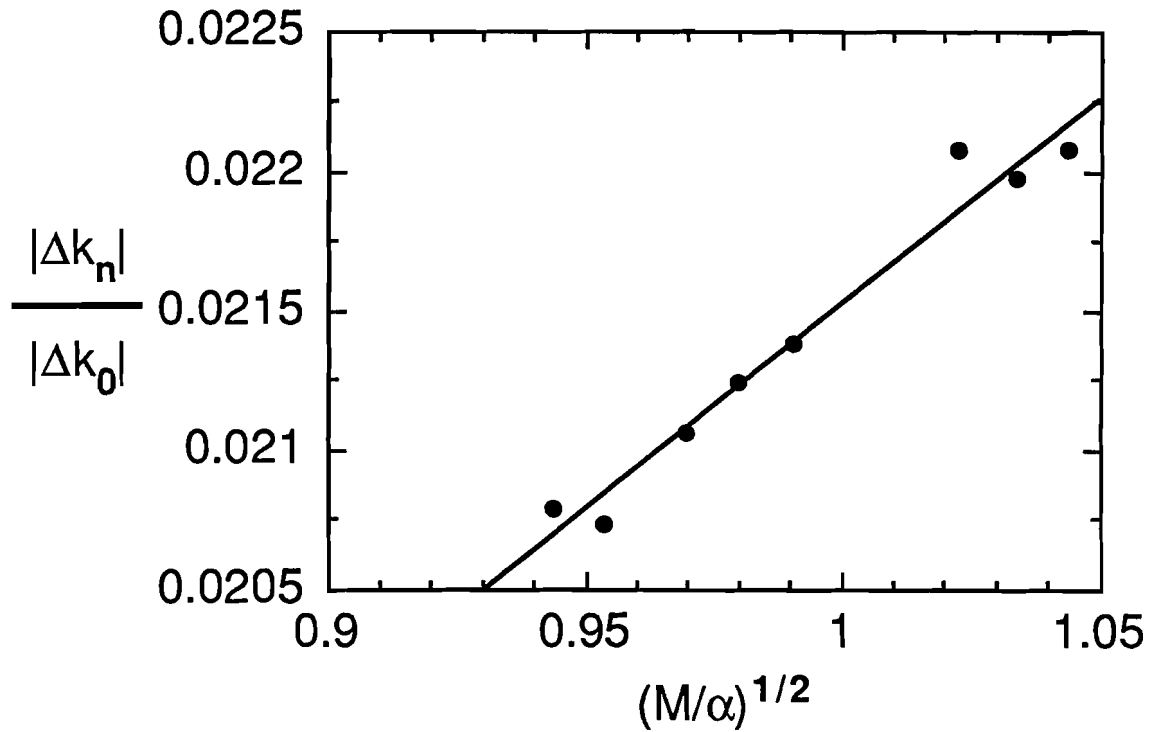


Figure 45:  $\frac{|\Delta k_n|}{|\Delta k_0|}$  plotted versus  $(M/\alpha)^{1/2}$  for Pb(111) where

$$\alpha = \frac{3\hbar^2 \left( \frac{4\pi \sin\theta}{\lambda} \right)^2}{mk_B}$$

From Eq. (D.4), the slope of this plot corresponds to a surface Debye temperature of 65 K.

$$\alpha = \frac{3\hbar^2 \left( \frac{4\pi \sin \theta}{\lambda} \right)^2}{mk_B}. \quad (\text{D.5})$$

The slope of this plot gives a surface Debye temperature of 65 K for Pb(111), which is within the error determined for Fig. 44 as well as the errors reported in Table 2.

In this Appendix it is demonstrated that RHEED is a suitable technique, comparable to LEED, with which to determine the thermal vibrations of surface atoms and hence the surface Debye temperature. In addition, RHEED has advantages over LEED in some applications. For example, RHEED, which is the principle diagnostic tool in molecular-beam epitaxy, has the ability to monitor the effect of film thickness on the thermal vibrations of surface atoms. There are advantages to using high-energy electrons, such as reduced space-charge effects, and reduced susceptibility to stray electromagnetic fields, when compared to low-energy electrons. Also, the glancing angle of incidence provides more flexibility in terms of coupling other experimental techniques with RHEED.

## REFERENCES

1. A. U. MacRae and L. H. Germer, *Phys. Rev. Lett.* **8**, 489 (1962).
2. See D. P. Jackson, *Surf. Sci.* **43**, 431 (1974) and references therein.
3. P. Debye, *Ann. Phys.* **43**, 49 (1913).
4. I. Waller, *Z. Phys.* **17**, 398 (1923); I. Waller, *Ann. Phys.* **79**, 261 (1926).
5. J. W. Herman and H. E. Elsayed-Ali, *Phys. Rev. Lett.* **69**, 1228 (1992).
6. R. M. Goodman, H. H. Farrell, and G. A. Somorjai, *J. Chem. Phys.* **48**, 1046 (1968).
7. R. M. Goodman and G. A. Somorjai, *J. Chem. Phys.* **52**, 6325 (1970).
8. J. W. Herman and H. E. Elsayed-Ali submitted to *Phys. Rev. B*.

**APPENDIX E**  
**THE HEAT-DIFFUSION MODEL**

One-dimensional heat diffusion at a solid surface is given by

$$C \frac{\partial T(z, t)}{\partial t} = K \frac{\partial^2 T(z, t)}{\partial z^2} + I_p (1 - R) \alpha e^{-\alpha z} f(t), \quad (\text{E.1})$$

where  $T(z, t)$  is the temperature profile at a distance  $z$  below the sample surface at time  $t$  and  $z$  is normal to the surface. The second term on the right-hand side gives the characteristics of the laser pulse at the surface, where the temporal dependence of the laser pulse is described by  $f(t)$ . Here,  $f(t)$  is assumed to be Gaussian.  $C$  is the heat capacity per unit volume,  $K$  is the thermal conductivity,  $R$  is the reflectivity of the surface at the laser wavelength,  $I_p$  is the peak laser intensity, and  $\alpha$  is the absorption coefficient. A uniform spatial source is assumed. The temperature rise  $\Delta T$  at the surface ( $z = 0$ ) due to laser heating is given by<sup>1</sup>

$$\Delta T(t) = \frac{I_p (1 - R) \alpha \kappa}{2K} \int_{-\infty}^t dt' \exp \left[ - \left( \frac{t'}{\tau} \right)^2 \right] \exp [\kappa \alpha (t - t')] \operatorname{erfc} \left[ 2 \sqrt{\kappa \alpha (t - t')} \right],$$

$$\text{where } \tau = \sqrt{\frac{\tau_{\text{FWHM}}^2}{4 \ln 2}} \text{ and } \kappa = \frac{K}{C}. \quad (\text{E.2})$$

$\tau_{\text{FWHM}}$  is the temporal FWHM of the laser pulse. The last term in the integrand is the complementary error function and is written as

$$\operatorname{erfc}(x) = \frac{2}{\sqrt{\pi}} \int_x^{\infty} e^{-t^2} dt. \quad (\text{E.3})$$

The heat-diffusion model dictates that the temperature rise of the laser heated surface scales directly with the laser fluence; i.e. the temporal profile of the surface temperature rise changes in magnitude and not in shape when  $I_p$  is varied. This is checked for the time-resolved RHEED experiments on Bi(0001) in Fig. 46 by confirming for a linear relationship between  $\Delta T$  and  $I_p$  for  $t_0$  and  $t_0 + 4$  ns.

Eq. (E.2) is solved for the specific physical parameters of the sample and the laser pulse in order to predict the laser-induced heating at the surface. The solution to this equation is given in Fig. 47 for pulsed-laser heating of the Bi(0001) surface. Experimental data for the Bi(0001) surface is included in the Figure. The parameters used in the model are given in Table 3. The pulse width was obtained by autocorrelation for the experiments discussed in Chapter 3. A diagram of the reflectivity setup is shown in Fig. 48, and the corresponding measurement of R versus T for  $\lambda = 1.06 \mu\text{m}$  can be found in Fig. 49. To measure the reflectivity, the oscillator beam is taken before it enters the regenerative amplifier. A chopper provides the reference frequency for the lock-in amplifiers. The beam is expanded and a portion is deflected to the reference detector to monitor intensity fluctuations. The undeflected beam is reflected off the sample surface and then captured by the signal detector. The ratio of the signal to reference is monitored versus temperature to provide a relative reflectivity measurement. To obtain an absolute measurement, the signal detector is moved so that it intercepts the beam just before it enters the UHV chamber. The signal to reference ratio before reflecting off the sample is compared to that measured after the reflection at a few temperatures. The absorption by the sapphire window on the UHV

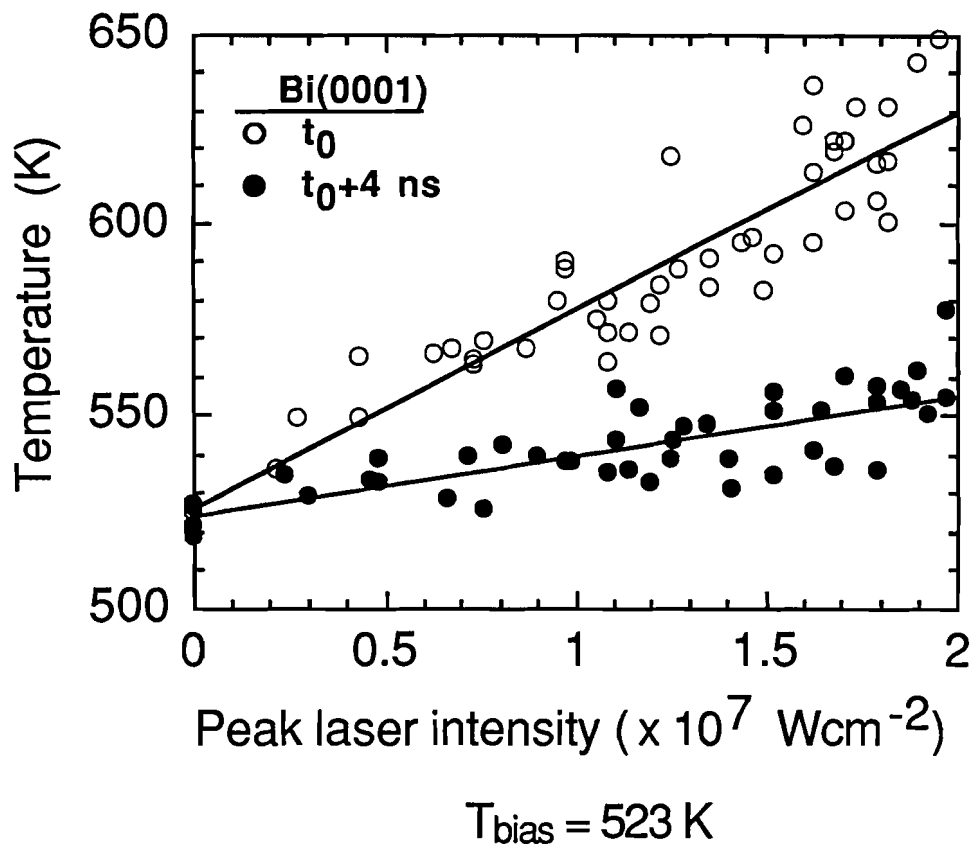


Figure 46: Temperature versus peak laser intensity plotted to confirm that  $\Delta T = T - T_{\text{bias}}$  is linear in  $I_p$ .

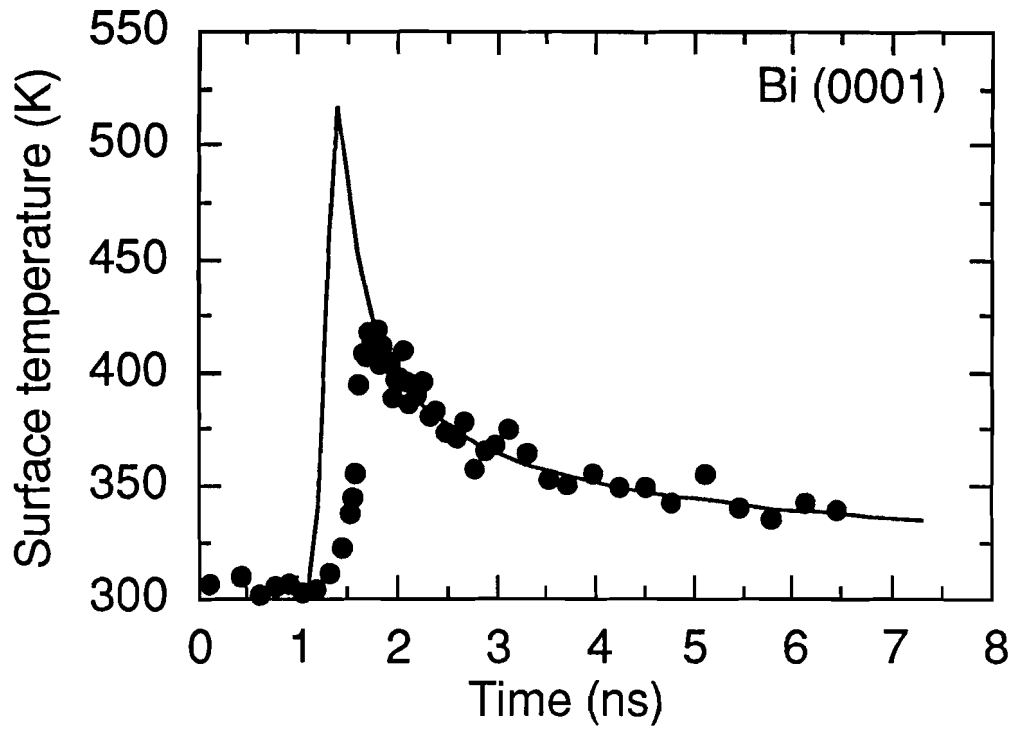


Figure 47: The heat-diffusion model calculated for laser-induced surface heating of Bi(0001). The parameters for this model can be found in Table 3.

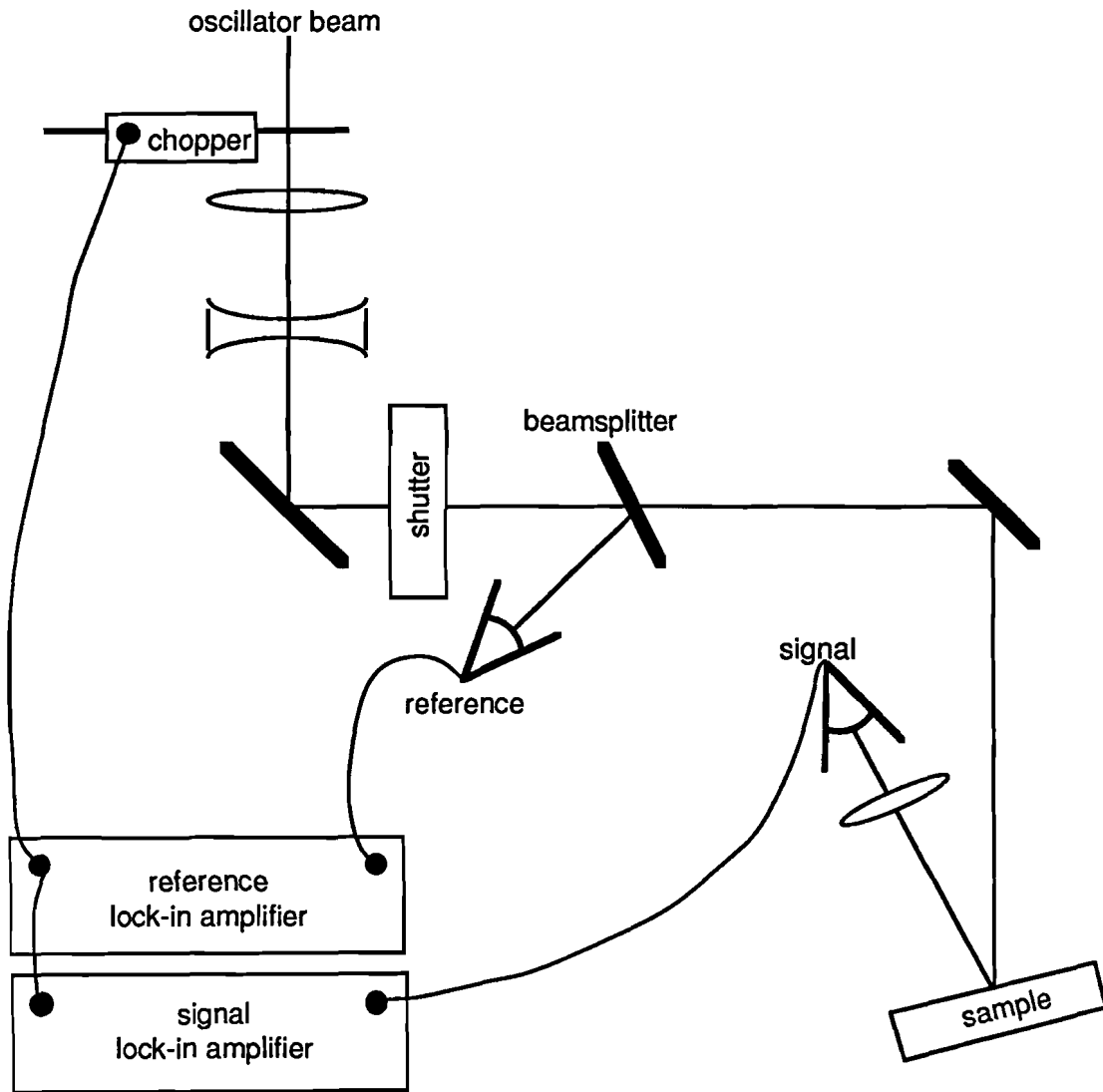


Figure 48: The experimental setup used to measure the reflectivity of the sample as a function of temperature at the laser wavelength.

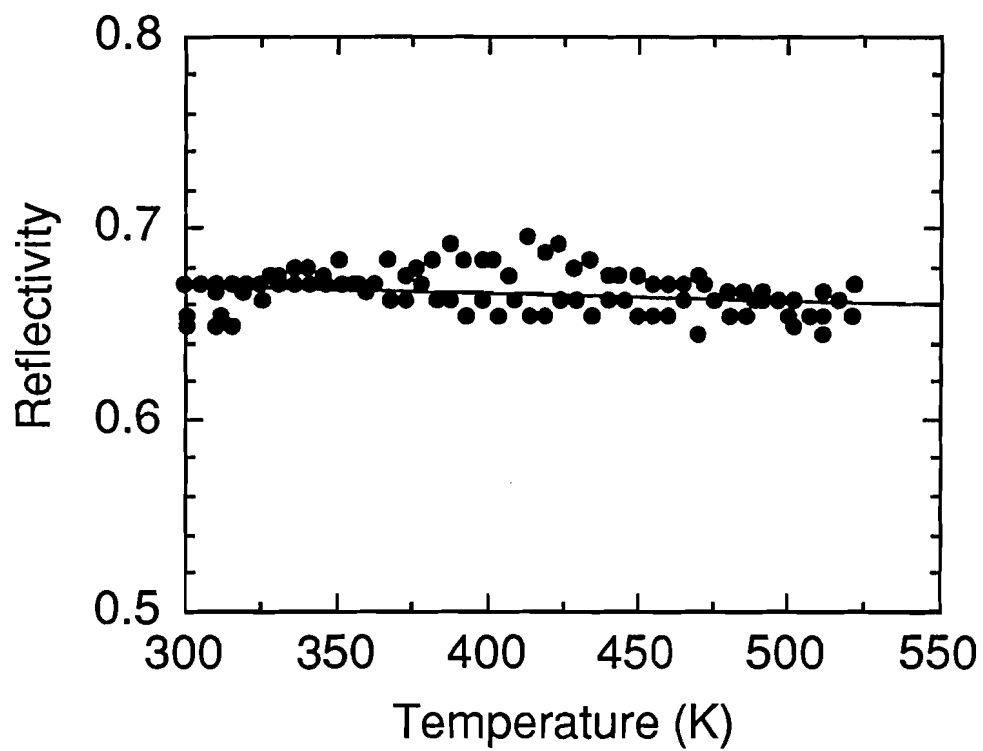


Figure 49: Experimental determination of the reflectivity of Bi(0001) for  $\lambda = 1.06 \mu\text{m}$  as a function of temperature.

chamber is accounted for in this measurement. The remaining parameters included in the model were obtained from the literature.<sup>2-4</sup>

Table 3: Heat-Diffusion-Model Parameters for Bi(0001)

$\tau_{FWHM}$ : pulse width FWHM (ps)	200
$T_{bias}$ : bias temperature (K)	300
$I_p$ : peak laser intensity ( $Wcm^{-2}$ )	$2.0 \times 10^7$
K: thermal conductivity ( $Wm^{-1}K^{-1}$ )	8.25
C: heat capacity/volume ( $Jm^{-3}K^{-1}$ )	$1.16 \times 10^6$
R: reflectivity	0.67
$\alpha$ : absorption length ( $m^{-1}$ )	$5.93 \times 10^7$

The absolute timing between the electron probe and the heating pulse is not experimentally determined. The temporal position of the experimental data relative to the heat-diffusion model in Fig. 47 is determined by minimization of the mean-squared difference between the experiment and the model for  $t_0+1 \text{ ns} < t < t_0+6 \text{ ns}$ . The one-dimensional heat-diffusion model significantly over predicts the peak surface temperature rise of the Bi(0001) surface, however, the fit in the tail is quite good. The peak surface temperature predicted by the model is expected to exceed that observed experimentally as a result of the convolution effects (first discussed in Chapter 3) which arise from the fact that the probing electron beam is not a  $\delta$ -function in time. The model does not take into account the time average which results in the experiment from the finite temporal width of the electron pulse. However, the convolution effects are probably not responsible for the entire discrepancy in peak temperature rise between experiment and model shown in Fig. 47.

The heat-diffusion model is solved for Pb for similar laser parameters as it is solved for Bi, and the corresponding temperature profiles for the two surfaces are shown in Fig. 50. The parameters for Pb(111) can be found in Table 4.<sup>3-5</sup> The laser parameters are chosen so that the same amount of laser energy is coupled to the surface, i.e.,  $I_p(1-R)$  is the same in both models. This enables the observation of the differences in the thermal parameters of the two surfaces, especially the order-of-magnitude difference in  $K$ , affects the heat diffusion. As one can see, the poorer thermal conduction in Bi results in a larger peak temperature rise, and a longer temperature decay with time. The model for Pb has been shown to provide a close fit to the data in previous experiments.<sup>6,7</sup>

Table 4: Heat-Diffusion-Model Parameters for Pb(111)

$\tau_{FWHM}$ : pulse width, FWHM (ps)	200
$T_{bias}$ : bias temperature (K)	300
$I_p$ : peak laser intensity ( $Wcm^{-2}$ )	$4.6 \times 10^7$
$K$ : thermal conductivity ( $Wm^{-1}K^{-1}$ )	34.6
$C$ : heat capacity/volume ( $Jm^{-3}K^{-1}$ )	$1.47 \times 10^6$
$R$ : reflectivity	0.857
$\alpha$ : absorption length ( $m^{-1}$ )	$6.77 \times 10^7$

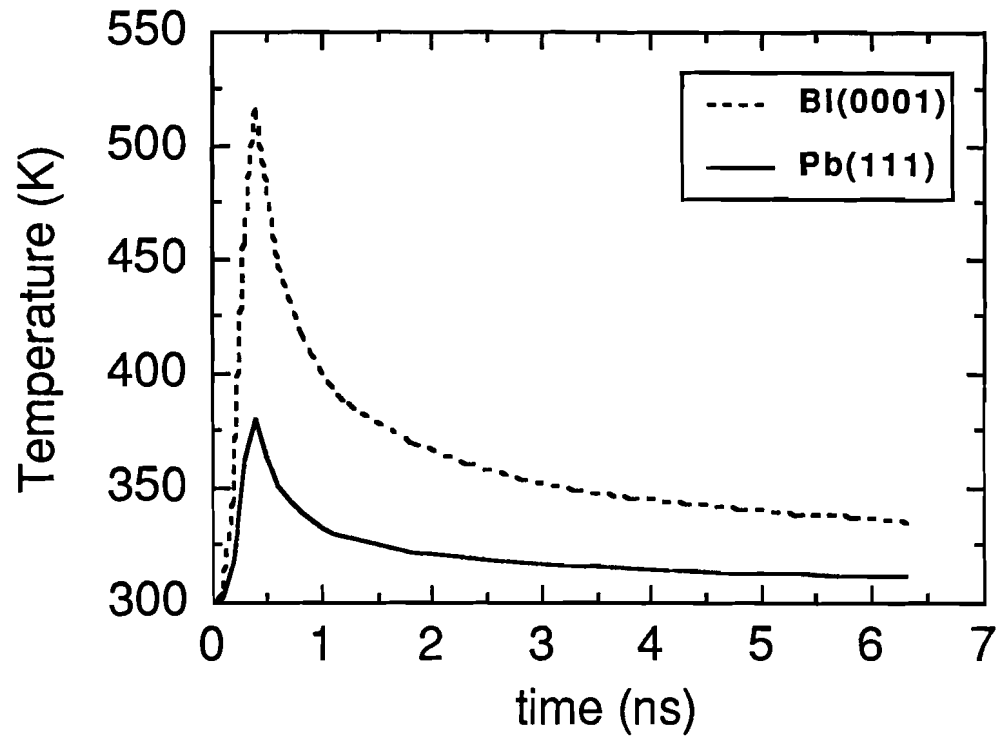


Figure 50: The heat-diffusion model solved for Bi(0001) and Pb(111) for the same laser energy absorbed at the sample surface.

**REFERENCES**

1. J. H. Bechtel, *J. Appl. Phys.* **46**, 1585 (1975).
2. J. N. Hodgson, *Proc. Phys. Soc. (London)* **B67**, 269 (1954)
3. *Thermophysical Properties of Matter*, Vols. 1 and 2, edited by Y. S. Toukourkian (Plenum Press, New York, 1970).
4. *American Institute of Physics Handbook*, 3rd ed. (McGraw-Hill, New York, 1972).
5. A. I. Golovashkin and G. P. Motulevich, *Sov. Phys. JETP* **26**, 881 (1968).
6. J. W. Herman and H. E. Elsayed-Ali, *Phys. Rev. Lett.* **69**, 1228 (1992).
7. J. W. Herman and H. E. Elsayed-Ali, *Phys. Rev. Lett.* **68**, 2952 (1992).

**INDEX**

- anisotropy** 96
  - of Bi** 54
  - of Pb** 9, 12, 42, 43, 49
- Auger electron spectroscopy** 14, 64, 65, 101
- convolution effects** 74, 88, 121
- Debye temperature**
  - bulk** 38, 81, 109, 111
  - surface** 34, 81, 97, 107
- Debye-Waller effect** 3, 8, 13, 22, 25, 49, 81, 83, 97, 105, 107
- Debye-Waller factor** 12, 29, 31, 47
- Ewald sphere** 67, 68
- heat-diffusion model** 88, 90, 115
- hemispherical energy analyzer** 14, 103
- laser fluctuations** 74
- laser-induced damage** 88, 91, 92, 93, 94, 97
- Laue condition** 64
- Lindemann criterion** 1
- mean-free path** 14, 22, 31, 46, 64
- mechanical melting point** 61
- multiple scattering** 12, 13, 16, 22, 31, 38, 39, 46, 49
- negative volume change** 54, 96
- nucleation** 7, 53, 58
- reflectivity** 91, 116
- refraction effects** 16, 30
- sample preparation** 13, 64, 109
- small-atom approximation** 30

**supercooling** 5, 7, 53

**superheating**

**Bi(0001)** 8, 9, 53

**generality of** 56, 98

**other** 7, 53, 56

**Pb(111)** 8, 9, 53, 96

**surface melting** 1

**Bi(0001)** 81

**Bi(01 $\bar{1}$ 2)** 61

**Pb(100)** 8, 11

**Pb(110)** 46, 61

**surface relaxation** 16, 33, 35, 36, 37, 49

**thermal expansion** 33, 35, 36, 37, 49

**x-ray photoelectron spectroscopy** 14, 15, 101